INVESTIGATIONS OF VOLCANIC AND EARTHQUAKE-RELATED DEFORMATION: OBSERVATIONS AND MODELS FROM LONG VALLEY CALDERA, NORTHWESTERN PELOPONNESE, AND NORTHWESTERN COSTA RICA

A Dissertation
Presented to
The Academic Faculty

by

Lujia Feng

In Partial Fulfillment
of the Requirements for the Degree
DOCTOR of PHILOSOPHY in the
School of Earth and Atmospheric Sciences

Georgia Institute of Technology
August 2011

INVESTIGATIONS OF VOLCANIC AND EARTHQUAKE-RELATED DEFORMATION: OBSERVATIONS AND MODELS FROM LONG VALLEY CALDERA, NORTHWESTERN PELOPONNESE, AND NORTHWESTERN COSTA RICA

Approved by:

Dr. Andrew V. Newman, Advisor
School of Earth and Atmospheric Sciences
Georgia Institute of Technology

Dr. Josef Dufek
School of Earth and Atmospheric Sciences
Georgia Institute of Technology

Dr. Zhigang Peng
School of Earth and Atmospheric Sciences
Georgia Institute of Technology

Dr. Timothy H. Dixon
Department of Geology
University of South Florida

Dr. Kurt L. Frankel
School of Earth and Atmospheric Sciences
Georgia Institute of Technology

Date Approved: April 25, 2011

To Mother Earth and World Peace

ACKNOWLEDGEMENTS

As the first PhD student of Dr. Andrew V. Newman, I would like to express my highest gratitude to my advisor for leading me into the broad field of geophysics, for providing excellent guidance in my growth into a qualified independent scientist, for allowing maximum freedom to pursue my scientific interests, and for supporting and encouraging me in all kinds of ways. Without Andy, I would not have the luck to discover my major interest in geodesy and tectonics, and I would not have the chance to work on them as a lift-time occupation.

I would like to thank my dissertation committee members, Dr. Zhigang Peng, Dr. Kurt L. Frankel, Dr. Josef Defuk, and Dr. Timothy H. Dixon, for taking their precious time to read my dissertation and provide invaluable comments and suggestions. Moreover, they either directly or indirectly taught me or shared with me their rich knowledge and innovative vision in their respective area of expertise. I have been greatly inspired by what I learned from them and most likely such inspiration will continuously impact on my future research.

Grant T. Farmer, now at MIT, and Yan Jiang from the University of Miami deserve credit and thanks. They offered incredible help with the GPS data processing. Special thanks go to Ting Chen for his early pioneer work on the MATLAB program, GTdef, we developed here at Georgia Tech.

Big thanks to my parents. Without their understanding and spiritual support, I could not have completed this dissertation while being so far away from home in China.

Jin Liao and Chen Li, as my roommates, gave me the most comfortable and warmest feeling of having a home in Atlanta. Thank them for everything they have done for me.

I am also grateful to my dear fellow students in our geophysics group. My PhD life would have been much more boring without their participation. After 5 years spent in EAS, it is a mission impossible to list them all, so I will only try a nonexclusive list. They are Jaime Convers, Peng Zhao, Kevin Chao, Abhijit Ghosh, Alice Koerner, Lei Liu, Kate Craft, Ming-Chu Chen, Jenn Telling, Zach Lifton, Yan Luo, Chenxiao Du, Chuanfei Dong, Ozge Karakas, Chastity Aiken, Mary Benage, Molly Lindle, Cindy Young etc. Special mention of my officemates, Chunquan Wu, Xiaofeng Meng, and Jeff Hoeft, who made our office so sweet. I will certainly miss the days and nights I spent together with all these awesome people preparing for exams, discussing problems, doing fieldswork, eating, drinking, partying, and so many other things!

This dissertation contains parts from two published manuscripts and one manuscript in prepare:

Feng, L., and A. V. Newman, Constraints on continued episodic inflation at Long Valley Caldera, based on seismic and geodetic observations, *J. Geophys. Res.*, *114*, B06403, doi:10.1029/2008JB006240, 2009.

Feng, L., A. V. Newman, G. T. Farmer, P. Psimoulis, and S. C. Stiros, Energetic rupture, coseismic and postseismic response of the 2008 M_W 6.4 Achaia-Elia Earthquake in northwestern Peloponnese, Greece: an indicator of an immature transform fault zone. *Geophys. J. Int.*, *183*(1), 103–110, doi:10.1111/j.1365-246X.2010.04747.x, 2010.

Feng, L., A. V. Newman, M. Protti, V. González, T. H. Dixon, and Y. Jiang, Interseismic megathrust coupling and forearc sliver transport near the Nicoya Peninsula, Costa Rica, between 1996 and 2010, *in prep*.

The contributions from the coauthors in ways of assisting with field campaigns, sharing data, giving advice, and revising the manuscripts are highly appreciated. Thanks Marion, Victor, Stathis, Panos, and Fanis. I had so much fun doing fieldwork in Greece and Costa Rica.

Georgia Tech Research Foundation supported the studies on Long Valley Caldera and the 2008 Earthquake in Greece. National Science Foundation grant 0847382 to A. V. Newman supported the interseismic deformation study of the Nicoya Peninsula.

A tragic bicycle accident happened to Dr. Kurt L. Frankel just before the submission of this dissertation. I was totally shocked by the unbelievable horrible news. He was a great scientist, a talented teacher, and an extremely nice person. May Kurt rest in peace. May Kurt smile in heaven. I'll always remember all the good time with him.

TABLE OF CONTENTS

LIST OF TABLES

LIST OF FIGURES

Page

SUMMARY

The advent of Global Positioning System (GPS) has revolutionized geodesy with high accuracy, fast speed, simple use, and low cost. This dissertation investigates three topics on volcano and earthquake-related deformation using GPS measurements and models to demonstrate the power of the new generation of geodetic methods. The three topics include the 2002-2003 continued episodic inflation at Long Valley Caldera in eastern California, the coseismic and postseismic response of the energetic 2008 M_W 6.4 Achaia-Elia Earthquake in northwest Peloponnese, Greece, and the interseismic megathrust coupling and forearc sliver transport near the Nicoya Peninsula in northwest Costa Rica.

CHAPTER 1

INTRODUCTION

Geodesy literally means "dividing the Earth" [*Torge*, 2001]. Ancient Greek scientists made the earliest geodetic measurements to determine the size of the Earth over 2000 years ago; in particular, Eratosthenes was the first person to estimate the circumference of the Earth assuming a spherical Earth [*Smith*, 1997]. The classical definition for geodesy by Friedrich Robert Helmert is "the science of the measurement and mapping of the Earth's surface" [*Torge*, 2001]. Helmert's definition remains fundamental today; however, modern geodesy has been continuously adding new objectives into its content. Now geodesy also includes determining the Earth's rotation and gravity field. Moreover, by observing the change of these characteristics with time, we can apply modern geodesy into many other disciplines like plate tectonics, earthquake physics, volcanology, geomorphology, seismology, oceanography, atmospheric science and so on; we can study numerous interesting earth processes and disastrous natural hazards that occur in the solid Earth, atmosphere, hydrosphere, cryosphere, and biosphere. Geodesy so far has made unprecedented success in studying volcanic and earthquake-related surface deformation, earth mass balance, sea level changes, post-glacial rebound, glacier melting, oceanic and atmospheric circulation, etc. According to the geodesy science plan – "A foundation for Innovation: Grand challenges in geodesy for the 21st century", I would expect a lot more other phenomena to be added to this category in the future.

Geodesy's transformative success largely relies on the incredible advancements of affordable high-accuracy (achieving mm accuracy after post-processing) modern geodetic measurement techniques, especially Global Positioning System (GPS) and Interferometric Synthetic Aperture Radar (InSAR).

The advent of GPS about 30 years ago has revolutionized the old-aged geodesy with high accuracy, fast speed, simple use, and low cost [*Strang and Borre*, 1997]. GPS can measure east, north, and vertical components simultaneously and continuously; therefore it combines and replaces more time- and personnel-consuming single-component methods like triangulation, leveling, and electronic distance measurement (EDM). The cost of GPS stations has been also significantly reduced making it superior to very costly methods like Very Long Baseline Interferometry (VLBI) and Satellite Laser Ranging (SLR). Strainmeters and tiltmeters have higher sensitivity than GPS, but they are limited by spatial coverage and long-term stability. InSAR is probably by far the only geodetic method that can compete with GPS, more precisely InSAR and GPS can complement each other. InSAR provides extensive spatial coverage but limited temporal coverage, while GPS provides the opposite – less spatial coverage but more temporal coverage.

This dissertation is focused on studying the volcanic and earthquake-related deformation using GPS measurements and models based on GPS observations. The research topics include volcanic deformation of Long Valley Caldera in eastern California, coseismic and postseismic deformation of the 2008 M_W 6.4 Achaia-Elia Earthquake in NW Peloponnese, Greece, and interseismic deformation of the Nicoya Peninsula in NW Costa Rica. These three cases are only examples from thousands of

successful applications of GPS; however, they are already sufficient to show how powerful GPS is for studying the deformation of the solid Earth.

CHAPTER 2

LONG VALLEY CALDERA

2.1 Introduction

Long Valley Caldera (LVC), a 15×30 km^2 oval-shaped collapse crater in eastern California (Figure 2.1), is a volcanic system that was active from ~4 Ma until the last eruptions ~0.1 Ma (see [*Bailey et al*., 1976; *Bailey*, 1989; *Hildreth*, 2004; *Hill*, 2006] for more about the volcanic history). The historic record, however, shows no observable deformation or significant earthquake activity between 1905 and the onset of the current state of unrest beginning in the late 1970s [*Hill*, 2006; *Castle et al*., 1984].

The recent unrest at LVC is characterized primarily by the uplift of the resurgent dome and recurring earthquake swarms beginning with an M_L = 5.8 earthquake on 4 Oct, 1978 [*Savage et al*., 1981; *Ryall and Ryall*, 1983; *Hill*, 2006]. Synchronous with the onset of seismicity, was the initiation of ongoing episodic uplift. Over the past 30 years, LVC has accumulated ~80 cm of the uplift centered on the resurgent dome (Figure 2.1) and produced multiple sequences of earthquake swarms in the south moat (Figure 2.1). The tools to measure the ongoing deformation have changed with time, going from initial leveling and regional triangulation [e.g. *Savage and Clark*, 1982; *Castle et al*., 1984], to local electronic distance measurements (EDM) [*Langbein*, 1989, 2003; *Langbein, et al*., 1993, 1995], campaign and continuous Global Positioning System (GPS) measurements [*Webb et al*., 1995*; Marshall et al*., 1997*; Dixon et al*., 1997*; Newman et al*., 2006], and Interferometric Synthetic Aperture Radar (InSAR) imaging [*Fialko et al*., 2001*; Newman et al*., 2006; *Tizzani et al*., 2007]. With these tools the character of uplift has been identified to consist of periods of episodic accelerated uplift, periods of steady slow

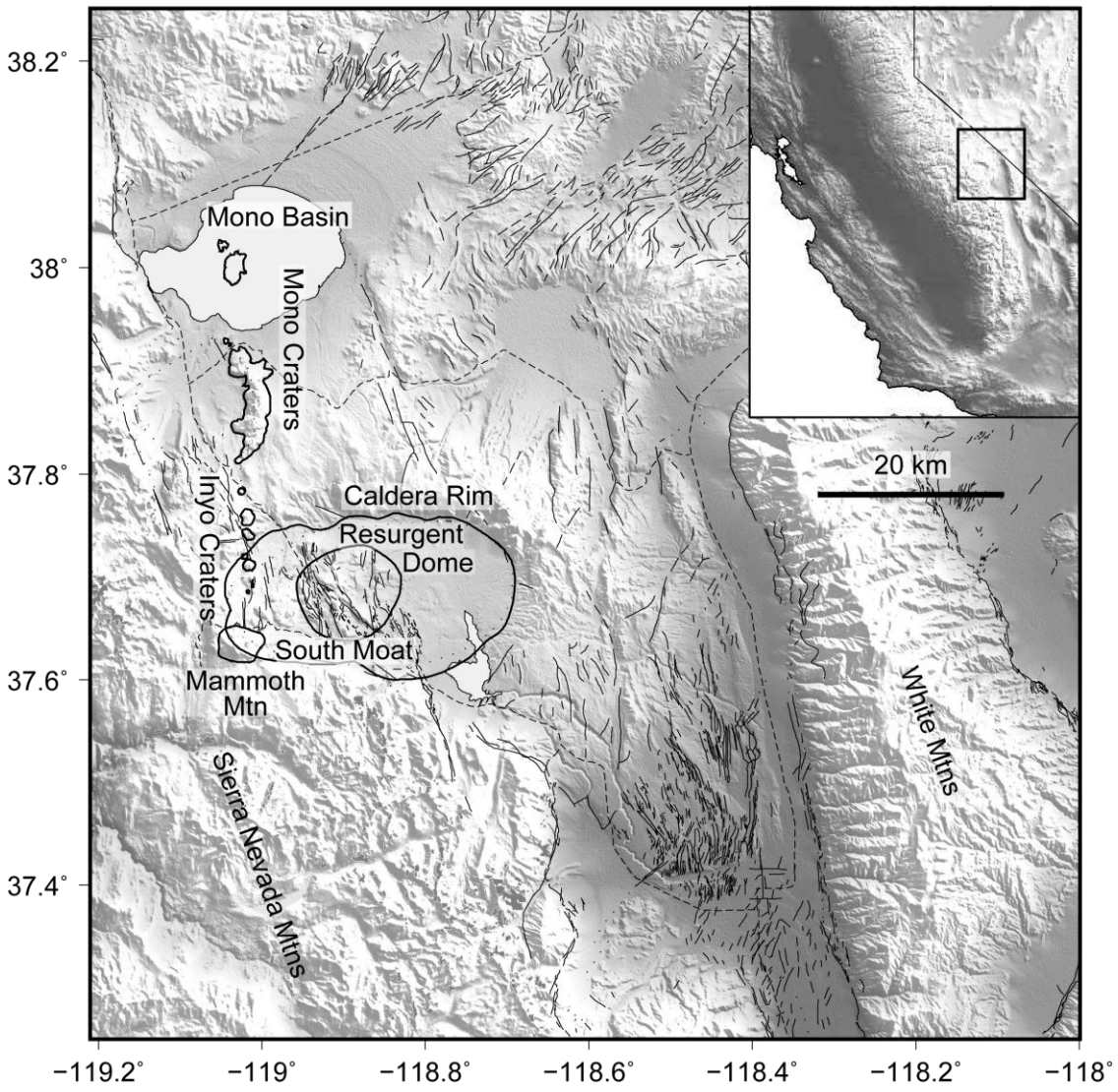

Figure 2.1: Shaded relief map of Long Valley Caldera and Mono-Inyo volcanic chain. Thick lines outline the caldera topographic rim, the resurgent dome, the Mono-Inyo craters, and Mammoth Mountain. Thin lines show the major faults in and around the Long Valley area. Dashed lines are roads. Inset shows the location of Long Valley Caldera in central eastern California.

inflation, and short-term small-amplitude deflations. The cause of LVC's recently renewed activity remains unclear; however the location of LVC along a left-step in the dextral Eastern California Shear Zone (ECSZ) likely plays an important role in maintaining pathways for magmatic activity [*Hill*, 2006]. Because both the nature of

seismicity and deformation reveal details about the ongoing subsurface processes, we briefly review the history of both through five episodes of accelerated dome growth (1979-1980, 1983, 1989-1990, 1997-1998 and 2002-2003). The most recent, and previously undocumented, 2002-2003 episode occurred with a level of GPS coverage not available in previous episodes, illuminating interactions between the resurgent dome and the Mono-Inyo volcanic chain (Figure 2.1) outside of the caldera. This episode is the focus of this paper.

Leveling, which was the major contributor to the early observation, revealed a rapid uplift of at least 25 cm at the resurgent dome in 1979-1980 [*Savage et al*., 1981; *Savage and Clark*, 1982; *Castle et al*., 1984]. During this episode, four $M_L \geq 6$ earthquakes on 25-27 May 1980 led the most intensive and vigorous earthquake sequence so far in LVC [*Ryall and Ryall*, 1983; *Denlinger and Riley*, 1984; *Hill*, 2006]. In 1980-1982, LVC continued a steady inflation with additional 10 cm uplift [*Castle et al*., 1984]. On 7 January 1983, a large earthquake swarm including two $M_L = 5.3$ events marked the second episode of uplift acceleration [*Savage and Cockerham*, 1984; *Langbein*, 2003; *Hill*, 2006]. The uplift of the resurgent dome increased to ~40 cm by August 1983 [*Castle et al*., 1984].

Two-color EDM measurements began in 1983 and repeated daily to sub-annually across the resurgent dome, and other regions in and around the caldera [*Langbein*, 1989]. EDM results documented a long-term slowing inflation with a gradual decrease in the displacement rates from 20 mm/yr in 1984 to near zero in mid-1989 across the resurgent dome, as measured between stations CASA and KRAK (Figure 2.2) [*Langbein*, 1989; *Langbein, et al*., 1993]. The corresponding seismic activity also declined to a relatively

low level through this period [*Langbein, et al*., 1993; *Hill*, 2006]. A short period of slight deflation through mid-1989 was recorded by EDM, which coincided with an 11-month-long swarm of small earthquakes under Mammoth Mountain (Figure 2.1) on the southwest rim of the caldera [*Langbein, et al*., 1993; *Hill*, 2006].

The third episode (1989-1990) started with a dramatic increase of displacement rate to 70 mm/yr in late-1989 throughout the first quarter of 1990, which was followed by a markedly increased seismicity two months later in early January 1991 [*Langbein, et al*., 1993]. The rate decreased to 30 mm/yr in April 1990 and was fairly steady at this rate through 1995, before slowing down through 1996 and dropping to less than 10 mm/yr by the end of April 1997 [*Langbein, et al*., 1993; *Langbein*, 2003; *Hill*, 2006]. Earthquake swarms still resumed in the south moat when the rate slowed down in mid-1990 and 1996 [*Langbein, et al*., 1993; *Hill*, 2006].

The fourth episode (1997-1998) began between mid-April and late-June 1997 [*Hill et al.*, 2003] as an exponential increase in the deformation rate with a ~60-day time constant [*Newman et al*., 2001]. The onset of significant microseismcity swarming initiated approximately 2 months after the onset of exponential inflation, similar to the 1989-1990 episode [*Newman et al*., 2001; *Langbein*, 2003; *Hill et al.*, 2003]. Interestingly, the peak in seismic moment release (in several M ~5 earthquakes), was coincident with the transition from exponential growth increase, to an exponential growth decay in late-November, culminating in approximately 10 cm of uplift [*Newman et al*., 2001; *Hill et al.*, 2003].

A permanent network of continuous GPS stations, most of which were established in 2000, recorded the most recent episode, which started in early 2002 and ended in early

2003, after a four-year period of slow subsidence from 1998 through the end of 2001. The accumulative uplift for this episode is ~3.5±0.8 cm estimated from the vertical displacement of site RDOM near the center of the resurgent dome, which compensated and exceeded the previous four year subsidence of ~2 cm. Interestingly, no significant increase in seismic activity was observed during this period, however, we detect an opening mode of the Mono-Inyo craters volcanic chain in this period.

The 30-years of observations show uplift and seismicity are not directly coupled neither temporally nor spatially, but do interact with each other. As an example, the 2002-2003 uplift occurred without an obvious increase in seismicity, while a vigorous 1996 earthquake swarm accompanied no uplift. When seismicity and deformation were observed to be temporally correlated, like the 1989-1990 and 1997-1998 episodes, the onset of an increased seismicity came ~2 months later than the onset of the uplift [*Newman et al.*, 2001; *Langbein*, 2003; *Hill et al.*, 2003]. In examining the occurrence of both seismic increases and periods of quiescence, we find that periods of significant anomalous seismic quiescence occur just prior to the onset of uplift in each of the 1989-1990, 1997-1998 and 2002-2003 episodes.

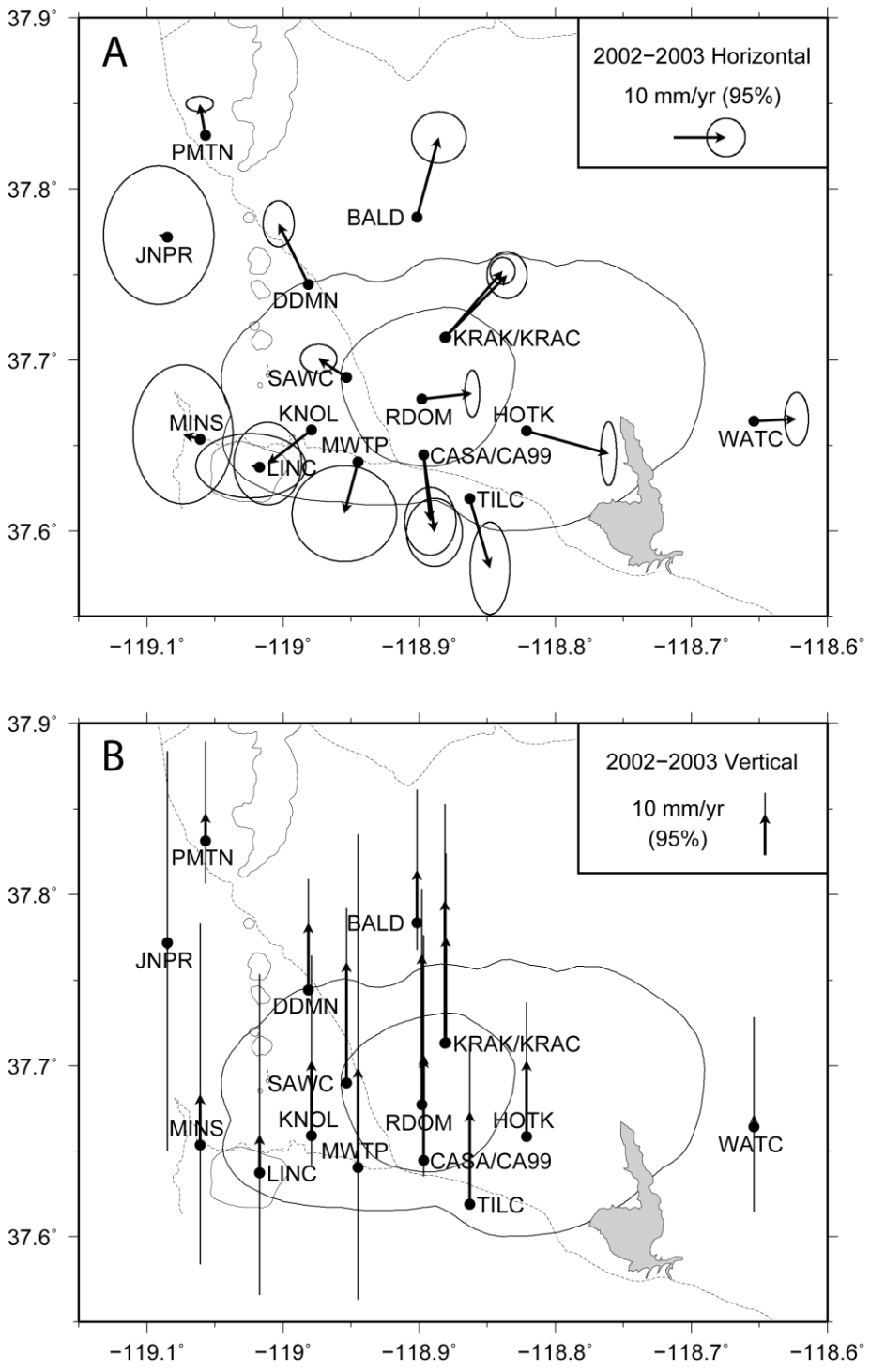

Figure 2.2: Locations of 17 continuous GPS stations in and near Long Valley Caldera. Arrows show the estimated horizontal (top) and vertical (bottom) velocities between 2002 and 2003 for all the 17 stations. Ellipses represent 95% confidence error including white noise, flicker noise and random-walk noise.

2.2 GPS Data and Analysis

A permanent continuous GPS network was established by the United States Geological Survey (USGS) in and around Long Valley beginning in 2000. The new network was established to largely replace the more personnel-intensive leveling, trilateration, and EDM surveys. Seventeen GPS stations within and near LVC operated between 2002 and 2003, providing a new and rich dataset of three-component time-dependent deformation documenting episodic deformational activity there. The locations of the GPS stations are well distributed: RDOM near the center of the resurgent dome, CASA/CA99 and KRAK/KRAC within the resurgent dome, SAWC near the boundary of the dome, KNOL, MWTP, TILC, HOTK in the moat, DDMN at the rim of the caldera, LINC in Mammoth Mountain, BALD, PMIN, JNPR, MINS and WATC outside the caldera (Figure 2.2).

The data were processed using the JPL-GIPSY software, and were obtained from the USGS at http://quake.wr.usgs.gov/research/deformation/gps/auto/LongValley/. The data are reduced to daily positions in the 2000 International Terrestrial Reference Frame (ITRF2000) relative to a stable North American plate. The precision of the data is ~3 mm in horizontal and ~8 mm in vertical. Unfiltered data are available from 1996, while filtered data with the seasonal common-mode signal over the regional network removed [*Hammond and Thatcher*, 2007; *Wdowinski et al*., 1997; *Langbein*, 2008] are available from 2000.

We use the unfiltered data, which extend back to 1996, to establish the baselines between the reference station, KRAK, and other GPS sites (Figure 2.3). KRAK is the second GPS station installed at LVC after CASA [*Dixon et al*., 1997] and is much less

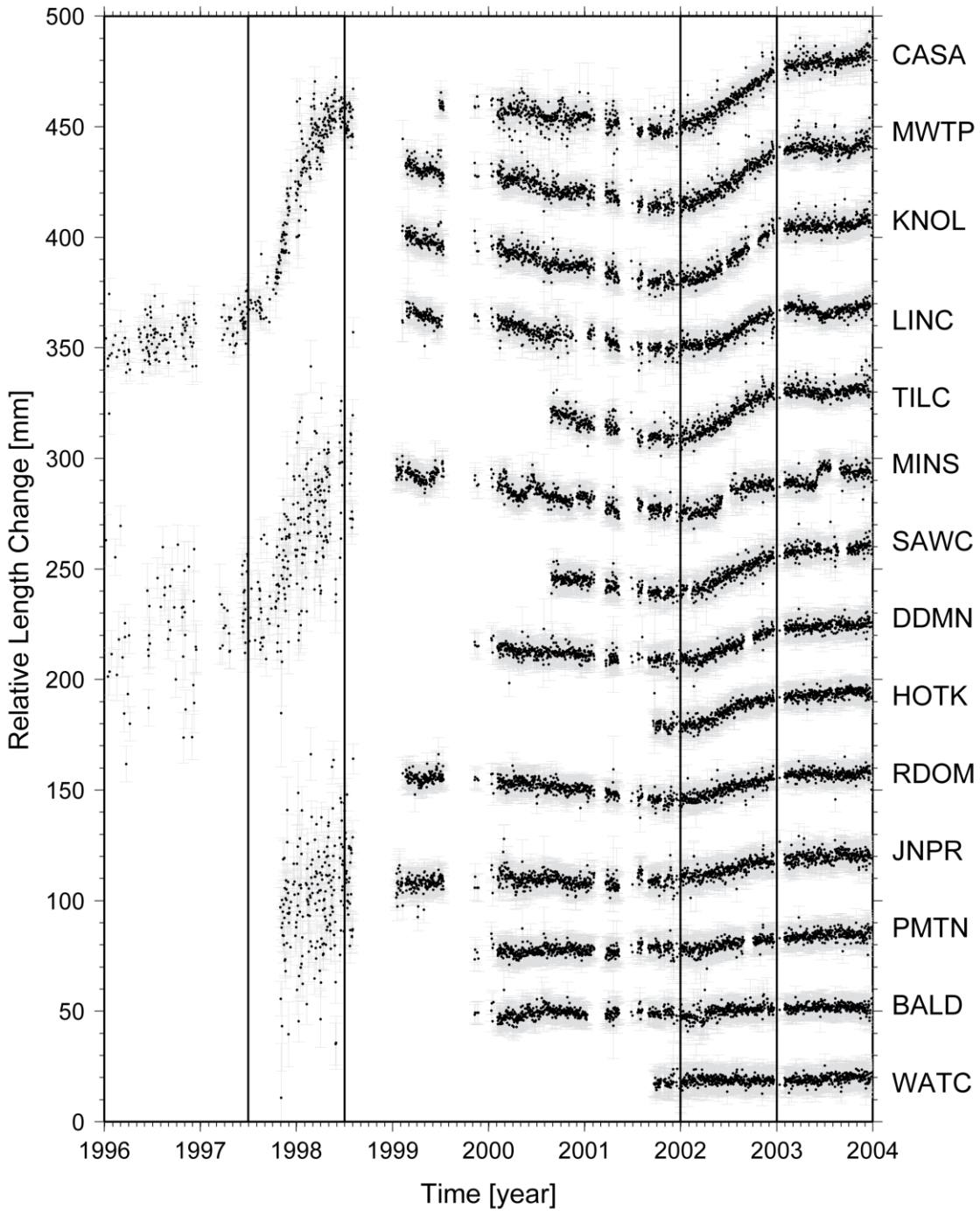

Figure 2.3: Relative GPS Baseline length changes between the reference station, KRAK, and other GPS stations. Most stations show a clear rapid extension during the 2002-2003 period right after a short-term contraction. CASA, MINS and JNPR, established before 1999, also display a much larger length increase during the 1997-1998 episode.

influenced by the geothermal power production at the Casa Diablo Hot Springs than CASA [*Langbein*, 1989; *Sorey et al*., 1995; *Howle et al*., 2003]. Because much of the noise is removed using local baselines, these results can be considered similar to the available filtered results from the USGS. The resulting baseline data show an obvious rapid change in most stations during early 2002 through early 2003. Compared to the exponential uplift in 1997-1998, the 2002-2003 uplift is quite small, about 1/3 of the size.

To get the local deformation of LVC, we further remove the effect of a rigid Sierra Nevada block relative to the stable North American plate from the regionally filtered data using the Euler vector (17.0 °N, 137.3 °W, rotation rate 0.28 degrees per million years) defined by *Dixon et al*., [2000]. Transitions associated with the onset and cessation of the most recent uplift episode are gradual and long-lasting, and hence are difficult to precisely determine from the daily GPS solutions. Thus, we chose a one-year time period between 1 Jan 2002 to 31 Dec 2002 to roughly represent the episodic uplift event. Further refinement of this episode is not likely because the end points are during a period of significant snow-cover, and hence sparse and noisy temporal data coverage. Assuming a constant uplift rate throughout the episode we estimated the approximate linear three dimensional deformation rates using a nonlinear-weighted least-squares algorithm [*Williams et al*., 2007].

The error estimate of the rate is important for the completeness of rate evaluation and understanding the level of noise. Two error sources commonly associated with GPS are time-uncorrelated white noise and time-correlated colored noise [*Mao et al*., 1999]. The time-correlated noise can be described by power-law models, such that the power density is related to frequency by f^{-n}, where f is frequency and n is the spectral index

[*Williams*, 2003; *Langbein*, 2004]. Generally, n is 1 for flicker noise [*Zhang et al.*, 1997; *Mao et al*., 1999] and 2 for random-walk noise [*Langbein and Johnson*, 1997]. A background noise model including white, flicker and random-walk noise is used to estimate the standard error in rate. The amplitude of each noise component for all 17 stations is obtained from regionally filtered data between 2000 and 2008 (see Appendix A). The uncertainties for evenly spaced data contributed from white [*Zhang et al.*, 1997], flicker [*Bos et al.*, 2008], and random-walk noise [*Zhang et al.*, 1997] are calculated respectively by

$$(\sigma_{\hat{r}})_w^2 = \frac{a_w^2}{T^2}\frac{12(n-1)}{n(n+1)} \approx \frac{12a_w^2}{nT^2} \qquad (1.1)$$

$$(\sigma_{\hat{r}})_{fl}^2 = \frac{8a_{fl}^2}{\pi \Delta T^{\frac{3}{2}}(n^2-n)} \qquad (1.2)$$

$$(\sigma_{\hat{r}})_{rw}^2 = \frac{a_{rw}^2}{T} \qquad (1.3)$$

where n is the number of data points, T is period of observation in years, ΔT is the sampling period in years. a_w, a_{fl}, and a_{rw} are the amplitudes of white, flicker, and random-walk noise, and $(\sigma_{\hat{r}})_w$, $(\sigma_{\hat{r}})_{fl}$ and $(\sigma_{\hat{r}})_{rw}$ are the standard errors in rate from white, flicker, and random-walk noise.

The total error of the rate from all the three contributors can be calculated by

$$\sigma_{\hat{r}} = \sqrt{(\sigma_{\hat{r}})_w^2 + (\sigma_{\hat{r}})_{fl}^2 + (\sigma_{\hat{r}})_{rw}^2} \qquad (1.4)$$

The estimates for the displacement rates and 95% confidence errors for the 17 regional GPS sites during 2002-2003 are shown in Figure 2.2. Most horizontal rates show a radially symmetric pattern about the western part of the resurgent dome, which is

attributed to the pressure source beneath LVC. Four stations outside the caldera (PMTN, JNPR, MINS, and LINC) largely deviated from the radial pattern. In the region west of the caldera, the influence of the relatively stronger Sierra Nevada bedrocks (as identified by an increase in seismic *P*-velocity by ~20% in Sierran crystalline bedrock to the south and west of the caldera [*Foulger et al.*, 2003] are affecting the deformational field, hence these data are removed from analysis to avoid introducing additional errors. All stations are weighted equally with the exception of the CASA/CA99 and KRAK/KRAC pairs which were each assigned half-weighting to account for collocation.

The maximum uplift of this 2002-2003 episode is approximately ~3.5±0.8 cm as determined by uplift at site RDOM, which, as its name suggests, is the closest station to the center of the resurgent dome. This uplift event compensates for subsidence after the 1997-1998 episode, resulting in approximately 80 cm of total uplift since the late 1970s.

2.3 Analytical Models

Since *Savage and Clark* [1982] performed the first model of a small spherical pressure source [*Mogi*, 1958], hereafter Mogi model, in LVC using leveling data, numerous modeling efforts have been performed on the first four uplift episodes and interim periods. Based on these results, two magmatic sources and two seismogenic sources are recognized to have contributed the surface deformation in LVC [e.g., *Hill*, 2006]. The two magmatic sources are a primary inflation source beneath the resurgent dome, and an additional deeper inflation source beneath the south moat. The two seismogenic sources are a set of WNW-striking right-lateral faults within the south moat seismic zone (SMSZ), and a set of NNE-striking left-lateral faults forming a 10-km-wide zone within the Sierra Nevada block just south of the caldera. The orientations of these

two strike-slip fault sets indicate a local ENE extension in LVC [*Hill*, 2006]. The inflation source responsible for the radial symmetric displacement pattern during the 2002-2003 episode is ~3 km west of the central resurgent dome, and is consistent with the primary inflation source from the previous episodes and interim periods. No contribution from a secondary source was resolved during the 2002-03 episode, possibly due to the reduced magnitude of overall inflation compared to previous episodes. No long-term increase in earthquake activity, or large individual earthquakes (largest M=3.2) were observed during this period, thus slip-induced deformation along the south moat is not significant during this time.

The source of previous inflation episodes has been suggested to be a combination of partially molten magma and hydrous fluids [*Hill*, 2006], and there is no evidence to suggest this episode is different. The existence of partial melt at shallow depths in the LVC is supported by the volcanic history of LVC [*Bailey et al*., 1976; *Bailey*, 1989], the seismic refraction data [*Hill*, 1976; *Hill et al*., 1985] the tomographic inversions [*Dawson et al*., 1990; *Steck*, 1995; *Sanders et al*., 1995; *Weiland et al*., 1995], and strongly suggested by changes in gravity associated with the 1997-1998 episode [*Battaglia et al.*, 1999].

A simple Mogi model is first tested to locate the inflation source by fitting the GPS data. The Mogi model is an analytic solution for a spherical pressure source, which represents a uniformly pressurized spherical cavity in a homogeneous elastic half-space, and is valid for a relatively small radius compared to its depth [*Mogi*, 1958] (Figure 2.4a). With the pressure P replaced by the volume change ΔV and the source radius a using the relation $P = \frac{\mu \Delta V}{\pi a^3}$ [*McTigue*, 1987], the number of free parameters can be

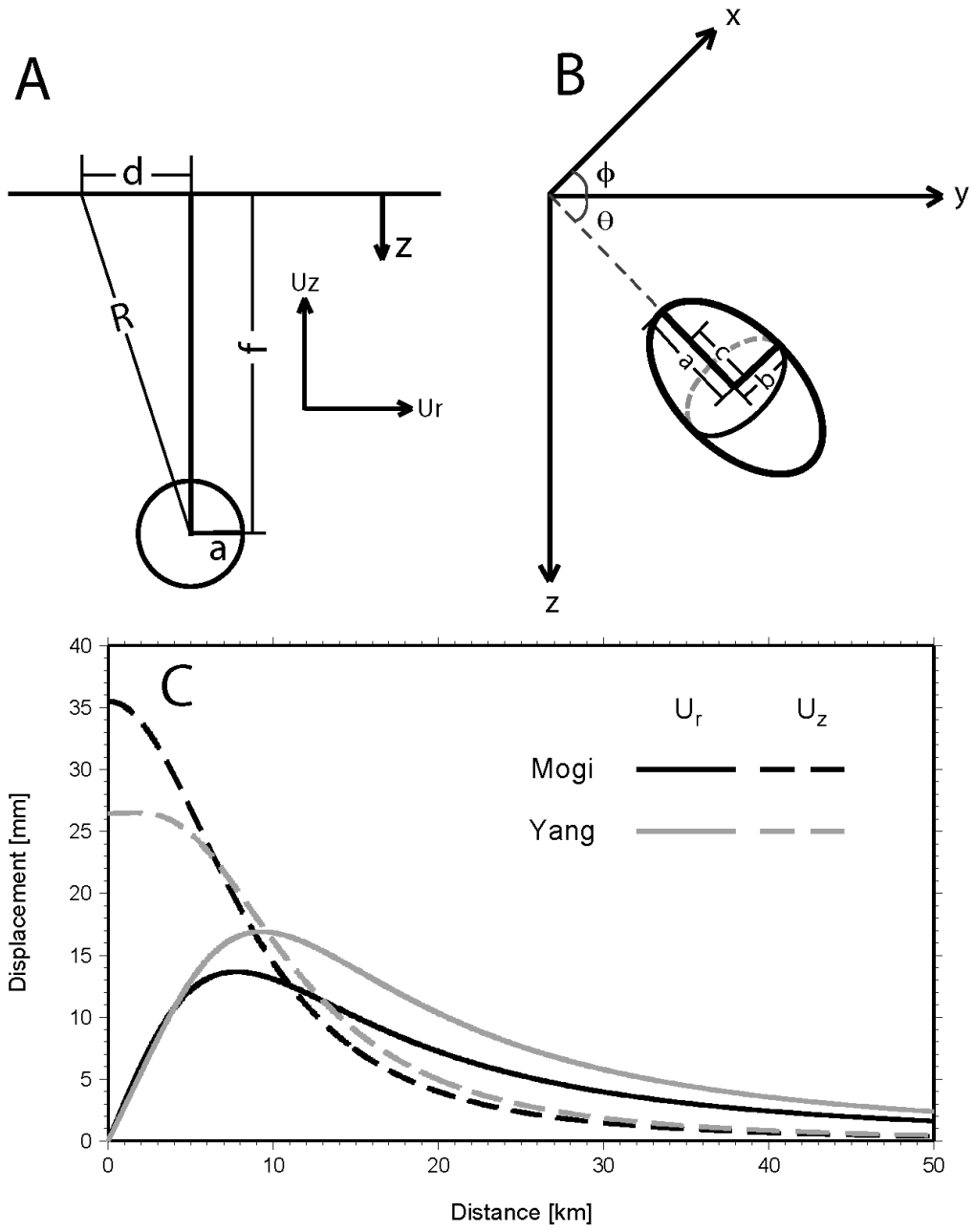

Figure 2.4: Schematic characterization and coordinate systems for the analytic Mogi and Yang models. (a) Mogi model: *a* and *f* are the radius and depth of the sphere, *d* and *R* are the horizontal and linear distance to the center of the sphere satisfying $R^2 = d^2 + f^2$. (b) Yang model: *a* and *b* are the semi-major and semi-minor axes, c is the distance from center to focus satisfying $a^2 = b^2 + c^2$, θ and ϕ are the dip and azimuth of the spheroid. (c) Vertical and radial displacements away from a Mogi source (at z = 11 km, ΔV = 0.018 km^3), and a vertically dipping Yang source (at z = 9.6 km, ΔV = 0.021 km^3, b/a = 0.5) models.

reduced to four (3 components of source location, and volume change). To more fully describe the field of potential source locations, we used a grid search across a wide range of the four parameters to find the best-fit models utilizing all three components of observed deformation. The best fitting solutions was determined from the combination of parameters that minimized the reduced Chi-square, χ_r^2 (similar to *Newman et al.*, [2006]). Because χ_r^2 accounts for complexity of the input model, by reducing the sum of the squared residual by the degrees of freedom, it is also a good indicator of the appropriateness of a given model, such that a result that approaches 1.0 theoretically has both an ideally suited model, and appropriately determined errors [*Press et al.*, 1992].

Because of its simplicity, the Mogi model is a useful tool for initially assessing the location and approximate magnitude of an inflation source. However, it is appropriate to assess other models that may more accurately characterize the nature of the source or rheology, if adequate spatially dense data are available. The vertically dipping prolate spheroid model [*Yang et al.*, 1988], hereafter Yang model, has been found to more adequately characterize the deformation sources from the previous episodes [*Fialko et al.*, 2001; *Battaglia et al.*, 2003a, 2003b; *Langbein*, 2003], therefore we additionally test its utility for the 2002-03 episode. The Yang model was developed as an arbitrarily dipping finite prolate spheroid pressure source model, which represents a uniformly pressured arbitrarily oriented prolate spheroid cavity of finite dimensions in a homogeneous elastic half-space (Figure 2.4b). With the substitution of $\frac{\mu \Delta V}{\pi a b^2}$ for P, where ΔV is the volume change, a is the semi-major axis, b is the semi-minor axis, and μ is the shear modulus [*Tiampo et al.*, 2000], the Yang model requires seven free

parameters to calculate the displacements at surface for a Poisson's solid (source location, volume change, axis ratio (b/a), and the dip and azimuth of the spheroid). Because previous models do not require a significant dip on the prolate spheroid geometry, we thus hold it fixed thereby removing two parameters (dip and azimuth). Similar to the method used for solving the Mogi model, we applied a grid search across a range of the remaining five free parameters to find the best-fit parameter combination. While the overall shape of deformation is similar between the Mogi and a vertically dipping Yang Model, subtle differences in the shape of both vertical and radial deformational fields increase as the Yang model becomes more prolate (Figure 2.4c).

Table 2.1: Summary for Models including 95% likelihood range as determined by bootstrap

Model	ndf	χ^2	χ_r^2	Longitude (°)	Latitude (°)	Depth (km)	ΔV (km^3)	b/a
No Model	33	1534.55	46.50					
Mogi	29	56.72	1.96	-118.930 -118.935– -118.908	37.678 37.672–37.687	11.7 7.5–13.5	0.023 0.010–0.030	N/A
Yang	28	52.83	1.89	-118.931 -118.936– -118.910	37.678 37.672–37.686	10.6 9.2–12.2	0.022 0.015–0.027	0.76 0.55-0.99

2.4 Model Results

The parameters of the best-fit Mogi and Yang models are summarized in Table 2.1. Both best-fit models explain up to 96% of the surface deformation. The χ_r^2 of both is about 1.9, suggesting our simple analytical models are appropriate for the observed deformation and the errors are realistic. While the χ_r^2 of the Yang solution is fractionally smaller than the Mogi solution, it is difficult to argue that it is enough to compensate for

the increased model complexity. An *F*-test is used to test whether the Yang model is significantly superior to the Mogi model [e.g. *Motulsky and Christopoulos*, 2003]. *F* is defined as

$$F = \frac{(\chi^2_{Mogi} - \chi^2_{Yang}) \big/ (ndf_{Mogi} - ndf_{Yang})}{\chi^2_{Yang} \big/ ndf_{Yang}} \qquad (1.5)$$

where χ^2 is Chi-square, also known as the weighted sum of the squared residuals (WSSR), ndf is the number of degrees of freedom.

We find an *F* ratio of 2.06 corresponding to 16% likelihood that the improved fit is from random chance; hence either model may be considered appropriate for this episode. Both models suggest a similar source location and volume change, and because Yang model axis ratios near 1 (optimal b/a = 0.76), that of a sphere, thus the source geometry can also be considered highly similar. The volume change for this one-year period, ~0.02 km^3, is comparable to ~0.03 km^3 from previous studies, however, the depth from this study is 11 km, and is somewhat deeper than ~7-8 km suggested for previous sources.

To test the sensitivity of best-fit results to the change in model parameters, we fix either the horizontal position or the depth and volume change (and axis ratio for Yang model) at the best-fit values to determine the Chi-square distribution of the remaining parameters. The best-fit locations are well constrained (Figures 2.5a and 2.6a), however a trade-off between depth, volume change, and ellipticity exists (Figures 2.5b, 2.6b and 2.6c).

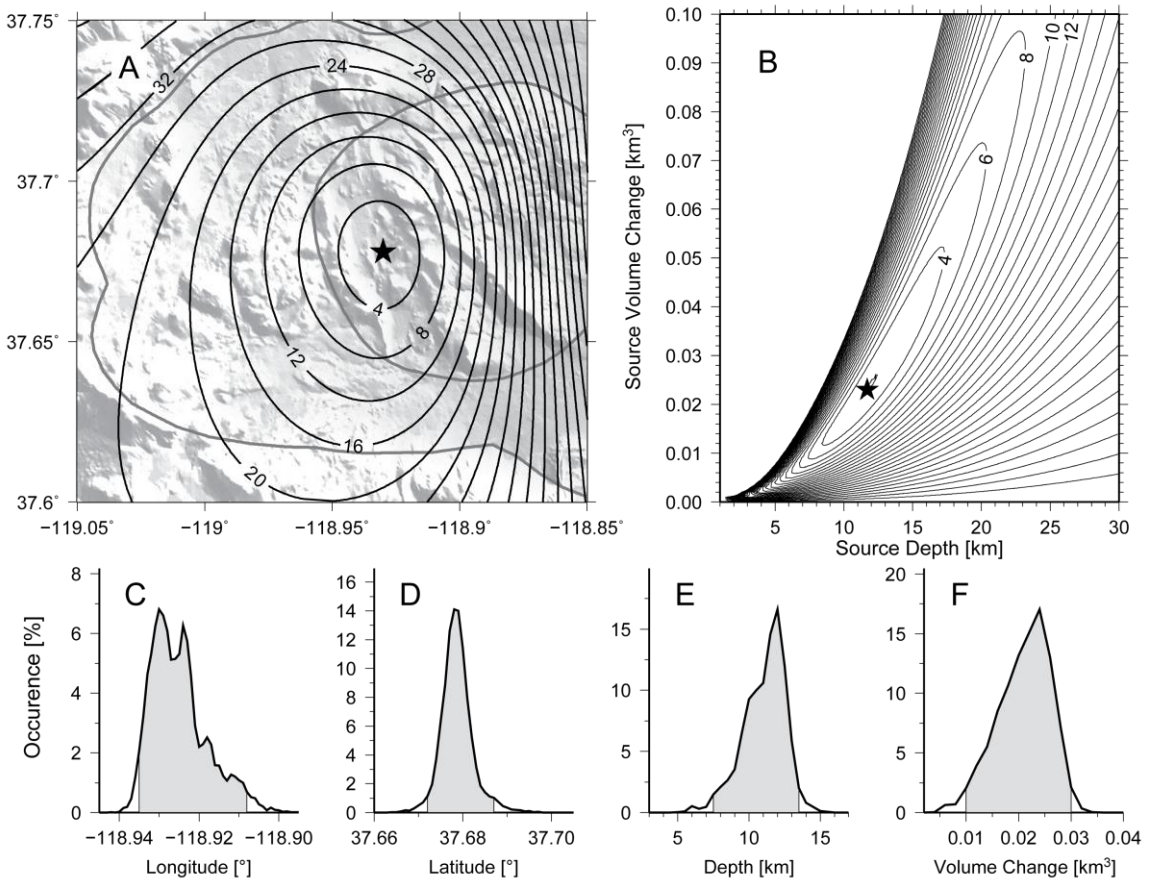

Figure 2.5: Mogi Models for the 2002-2003 episode**:** (a) and (b) are contours of χ_r^2 for the pair of longitude and latitude and the pair of source depth and volume change. Stars indicate the best-fit parameters. (c), (d), (e), and (f) are histograms of best-fit values from 10,000 bootstrap runs for the source longitude, latitude, depth and volume change. The vertical lines show the 95% confidence level.

To better assess the range of possible solutions dependent on station availability, we use a bootstrap method, randomly subsetting the data for both the Mogi and Yang models. For each of 10,000 iterations, 11 of 13 station locations were randomly selected and best-fit locations were subsequently identified. Station pairs CASA/CA99 and KRAK/KRAC were co-located, and hence were treated as 1 location each. The distribution of best-fit determinations yields a robust assessment of the probability distribution of the parameters for a given model. For the Mogi solution, we allow the four parameters (latitude, longitude, depth, and volume change) to vary simultaneously.

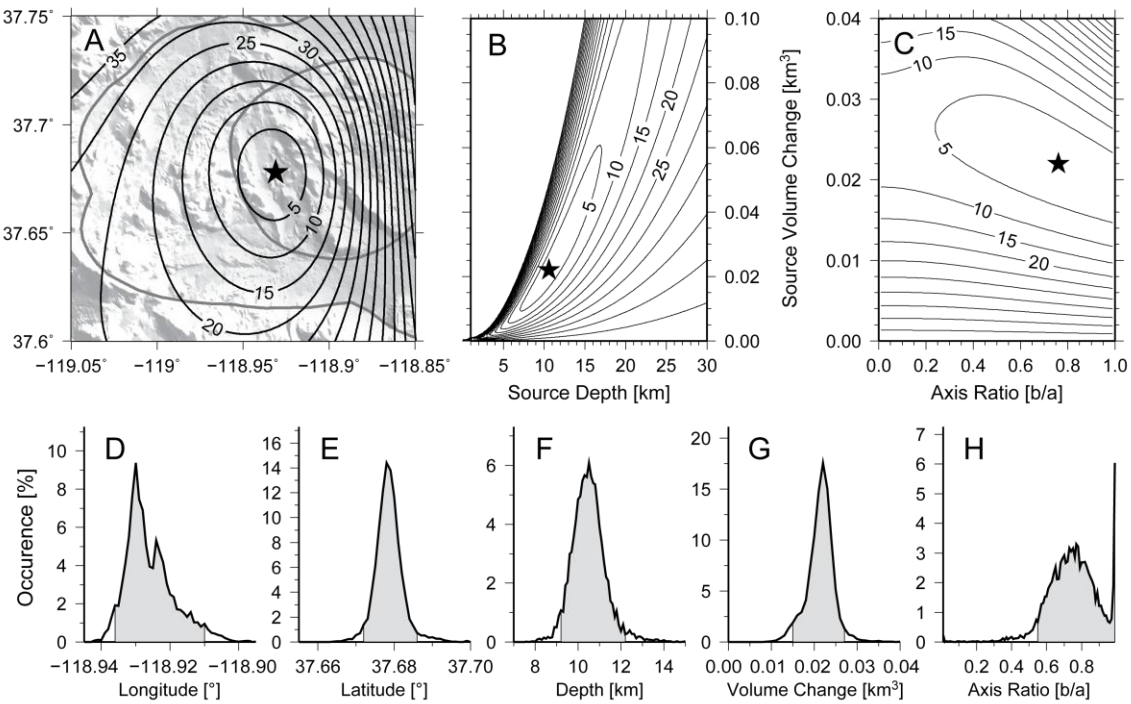

Figure 2.6: Same as Figure 2.5, but for prolate spheroid Yang models for the 2002-2003 episode. (a), (b), and (c) are contours of χ_r^2 for the pair of longitude and latitude, the pair of source depth and volume change, and the pair of axis ratio and source volume change. Stars indicate the best-fit parameters. (d), (e), (f), (g), and (h) are histograms of best-fit values from 10,000 bootstrap runs for the source longitude, latitude, depth, volume change, and axis ratio. The vertical lines show the 95% confidence level.

However, for the Yang solution we preferred to utilize a two-step process, first fixing the axis ratio (b/a) at the best-fit value to determine the simultaneous range of the horizontal position. Subsequently, we hold the horizontal position fixed at the best-fit value and determine the parameter range for depth, axis-ratio and volume change, for which there is a trade-off. The variability in each parameter is shown in Figures 2.5c-2.5f and 2.6d-2.6h. The 95% confidence is given in Table 2.1.

The model displacements are generally consistent with the GPS observations (Figures 2.7a and 2.7b), except at the four stations that were excluded from the model determinations (PMTN, JNPR, MINS, and LINC). The models overpredict deformation

at these stations presumably because the Sierra Nevada bedrock west of the caldera is stronger (tomography from *Foulger et al.,* [2003]), and hence dampens the deformation outside the caldera.

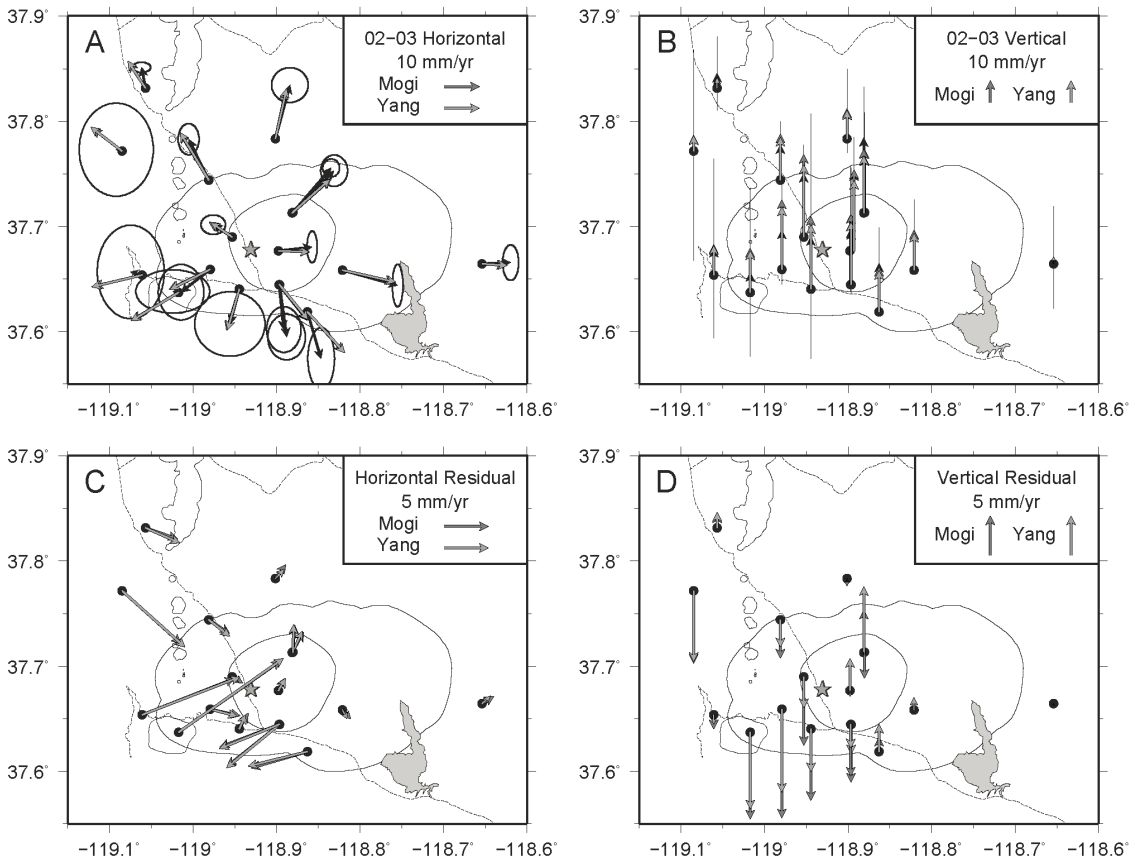

Figure 2.7: GPS and model (a) horizontal and (b) vertical velocities. Black vectors with error ellipses are observed GPS rates. Model (c) horizontal and (d) vertical residuals. Dark gray and light gray vectors are predicted from the best-fit Mogi and Yang models respectively. Dark gray and light gray stars show the best-fit location for the Mogi and Yang model.

The residual velocities (Figures 2.7c and 2.7d), which are obtained by subtracting the model prediction from the data, show some interesting features. The residuals of five station locations (BALD, KRAK/KRAC, RDOM, WATC, and MWTP) toward NE to ENE direction are consistent with the local ENE background extensional direction [Prejean et al., 2002; Hill, 2006], while the residuals of three stations (DDMN, SAWC,

and KNOL) shift 90 °towards the SE direction potentially influenced by transient activity along the Mono-Inyo chain (see next section). CASA/CA99 located 1 km east of the Casa Diablo geothermal well field has been pulled westward at a rate of 3-5 mm/yr by the local subsidence of the well field [*Sorey et al*., 1995; *Howle et al*., 2003; *Langbein*, 2003], which could explain why the residual motion of CASA/CA99 does not correspond with the observed NE-ENE extension.

2.5 Discussion

2.5.1 Opening Mode of Mono-Inyo Craters

Adjacent to LVC is both Mammoth Mountain and Mono-Inyo craters (Figure 2.1). These volcanoes form a 45-km-long north-trending volcanic chain west of, and extending north of the caldera. Petrologic results show that these two systems are compositionally distinct from LVC [e.g., *Bailey*, 1989; *Kelleher and Cameron*, 1990]. While the chain penetrates the topographic boundary of Long Valley, the system lies outside the inferred ring faults of the caldera [*Suemnicht and Varga*, 1988; *Hildreth*, 2004], and therefore they may derive from younger magma chambers not directly related to Long Valley chamber [*Bailey*, 1989; *Hildreth*, 2004; *Hill*, 2006]. However the interrelation between the two systems is still not well known.

In examining details of the eastern component of the GPS time-series for baselines of sites that cross the Mono-Inyo chain, we identify a distinct change in the opening rate associated with the 2002-2003 uplift at LVC. Four stations with high quality data are available near the Mono-Inyo chain spanning from late-1999 to either mid-2007 or present: PMTN, JNPR on the west side and BALD, DDMN on the east side (Figure 2.8a). P648-P632 (Figure 2.8a), a pair of Plate Boundary Observatory (PBO) sites

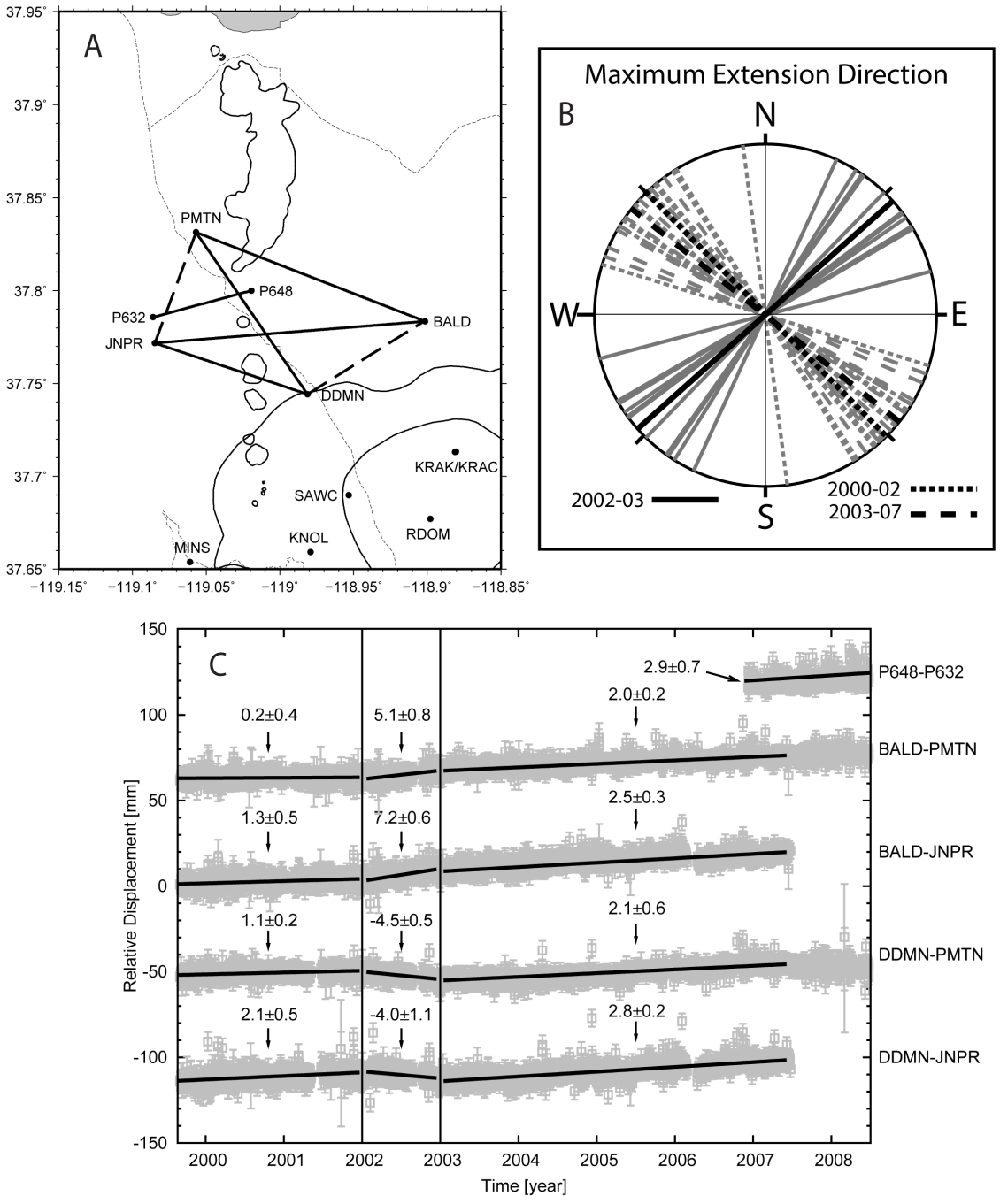

Figure 2.8: (a) GPS baselines across the Mono-Inyo craters chain. Baseline P632-P648 is used only for qualitative comparison. (b) From baselines (solid and dashed lines in a), the individual (gray) and average (black) maximum extension directions are shown for the three periods of observation. (c) East-west component of baselines crossing the volcanic chain (black lines in a). Eastward extension rates (mm/yr) with standard errors are estimated using the maximum likelihood estimator (MLE) [*Langbein*, 2004; *Langbein*, 2008]. Gray bars are GPS data with errors. Thick solid lines are best-fit. Positive rates indicate an increase in the east-west extension between sites.

available from late-2006 are also included. The east-west component of the unfiltered GPS data is used to form five east-west baselines (Figure 2.8c). Linear changes in the east-west baselines were determined using maximum likelihood estimator (MLE) [*Langbein*, 2004; *Langbein*, 2008] for three periods: the 2002-2003 inflationary episode, the pre-inflationary period including all available data after the 1997-1998 episode, and the post-inflationary period, including all available data beginning in 2003 to mid-2007 when data were available for all the baselines, and are summarized in Table 2.2 with their standard errors (1 σ).

Table 2.2: East-West extensional rates before 2002 and after 2003

Baselines	Before 2002 (mm/yr)	After 2003 (mm/yr)	Z-value	p-value
BALD-PMTN	0.24 ± 0.36	2.03 ± 0.17	4.47	0
BALD-JNPR	1.28 ± 0.49	2.54 ± 0.29	2.24	0.03
DDMN-PMTN	1.07 ± 0.21	2.15 ± 0.55	1.83	0.07
DDMN-PMTN	2.09 ± 0.46	2.79 ± 0.25	1.35	0.18
P648-P632	NA	2.91 ± 0.74	NA	NA

For both the pre-inflationary and post-inflationary periods, rates were positive showing that sites to the east are moving more eastward relative to those in the west, which can be interpreted as an opening mode of the Mono-Inyo chain. *Marshall et al.* [1997] similarly identified a possible Mono craters dike opening from a five-year campaign GPS survey in 1990-1994. During 2002-2003, all eastward baselines were dominated by the uplift. After 2003, the rates again become constant, but at rates higher than those observed before 2002. To test whether the rates before 2002 are statistically significant from those after 2003, we apply a large-sample *Z*-test for parallelism of the two lines [*Kleinbaum and Kupper*, 1978]. We first assume the slopes (rates) before 2002

and after 2003 are essentially the same as the null hypothesis and then test the probability of this assumption. Z is defined as

$$Z = \frac{\dot{u}_{eb} - \dot{u}_{ea}}{\sqrt{S^2_{\dot{u}_{eb}} + S^2_{\dot{u}_{ea}}}} \qquad (1.6)$$

where $\dot{u}_{eb}$ and $\dot{u}_{ea}$ are the slopes/rates before 2002 and after 2003, $S^2_{\dot{u}_{eb}}$ and $S^2_{\dot{u}_{ea}}$ are the variances of the estimated slopes, calculated by

$$S^2_{\dot{u}_e} = \frac{S^2_{Y \cdot X}}{(n-1)S^2_{XX}} \qquad (1.7)$$

where n is the number of data points, $S^2_{Y \cdot X}$ is the residual mean square, S^2_{XX} is the variance of the independent variable X .

Z, which corresponds to one *p*-value, should have a normal distribution with zero mean and unit variance. If $p = 0$, then there is statistically zero chance of the two data sets having the same slope. In examining early and late eastward baseline, we find that *p*-values are less than 10% for all but one baseline, where *p*-value is 18% (Table 2.2). Thus, extension rates across the Mono-Inyo chain before 2002 are statistically smaller and different than after 2003. Hence, the increased regional opening is likely real. We postulate that the change in rates is likely associated with either increases in the crustal elastic stress due to the increased inflation, or to interactive fluid pathways at depth that are common to both the resurgent dome and the Mono-Inyo chain. The same methodology was applied to north baselines: While the north DDMN-PMTN baseline rate was determined to be different at 95% confidence, the *Z*-test showed 30%, 38%, and 94% likelihood that differences were due to random variability for the pairs BALD-

PMTN, DDMN-JNPR, and BALD-JNPR. Because the Mono-Inyo chain is north trending, along with the subsurface dike [*Fink*, 1985], extension is expected to be primarily east-west, and hence we do not further consider the ambiguous north-south baselines here.

We examined the relative contribution of the recent transient inflation episode at Long Valley on the overall strain-field of the Mono-Inyo chain using the six possible baselines resolved from four stations in the region (PMTN, JNPR, BALD, and DDMN; Figure 2.8a). We separately examined the pre-inflation (2000 – 2002), co-inflation (2002 – 2003), and post-inflation (2003 – 2007). For each period we use subsets of three non-parallel baselines (avoiding sub-parallel pairs BALD-PMTN – DDMN-JNPR, and BALD-DDMN – PMTN-JNPR) to identify 12 sets of principle horizontal strain directions with their individual and average maximum extension directions, shown in Figure 2.8b (following *Turcotte and Schubert* [2002]). The maximum horizontal extension directions during the inflationary period are in good agreement with each other, and the average is trending N48E, and can be described mostly from inflationary strain from the SE. However, horizontal strains determined before and after the inflationary episode are rotated by approximately 90 °, with average maximum extension at S45E and S52E, respectively. The extension direction for these periods are in good agreement with the expected regional strain field north of the caldera due to the confluence of Sierra Nevada Block and Basin and Range extension [*Bursik and Sieh*, 1989; *Prejean et al.,* 2002]. Over the past 40,000 years *Bursik and Sieh* [1989] suggest that approximately 1mm/yr of E-W extension is accommodated along the Mono-Inyo dike system. These

modern results of between 1and 3 mm/yr observed here are comparable, but show extension to variable, both in direction and magnitude.

2.5.2 Seismic indicators of deformation change

Increased seismicity occurring approximately 2 months after the onset of inflation has been reported in both the 1989-1990 and 1997-1998 episodes [*Langbein, et al*., 1993; *Dixon et al.*, 1997; *Newman et al*., 2001; *Langbein*, 2003; *Hill et al.*, 2003]. The seismicity, which is thought to be an expression of a transition in the Eastern California Shear Zone, is predominantly along the south moat and other faults south of the caldera, and not collocated precisely with the inflationary source. However changes in crustal stress due to caldera inflation undoubtedly have an effect on seismic activity, and may act to either increase activity by increasing shear stress along faults, or decrease it by increasing fault normal stresses. A precise determination of which of these is dominant requires a careful examination of relative fault orientations to the pressure source, and characterization of the stress changes along structural and strength boundaries (e.g., along ring boundaries).

While such a characterization is beyond the scope of this paper, we empirically advance the observed relationship between the resurgent dome uplift and predominantly south moat seismicity. The earthquake data within the larger SMSZ (confined by the lower left point [-119.00 °, 37.60 °] and the upper right point [-118.8 °, 37.68 °]) from 1980 to mid-2008 are from the Northern California Seismic Network (NCSN) catalog [http://www.ncedc.org]. While long-term changes in seismicity rate may occur from network changes, likely causing an increased observation bias with time, the short-term changes of interest are largely unaffected. We use a 30-day sliding window with 1-day

step to compute the average activity. We compare these results to the CASA-KRAK EDM baseline, because it is the only continuous deformational dataset available for each episode examined (1989-1990, 1997-1998, and 2002-2003; Figure 2.9).

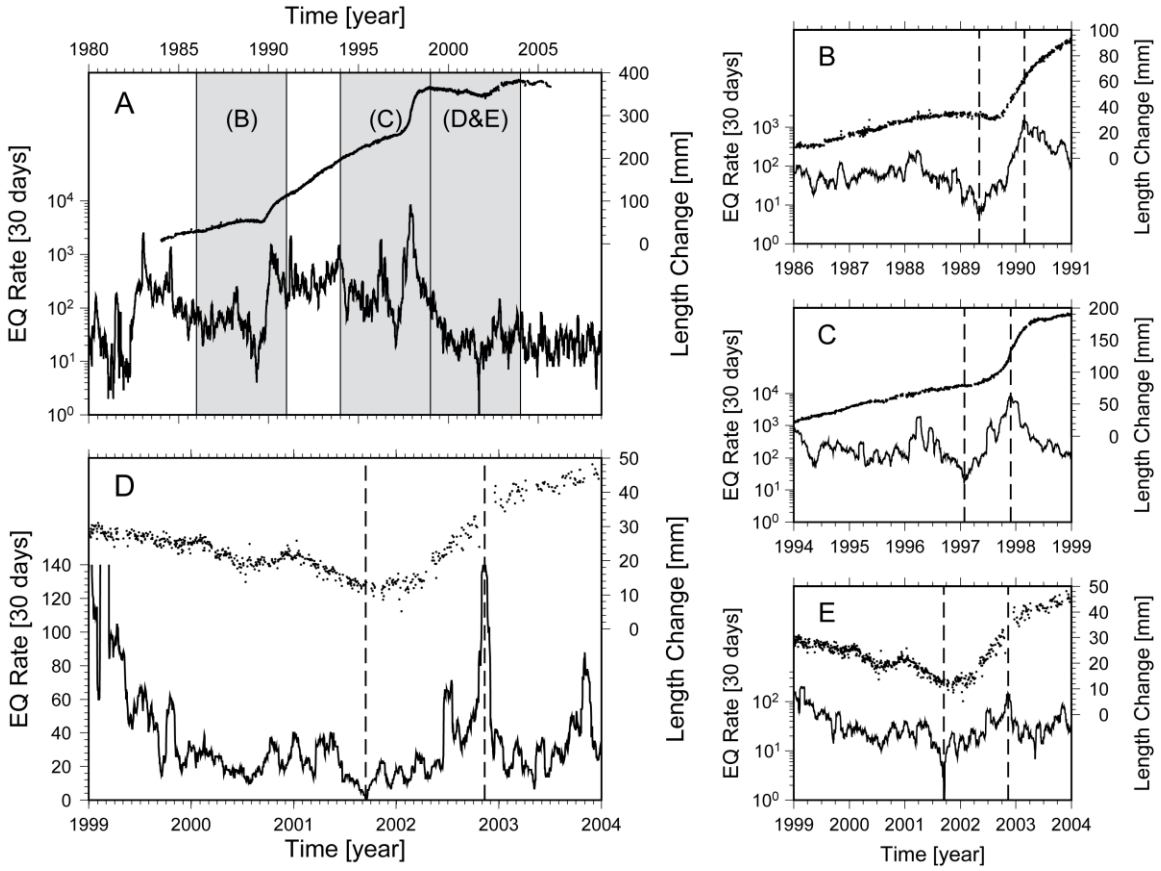

Figure 2.9: Black lines are 30-day centrally averaged earthquake rates in the larger South Moat Seismic Zone (SMSZ). Black dots are normalized EDM baselines between CASA and KRAK. (a) 1980-2006. Gray boxes highlight the periods for subplots b, c, d and e. (b) 1986-1991. (c) 1994-1999. (d & e) 1999-2004 (linear and log earthquake rates). The first dashed line in subplots b, c, d and e indicates seismic quiescence immediately prior to inflation, while the second dashed line indicates the peak in seismic activity during the maximum rate of uplift.

For all episodes, including 2002-2003 an episode with no large long-term increase in background seismicity, we observe a clear peak in seismicity during the maximum rate of uplift. The maximum periods of activity are shown against all SMSZ activity between 1984 and 2003 (Figure 2.10). Seismicity catalog used here are relocated using waveform

cross-correlation and double difference methods, yielding improved hypocenter locations [*Waldhauser and Schaff*, 2008]. While seismicity is somewhat distributed spatially over the 20 year period, activity occurs predominantly along the SMSZ during both the 1997 and 2002 peaks in activity. During these peaks, not surprisingly, the largest earthquakes also occur: A series of $M_W \sim 4.8$ events occurred in late November 1997, and an $M_d = 3.2$ occurred in early November 2003, all along the south moat.

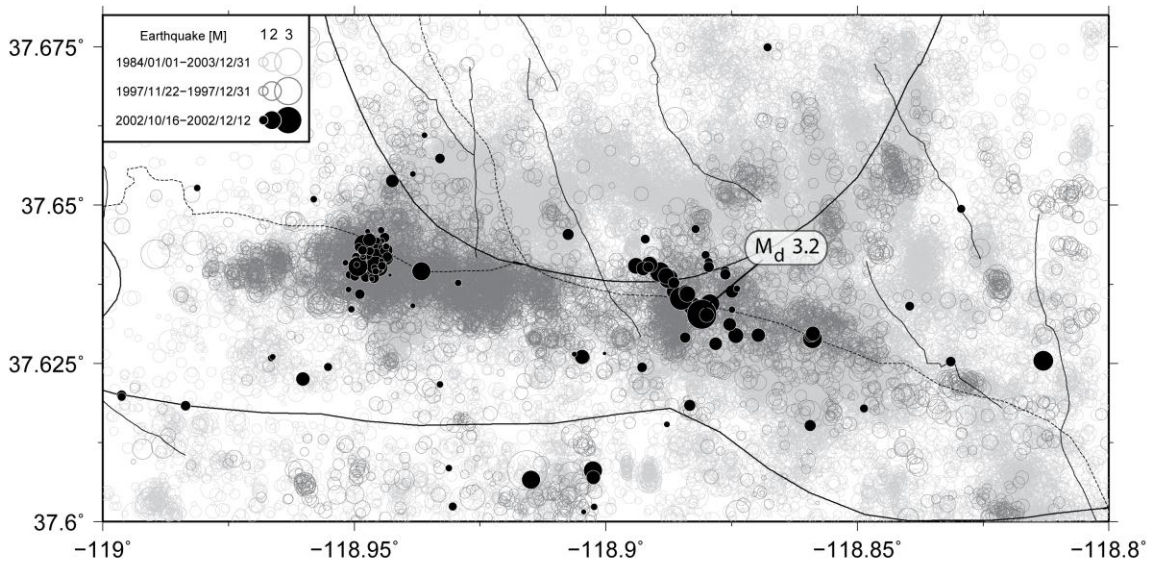

Figure 2.10: Seismicity in the larger SMSZ area between 1984 and 2003. Dark gray open circles represent earthquakes during the seismic peak of the 1997-1998 episode. Black solid circles indicate earthquakes during the seismic peak of the 2002-2003 episode. Light gray circles are other earthquakes in 1984-2003.

More surprisingly, we identified a uniquely anomalous seismic quiescence immediately prior to the onset of uplift during each episode. For each episode the seismic activity was at its absolute lowest in several years, immediately before an episode of uplift is observed. The decrease in seismicity for each quiescent period is actually lower than at any other time since the onset of the previous uplift event. For the 2002-2003 episode, only one earthquake was recorded in SMSZ for a 30-day period, while for

the preceding several years, between 20 and several hundred events were recorded monthly.

2.6 Conclusion

The most recent 2002-2003 uplift is part of the remarkable continued episodic dome growth at Long Valley Caldera that began in the late 1970s. This most recent period is similar to previous episodes of 1979-1980, 1983, 1989-1990, and 1997-1998. A total uplift of ~80 cm has accumulated on the resurgent dome. The 2002-2003 episode is responsible for ~3.5 ±0.8 cm of uplift, which is about 1/3 the magnitude of the 1997-1998 episode, but with a similar exponential shape. Whether the continued uplift over the past 25 years is a long-term transient (e.g. tumescence), or permanent dome-growth due to magmatic intrusion remains unclear.

Similar to previously observed episodes of inflation, uplift between 2002 and 2003 is primarily radial, and can largely be explained by a compact inflation source located ~3 km west of the central resurgent dome. Spherical Mogi models and vertically dipping prolate spheroid Yang models are chosen to constrain the source location and geometry. For the Mogi source, the optimal source is located at -118.930 °, 37.678 °, and approximately 11 km depth. A trade-off between depth, volume change is observed, thus a depth range between 7.5-13.5 km and a volume change of 0.01-0.03 km^3 is observed at 95% confidence. The location and volume change for the Yang model are indistinguishable from Mogi model, however a modest stretching of the source is preferred over the Spherical Mogi geometry (b/a=0.76). Both Mogi and Yang models explain up to 96% of the deformation characterized by the three orthogonal components

of 13 continuous GPS stations. A small reduction of WSSR suggests a slight but potentially insignificant preference for the prolate spheroid Yang model.

A significant increase of 1-2 mm/yr in the rate of opening of the Mono-Inyo volcanic chain is associated with the 2002-2003 uplift of LVC, as identified by changes in east-west baselines across the chain. This result suggests that the inflation within the resurgent dome of Long Valley Caldera, and activity along the Mono-Inyo craters are linked either by transmitted elastic stresses in the crust or by connectivity of deeper fluid pressures in the magmatic plumbing system.

Changes in the crustal stress regime immediately prior to and during the maximum rate of uplift may additionally be responsible for significant and consistent changes in the rate of seismic activity along the South Moat Seismic Zone. This is suggested by the observation that peak seismicity rates coincides with maximum inflation rates -- well after uplift begins. Similarly, a significant episode of seismic quiescence is identified immediately prior to the onset of the uplift in each of the 1989-1990, 1997-1998, and 2002-2003 episodes.

CHAPTER 3

NORTHWESTERN PELOPONNESE

3.1 Introduction

On 8 June 2008, a strong rupturing crustal earthquake struck NW Peloponnese, Greece (Figure 3.1b). The event is reported as a moment magnitude $M_W = 6.4$ strike-slip earthquake by the global centroid moment tensor (gCMT) catalog [Eskröm *et al.*, 2005], making it the largest such event instrumentally recorded in this area. The enhanced shaking of this earthquake was felt throughout mainland Greece. It triggered a number of landslides and rockfalls, toppled old buildings and un-/poorly reinforced houses, and cracked reinforced concrete building in nearby communities. Secondary ground fissures were observed on the pavement of roads and bridges; however, neither positive evidence of surface rupture nor significant surface deformation was observed [*Briole et al.*, 2008; *Ganas et al.*, 2009; *Margaris et al.*, 2010; this study].

The Peloponnese is part of the Aegean microplate, which is fast moving to the SW away from Eurasia at ~30 mm/yr [*McClusky et al.*, 2000; *Reilinger et al.*, 2006], overriding the African plate along the Hellenic subduction zone to the south at ~5 mm/yr [*McClusky et al.*, 2000; *Fernandes et al.*, 2003], and sliding past the Apulian platform along the dextral strike-slip Cephalonia Transform Fault (CTF) to the west [e.g. *van Hinsbergen et al.*, 2006] (Figure 3.1a). GPS sites east of the CTF show increased relative motion southward from ~10 mm/yr to ~30 mm/yr [*Hollenstein et al.*, 2006, 2008]. Aegean-Eurasian motion is partially localized on WNW-ESE trending normal faults within the fast-spreading young rift forming the Gulf of Corinth (GC) (Figure 3.1a). N-S extension within the rift increases from 11 mm/yr in the central zone to 16 mm/yr in the

west [*Avallone et al.*, 2004]. To first order, the Peloponnese is considered to move along with the Aegean plate with little internal deformation [<2 mm/yr ; *McClusky et al.*, 2000]; however, motion in the NW Peloponnese is modestly reduced and perturbed toward the south [*Hollenstein et al.*, 2008 and Figure 6 therein]. *Le Pichon et al.* [1995] proposed that the NW Peloponnese belongs to the central Ionian Islands block rather than the Peloponnese system. Due to lack of sufficient modern geodetic observations and low-rate seismicity, the extent and accommodation of strain across the region remained unclear before the 2008 Achaia-Elia Earthquake.

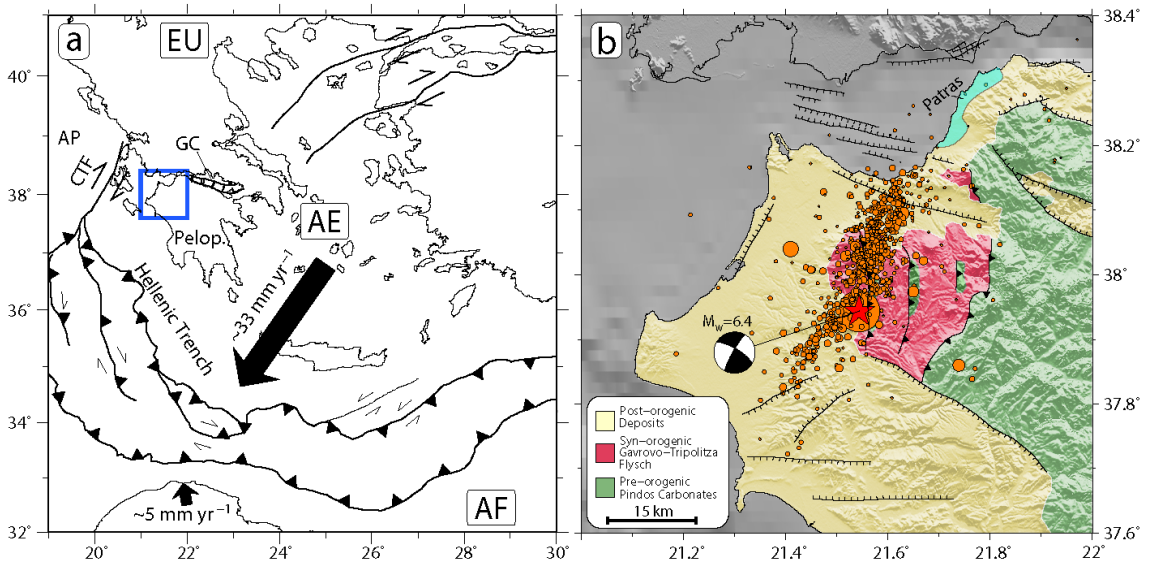

Figure 3.1: (a) Regional tectonic map of the Aegean. The major boundaries are simplified after *Kreemer and Chamot-Rooke* [2004]. Arrows show the relative motion of the Aegean (AE) [*Reilinger et al.*, 2006; *Ganas and Parsons*, 2009] and African (AF) [*Fernandes et al.*, 2003; *Ganas and Parsons*, 2009] plates to Eurasia (EU). Pelop.: Peloponnese; GC: Gulf of Corinth; AP: Apulian Platform; CTF: Cephalonia Transform Fault. Solid blue box outlines the region of Fig. 1b. (b) Simplified geological map of NW Peloponnese. Normal faults are combined from *Doutsos and Kokkalas* [2001] and *Flott e et al.* [2005]. Thrust faults are adapted from *van Hinsbergen et al.* [2006]. Orange circles indicate the 8 June 2008 mainshock and 10-day aftershocks taken from the preliminary seismic catalog of Aristotle University of Thessaloniki (AUTh catalog) (*http://geophysics.geo.auth.gr/index_en.html*). Red star is the mainshock epicenter representing rupture initiation. The gCMT focal mechanism for the mainshock is consistent with other reporting institutions. The earthquake does not associate with any existing mapped fault. The populated Patras metropolitan area is highlighted in turquoise.

The 2008 Achaia-Elia Earthquake exhibits an approximately 25 km long NE-SW trending aftershock distribution that, together with fault plane solutions (compiled in *Ganas et al.* [2009]), clearly indicates right-lateral strike-slip on a near-vertically dipping fault that is unassociated with existing mapped faults (Figure 3.1b). The earliest identified fault system in the NW Peloponnese is the N-S to NNW-SSE striking thrusts with secondary sinistral WNW-ESE and dextral WSW-ENE strike-slip faults [*Kamberis et al.*, 2000] active from the late Eocene to the Oligocene [*Sotiropoulos et al.*, 2003; *van Hinsbergen et al.*, 2005] as a part of the west-verging External Hellenide orogenic belt. The active thrust front has moved westward to the West Hellenic Arc as shown by the destructive surface-wave magnitude M_s = 7.2 Cephalonia earthquake in 1953 [*Stiros et al.*, 1994]. After the collisional episode, two independent and locally interacting sets of WNW-ESE and NE-SW trending normal faults related to the latest extensional stage dominated the area since the late Pliocene [*Doutsos and Kokkalas*, 2001]. The 2008 earthquake does not correspond to, but instead crosscuts the preexisting thrusts and normal faults. We show the NE-SW trending strike-slip faulting of the 8 June 2008 earthquake is likely part of an early stage of a diffuse transform regime, accommodating dextral motion between the Apulian and Aegean plates along with the CTF (Figure 3.1a). Because Patras, the third largest city in Greece, is located only ~35 km from the epicenter and is in the approximate striking plane of the 2008 earthquake, the continued activity along this transform system poses a previously poorly understood seismic hazard.

3.2 Strong Rupture

Using the methodology and algorithms of *Newman and Okal* [1998] and *Newman and Convers* (in review), we evaluate the radiated seismic energy from teleseismically

distributed (between 25 ° and 80 ° from the event) broad-band vertical waveforms. Averaging the seismic energy as determined from 53 stations after correcting for distance, attenuation, focal mechanism, and depth, we find that the 2008 Achaia-Elia Earthquake had excessive rupture energy that may have contributed to the enhanced shaking that caused regional damage. We obtain broad-band (period 0.5 s to 70 s) energy E_{bb} = 4x10^{14} J and high-frequency (period 0.5 s to 2 s) energy E_{hf} = 2.7x10^{14} J that correspond to broad-band and high-frequency energy magnitudes $M_{e\text{-}bb}$ = 6.8 and $M_{e\text{-}hf}$ = 7.2, respectively, using the conversion from *Choy and Boatwright* [1995]:

$$M_{e\text{-}bb} = 2/3 \, \mathrm{Log}_{10} (E_{bb}) - 2.9 \qquad (2.1)$$

after making a standard conversion from E_{hf} to E_{bb} using the relationship $E_{bb} = 5E_{hf}$ from *Newman and Convers* (in review). Our determinations are similar to the reported energy magnitude M_e = 7.0 from the US Geological Survey Preliminary Determinations of Epicenters (catalog described in *Dewey et al.* [2007]). The 0.4 and 0.8 unit magnitude discrepancies between the energy and moment magnitudes highlight the disproportional increase in high-frequency shaking of the event, which may be the result of relatively high stress drop $\Delta\sigma$.

Such a determination can be made by the direct comparison between energy E_{bb} and moment release M_0 of an event, where

$$\Delta\sigma = 2 \, GE_{bb}/M_0 \qquad (2.2)$$

allowing few assumptions about the extent of coseismic and final stress along the rupture, and regional crustal rigidity G [e.g. *Stein and Wysession*, 2003]. The energy to moment ratios E_{bb}/M_0 for large global events range between 10$^{-4.8}$ and 10$^{-5.0}$ [*Choy and Boatwright*, 1995; *Newman and Okal*, 1998; *Weinstein and Okal*, 2005], which yields $\Delta\sigma$

estimates between 0.6 and 1 MPa assuming G = 30 GPa. Using the same conversion for the 2008 Achaia-Elia Earthquake, where $E_{bb}/M_0 = 10^{-4.1}$ (Figure 3.2), we find $\Delta\sigma$ = 5 MPa, a value that is between 5 and 10 times the global average. A nearby event (090216 in Figure 3.2) has $\Delta\sigma$ = 0.6 MPa, comparable to the global average, suggesting that the large stress-drop associate with the Achaia-Elia Earthquake is not due to regional changes in rigidity. (Herein, event identifiers represent the date of the event: YYMMDD). Explanations of such a high $\Delta\sigma$ include a relatively large or fast coseismic slip, which may be due to rupture of an immature fault containing little, if any, fault gouge [*Marone*, 1998].

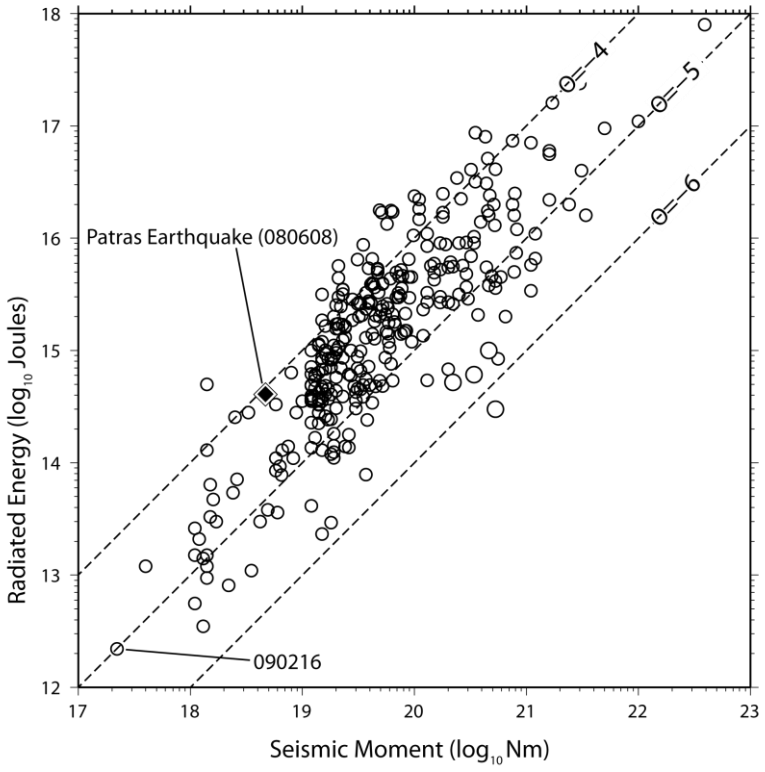

Figure 3.2: Distribution of radiated broad-band seismic energy to moment showing the relationship for most earthquakes (open circles) is near $E_{bb}/M_0 = 10^{-4.8}$ (figure after *Newman and Convers*, in review). The Patras event (filled diamond) is anomalously high in energy, with $E_{bb}/M_0 = 10^{-4.1}$, which can be explained by excessive $\Delta\sigma$, while a smaller M_W 5.5 event (090216) approximately 50 km away maintains an energy ratio similar to the global average.

It should be noted that the observed stress drop for this event is not significantly larger (less than a factor of 2) than the independently determined global average $\Delta\sigma = 3$ MPa from another global study that estimated results using precision determination of corner frequencies [*Allmann and Shearer*, 2009]. Though a direct comparison of average stress drops between this study and those of *Allmann and Shearer* [2009] cannot be made because of differences in methods, their findings of near an order of magnitude variance, and a factor of two or more increase in $\Delta\sigma$ of strikes-slip events is intriguing.

3.3 InSAR Coseismic Analysis

To explore the possible spatial extent of coseismic surface displacement, we utilized repeat passes of C-band ENVISAT (European Space Agency satellite) Synthetic Aperture Radar (SAR) phase data encompassing the coseismic period to construct Interferometric SAR (InSAR) images using ROI_PAC software [*Rosen et al.*, 2004]. Since the satellite's right-looking ascending (northward) path is advantageous for detecting NE-SW motion, ascending scenes on 16 Dec 2007 and 13 Jul 2008 (Figure 3.4a) are expected to be optimal, however, are largely decorrelated in the zone of interest. A second descending orbit pair was also examined with comparable areas of decorrelation. Unfortunately, in either image, little substantive information about the coseismic displacement could be obtained. However, regions near the projected fault plane maintain modest coherence in the ascending image, yet little interference consistent with coseismic activity is identifiable, implying buried and perhaps detached slip in the subsurface.

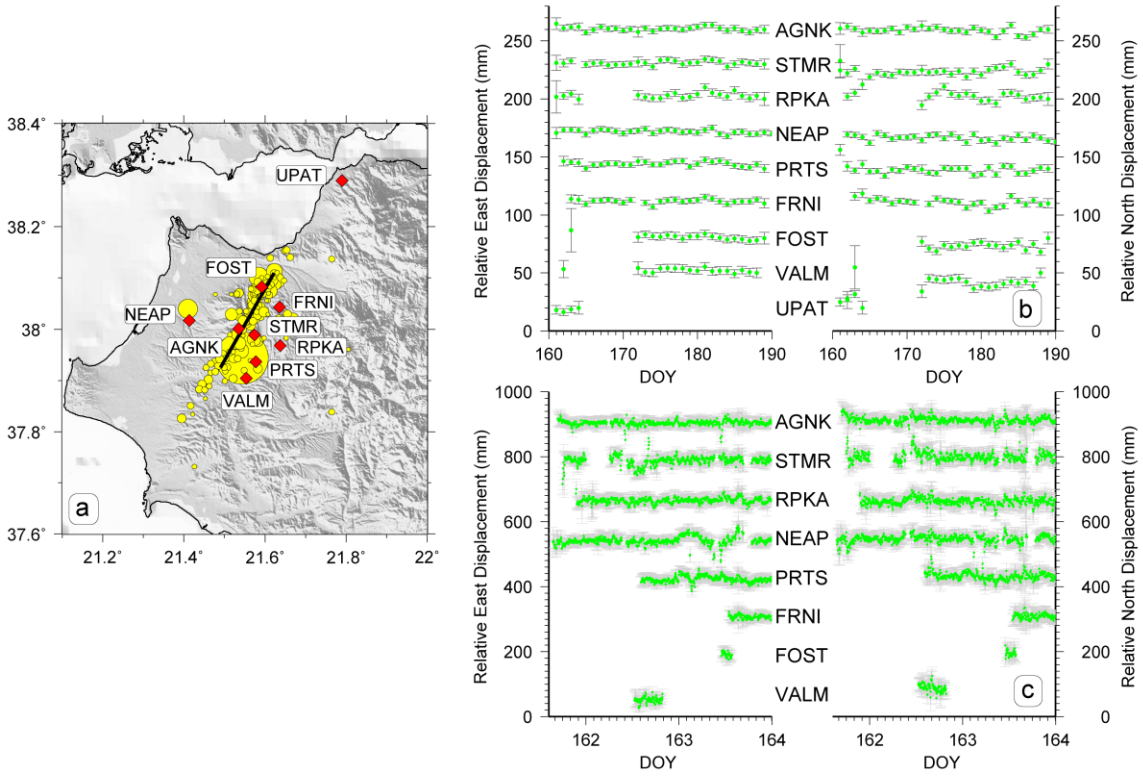

Figure 3.3: (a) Location of the temporary network of 9 continuous GPS sites (red diamonds). Thick solid line striking N30°E defined by the southern end [21.490°, 37.925°] and the northern end [21.633°, 38.120°] represents the approximately 25 km long projected fault trace estimated from mainshock and 1-day of aftershocks (yellow circles; AUTh catalog). (b) JPL-GIPSY daily solutions for postseismic period. (c) GAMIT-Track solutions for the first 3-days of recording. Data are 5-minute averaged 15-second kinematic solutions relative to site UPAT. Neither daily (b) nor rapid kinematic solutions (c) show discernible postseismic displacement across the network.

3.4 GPS Postseismic Analysis

To record possible postseismic surface deformation, a local network of 9 continuous GPS sites was rapidly deployed between 24 and 72 hours of the initial rupture, and maintained for approximately six weeks (Figure 3.3a). The sites including one base station at the University of Patras, and eight stations near the early aftershock locations. Sites were installed either on rooftops of visibly undamaged 1-2 story homes, or on exposed bedrock in open fields. Six weeks of daily point-position solutions were determined using JPL-GIPSY [*Zumberge et al.*, 1997]. For the initial 3-days, 15-second

kinematic solutions relative to site UPAT were determined using the Track software included with GAMIT/GLOBK [*Herring et al.*, 2008]. Even though numerous M_L 2-4 aftershocks continued in this region [*Ganas et al.*, 2009], no discernible early postseismic deformation was identified across the network using either daily solutions or rapid kinematic solutions (Figures 3.3b and 3.3c). Some shifts are observed in the kinematic solutions; however, they are mostly short-lived (less than 1-day), not correlated across stations, and are likely not tectonic in origin.

3.5 Discussion

The lack of coseismic surface rupture and significant surface deformation may be attributed to the increased depth of the 2008 Achaia-Elia Earthquake. The initial focal depth estimates varied significantly from 5 km to 38 km (Table 2 in *Ganas et al.* [2009]); however, the hypocenter depth was subsequently relocated with results between 18 km and 22 km [*Ganas et al.*, 2009; *Gallovič et al.*, 2009; *Konstantinou et al.*, 2009]. Since very few relocated aftershocks were below 25 km [*Ganas et al.*, 2009; *Konstantinou et al.*, 2009], 25 km is probably the lower limit of the base of the seismogenic zone.

To test whether the increased depth can explain the coseismic surface deformation deficit, we develop a series of uniform-slip vertically-dipping dextral fault models with different burial depths using Okada [1992] dislocation model. We fix seismic moment M_0 = 4.6×10^{18} Nm (determined by gCMT), fault length l = 25 km as identified by early aftershocks (see fault surface trace in Figure 3.3a), fault bottom at h = 25 km depth, and average crustal rigidity $G = 3 \times 10^{10}$ Pa. We then determine the average slip $\overline{D}$ required for an event occurring below a burial depth b, by

$$\overline{D} = \frac{M_0}{Gl(h-b)} \qquad (2.3)$$

where *h*-*b* represents the fault width *w*. The horizontal surface displacements along the line bisecting and normal to the fault trace for each model are calculated and plotted in the burial depth and fault normal distance space (solid curves in Figure 3.4c). Though a trade-off between *b* and $\overline{D}$ is necessary to maintain constant M_0, deeper burial requires lesser surface deformation. The horizontal surface deformation normally bisecting a fault ranges from almost 5 cm at 2 km burial to a little more than 1 cm at 10 km burial depth. Considering the fault length and allowing a generous bottom depth (25 km), a burial depth to 10 km is unlikely as it would create an unnecessarily large *l:w* aspect ratio. Alternatively, a more appropriate *b* ~ 5 km corresponding to the shallow extent of aftershocks to ~4 km [*Ganas et al.*, 2009]. At *b* = 5 km, the predicted horizontal displacement is > 2 cm between 3 and 13 km from the fault (Figure 3.4c), while vertical deformation would be highly variable but with cross-fault differentials of near 3 cm (Figure 3.4b). Such predicted displacements should be readily observable from InSAR. The only continuous GPS station running nearby during the 2008 Achaia-Elia Earthquake is the NOANET station RLS [*Ganas et al.*, 2009], located ~10 km away from the projected fault trace (Figure 3.4b). A northward motion of 7.3±0.3 mm was recorded at RLS [*Ganas et al.*, 2009], much less than ~20 mm that should be expected from a transform fault buried at 5 km depth (Figures 3.4b and 3.4c). The burial depth and downdip extent of the fault within a homogeneous elastic earth cannot explain the observed small surface deformation. Therefore, we argue that the compositionally weak, ~3 km thick flysch layer acts as a near-surface decoupling agent that isolates subsurface deformation from the surface.

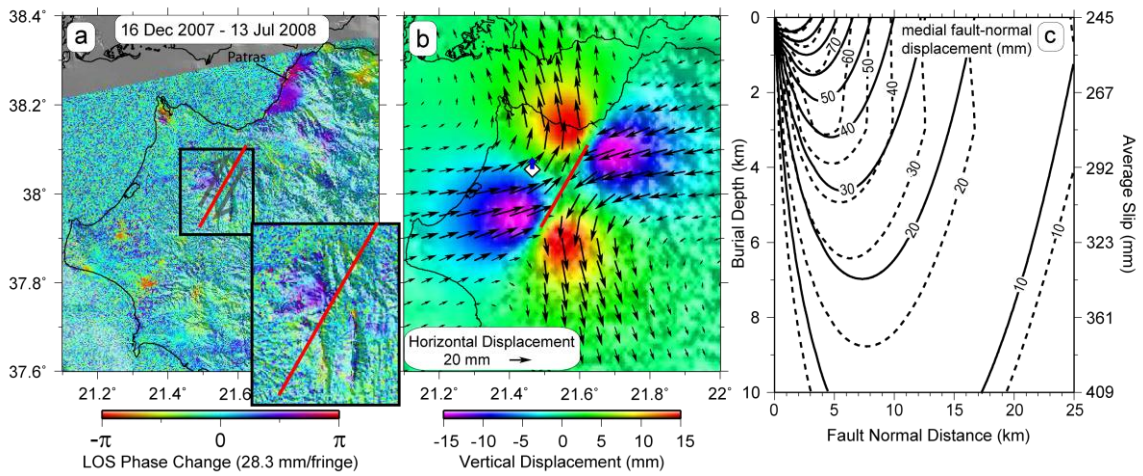

Figure 3.4: (a) The highly decorrelated ENVISAT ascending interferogram encompassing the 2008 Achaia-Elia Earthquake between 16 Dec 2007 and 13 Jul 2008. The color shows the line-of-sight (LOS) motion away from the satellite with 28.3 mm/fringe. Red line is the same surface projection of the fault as Fig. 3a. The inset is a blow-up of the near-fault region, and shows increased coherence. (b) The horizontal (black arrows) and vertical (colors) displacements as expected from a dextral fault (M_0 = 4.6x10^{18} Nm) buried at 5 km depth in a homogeneous half-space (G = 30 GPa) with both length and bottom depth of 25 km. White diamond shows the location of NOANET continuous station RLS. Blue arrow indicates the 7.26±0.28 mm northward motion of RLS during the earthquake [*Ganas et al.*, 2009]. (c) Predicted horizontal displacement (mm) normally bisecting the fault trace as described in (b) but with variable burial depth and average slip corresponding to M_0 = 4.6 x 10^{18} Nm. Homogeneous Okada half-space models show in solid curves; two-layer continuum models show in dashed lines.

Flysch is a sequence of syn-orogenic deep-marine terrigenous-clastic deposits [*van Hinsbergen et al.*, 2005]. The flysch deposits in NW Peloponnese were accumulated on top of the pre-orogenic Triassic to Eocene carbonates in the Gavrovo-Tripolitza and Ionian foreland basins mainly in the Oligocene during the overthrusting course of the Pindos and Gavrovo-Tripolitza nappes onto the Ionian zone caused by the collision-subduction between the Apulian and Eurasian plates [*Kamberis et al.*, 2000, 2005; *Sotiropoulos et al.*, 2003; *van Hinsbergen et al.*, 2005]. The average thickness of the flysch deposits is estimated to be approximately 3000 m from seismic and borehole

measurements [*Kamberis et al.*, 2005]. A portion of the Gavrovo-Tripolitza flysch is exposed in the middle part of the 2008 Achaia-Elia Earthquake region; while most of the flysch is covered by variously thick Pliocene-Quaternary sediments in the extensional basins rather than exposed at surface (Figure 3.1b).

Flysch is characterized by rhythmic alternations of sandstone and pelitic layers of varying rock strength [*Marinos and Hoek,* 2001]; however, it is typically weak and compliant with $G \leq 5$ GPa (estimated from *Marinos and Hoek* [2001]), much lower than carbonates, or granitic crust ~20-30 GPa [e.g. *Carmichael*, 1982]. To understand whether the reduced rigidity alone can explain the lack of coseismic surface deformation, we employ an elastic model that has a 3 km thick surface layer with reduced rigidity (G = 5GPa representing the flysch layer) over a stronger half-space (G = 30 GPa representing carbonates, or typical granitic crust) using Fortran programs EDGRN/EDCMP [*Wang et al.*, 2003]. Compared with homogeneous elastic models having the same fault parameters, the two-layer models allow for increased coseismic surface deformation (dashed curves in Figure 3.4c). Thus, we conclude a detachment between the seismogenic crust and the flysch layer would best explain the lack of significant observed surface deformation.

With lower overall stress, the compliant flysch may allow for an essentially decoupled cap, and hence lateral coseismic slip in the carbonates will not necessarily propagate through the flysch layer. A clear correlation between the strength of the geological formations and the existence of surface rupture was observed for the 1980 M_s 6.9 Irpinia normal earthquake in southern Apennines, Italy, where the surface faulting cut through carbonate platform rocks and was absent in the presence of thick flysch [*Bernard*

and Zollo, 1989; *Lyon-Caen et al.*, 1988]. Similarly, the detached surface layer may prohibit propagation of coseismic deformation to the surface as well. Strain in the flysch might be released independently by interseismic ductile deformation similar to that proposed by *Fialko et al.* [2005] for 2004 M_W 6.5 Bam earthquake in Iran, or fail in subsequent, smaller earthquakes.

Not only did the 2008 Achaia-Elia Earthquake have little discernable coseismic deformation, it had no perceptible early postseismic surface deformation from our GPS analyses. The most likely and potentially substantial candidate for fault-related deformation in the months that follow the mainshock is afterslip – aseismic slip driven by a stress perturbation that builds as coseismic rupture is arrested within the upper 4-5 km velocity-strengthening region [*Marone et al.*, 1991]. Afterslip is observed to exist in regions of coseismic slip deficit and is at times comparable or larger in magnitude than coseismic slip for mature transform faults, which may have thick unconsolidated gouge zones at shallow depths, or faults overlain by poorly consolidated sediments [*Marone et al.*, 1991; *Marone*, 1998]. The causal relation between unconsolidated fault gouge and afterslip suggests the 2008 Achaia-Elia Earthquake probably ruptured an immature fault without significant fault gouge that could favor afterslip. Instead, we suggest that the event had near complete coseismic slip along the seismogenically favorable fault at depth, but was unable to transmit significant stress to the potentially detached overriding flysch layer, making it unlikely to sustain any afterslip.

The 2008 Achaia-Elia Earthquake is the largest, but not the first strike-slip event in NW Peloponnese in recent history. Over 30 additional dominantly strike-slip crustal earthquakes with $M_W > 4$ have been identified between 1965 and 2009 in NW

Peloponnese and surrounding regions from published reports and earthquake catalogs (compiled in *Ganas et al.* [2009]; Figure 3.5). A diffuse series of NE-SW trending dextral transform faults sub-parallel to the southern branch of CTF can be interpreted according to the distribution and focal mechanisms of these earthquakes. The major transform fault on which the 2008 Achaia-Elia Earthquake occurred extends at least 40 km long crossing NW Peloponnese, and might connect with the recently active Rion-Patras fault (RPF) described by *Flotté et al.* [2005] to the north (Figure 3.5). To the south, its extension likely continues further south for another 40 km into the Ionian Sea (Figure 3.5). The dextral sense of motion on the major transform fault is widely accepted, however identification of fault and auxiliary planes was not clear for some events including 881016 (Kyllini) and 021202 (Vartholomio) earthquakes in the Zakynthos Channel, and 930926 (Pyrgos) earthquake. The NE-SW trending 10-day aftershocks and the NE-SW differential shear motion shown by the continuous GPS sites along the West Hellenic Arc [*Hollenstein et al.*, 2006] (Figure 3.5) suggest a dextral mechanism for each of the recorded events. The small, but widely spread, transform zone in the Zakynthos Channel is most likely restricted by a number of thrust events to the south and a possible more-rigid block to the north, as evidenced by low-seismicity rates [e.g. *Hatzfeld et al.*, 1990]. A similar wide spread transform zone is also observed in the Ionian Sea. The connection of the Ionian transform zone with the Pyrgos (930926) transform fault is not currently evident with the possibilities that either continuity between them or discontinuity by another small more-rigid block may exist. The 751231 earthquake near Lake Trichonis is likely a dextral slip event related to the Evinos fault (EF) just south of it. The newly recognized dextral shear zone had increasing activity over the past 30 years, and is

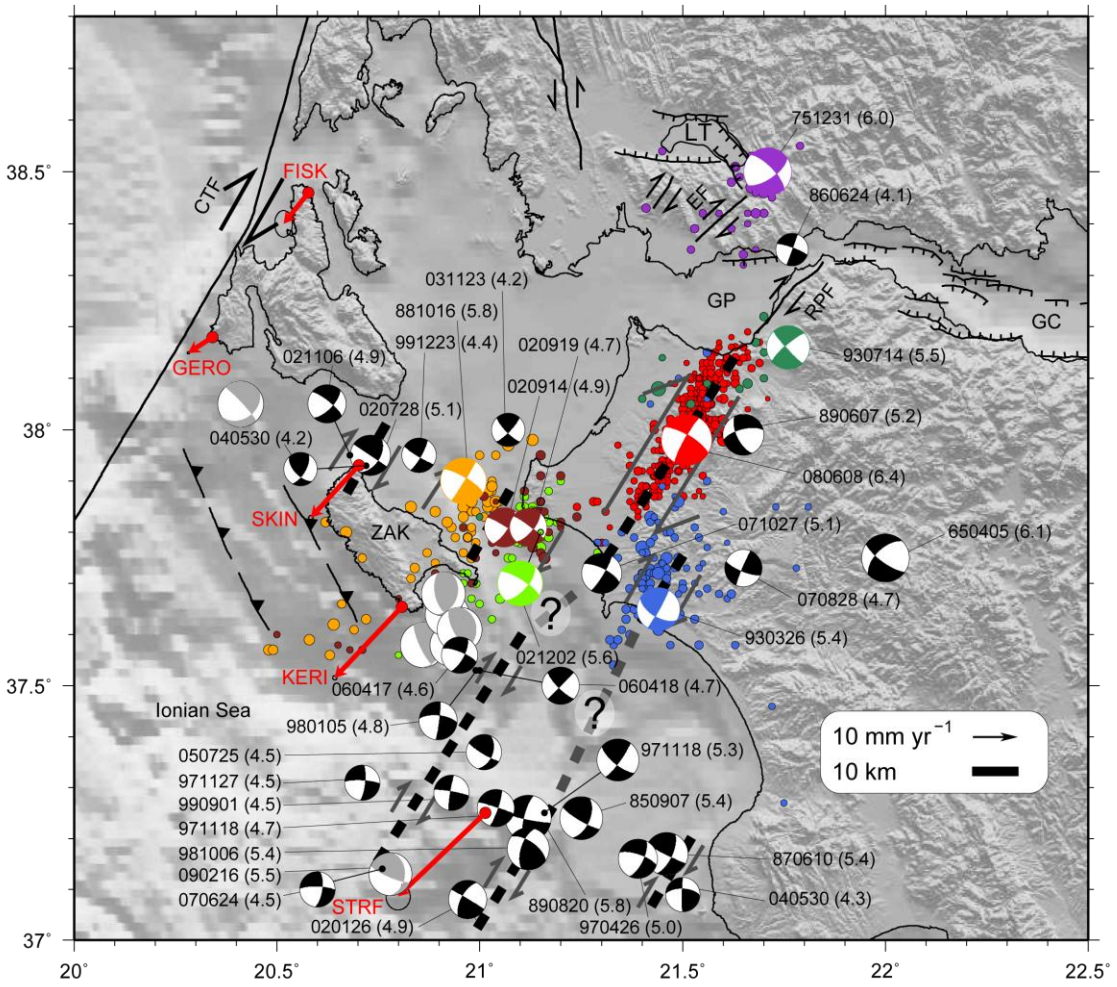

Figure 3.5: $M_W > 4$ strike-slip focal mechanisms in NW Peloponnese and surrounding regions. The seismic activity identifies a diffuse NE-SW trending transform fault zone in the crust (dark gray arrows and thick dashed lines). Most fault planes are solutions combined from gCMT 1976-2009, and European-Mediterranean Regional CMT (RCMT) 1997-2009 (*http://www.bo.ingv.it/RCMT*). Higher quality solution is used if the same event exists in both; gCMT solution is used if the quality flags are the same. *Benetatos et al.* [2004] (for events 650405, 850907, 870610, 890820, and 930714), *Kiratzi et al.* [2008] (for event 751231), and *Hatzfeld et al.* [1990] (for event 860624) are used as supplementary for missing events or events with low solution quality. Thrust earthquakes $M_W \geq 5.5$ in gCMT catalog are also plotted for reference. Event locations (beach-balls) and 10-day aftershocks (circles) differentiated by colors are taken from *Papanastassiou et al.* [2001] for earthquakes in 1950-2000 and from the National Observatory of Athens catalog (*http://www.gein.noa.gr*) after 2000. Faults are compiled from *Ferentinos et al.* [1985], *Louvari et al.* [1999], *Flotté et al.* [2005], *Lagios et al.* [2007], *Kiratzi et al.* [2008], and *Bell et al.* [2008]. Red arrows show the horizontal velocities of GPS sites along the West Hellenic Arc during 1995-2001 relative to Eurasia [*Hollenstein et al.*, 2006]. GC: Gulf of Corinth, GP: Gulf of Patras; ZAK: Zakynthos Island; CTF: Cephalonia Transform Fault; RPF: Rion-Patras Fault; EF: Evinos Fault; LT: Lake Trichonis.

potentially beginning to accommodate dextral shear between the Apulian and Aegean plates, similarly to the CTF.

Outside of some limited historical evidence of damaging events near Patras approximately 200 years ago [*Simopoulos*, 1985; *Stiros*, 1995; *Ambraseys and Jackson*, 1997], little is known about the earthquake potential and seismic hazard in the region. Hence, identification of the diffuse dextral shear zone that includes the 2008 event helps illuminate the internal deformation of the area. It is now evident that Patras, centrally located between this shear zone and the rapidly extending Gulf of Corinth, has significant seismic hazard. Because the rates of deformation and historic activity are poorly constrained, more effort is necessary to evaluate the long-term recurrence and near-term potential of a moderate to large transform earthquakes near Patras.

3.6 Conclusion

We identified the 8 June 2008 M_W 6.4 Achaia-Elia Earthquake to have a highly energetic rupture with teleseismic M_e between 6.8 and 7.2. Such large energy release is highly suggestive of a near order-of-magnitude increase in stress-drop over the global average. Field investigation of GPS, and analyses of InSAR images identify neither significant afterslip nor coseismic surface deformation, respectively. The contrasting increased shaking and lack of surface deformation can be explained by the existence of a thick and mechanically weak flysch layer covering the earthquake region that disassociates high-energy initial fault slip from the surface. The 8 June 2008 earthquake together with numerous smaller strike-slip events reveal an immature NE-SW trending dextral transform fault zone, which likely accommodates distributed shear between the central Ionian islands and NW Peloponnese.

CHAPTER 4

NORTHWESTERN COSTA RICA

4.1 Introduction

The Nicoya Peninsula on the Pacific coast of Costa Rica in Central America is one of the closest landmass (within 60-120 km) to the Middle America Trench (MAT). Offshore Nicoya the young oceanic Cocos plate (CO) is subducting underneath the Caribbean plate (CA) at a convergence rate of 82.3 ± 2.2 mm/yr and a direction of N20°E ± 2° according to the GPS-based PVEL model by *DeMets et al.* [2010] (Figure 4.1).

Owing to such a rapid subduction and the proximity to the trench, three devastating megathrust earthquakes (likely M > 7.5) have occurred directly beneath Nicoya in 1853, 1900, and 1950, respectively, following an approximate 50-year characteristic earthquake cycle pattern [*Protti et al.*, 2001]. However, only one large subduction thrust earthquake, the 1978 M_w = 7.0 Sámara earthquake, has occurred in Nicoya since 1950. The average slip of the 1978 event was estimated to be 71 cm [*Protti et al.*, 2001] that only accounts for 16% of the potential accumulated slip from 1950 to 2010 assuming 100% coupling. In contrast to the relatively quiet interseismic behavior of the Nicoya segment, the Nicaragua subduction segment just NW of Nicoya experienced a shallow M_w = 7.7 tsunami earthquake in 1992 [e.g., *Kanamori and Kikuchi*, 1993; *Satake*, 1994; *Ihmlé*, 1996] and the Nicoya Gulf entrance immediately SE of Nicoya was struck by a deeper M_w = 7.0 event in 1990 [*Protti et al.*, 1995; *Husen et al.*, 2002; *Bilek et al.*, 2009] (Figure 4.1b). Neither of these two earthquakes ruptured the Nicoya segment [*Protti et al.*, 1995] indicating the Nicoya segment is a prominent seismic gap with a large 1950-type earthquake missing (Figure 4.1b).

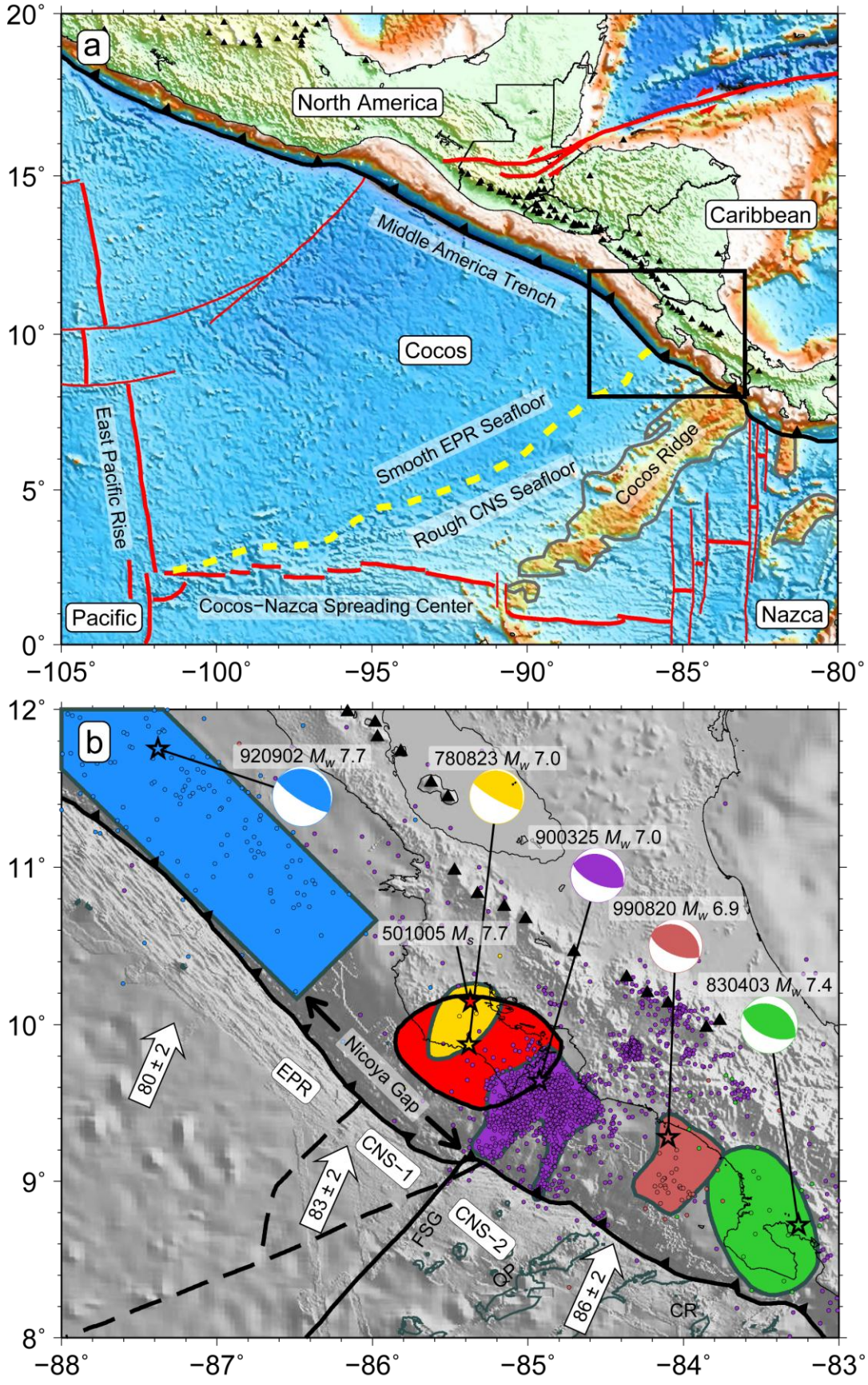
a
North America
Caribbean
Middle America Trench
Cocos
East Pacific Rise
Smooth EPR Seafloor
Rough CNS Seafloor
Cocos Ridge
Pacific
Cocos–Nazca Spreading Center
Nazca
20°
15°
10°
5°
0°
−105°
−100°
−95°
−90°
−85°
−80°
b
920902 M_w 7.7
780823 M_w 7.0
900325 M_w 7.0
990820 M_w 6.9
501005 M_s 7.7
830403 M_w 7.4
80 ± 2
EPR
Nicoya Gap
CNS–1
83 ± 2
FSG
CNS–2
CP
86 ± 2
CR
12°
11°
10°
9°
8°
−88°
−87°
−86°
−85°
−84°
−83°

Figure 4.1: (a) Regional tectonic map of Central America. Plates in this region include Cocos, Caribbean, Nazca, North America, and Pacific. Active spreading centers (thick red lines without arrows), fracture zones (thin red lines), the rough-smooth CNS-EPR boundary (yellow dashed line), and high-relief ridges (gray lines) are based on *Barckhausen et al.* [2001], *MacMillan et al.* [2004], and *Lonsdale* [2005]. Left-lateral transform faults (thick red lines with arrows) are taken from *Plafker* [1976] and *Rosencrantz and Mann* [1991]. Black triangles are volcanoes with evidence of Holocene activity [*Siebert and Simkin*, 2002]. Box outlines the area of Figure 4.1b. Bathymetry and topography use ETOPO2v2 Global Gridded 2-minite Database. (b) Large earthquakes in Nicoya and surrounding regions since 1950. Different color patches with stars as epicenters indicate rupture areas identified from aftershock distribution for 1950 Nicoya [Avants *et al.*, 2001; *Norabuena et al.*, 2004], 1978 Nicoya [Avants *et al.*, 2001; *Norabuena et al.*, 2004], 1983 Osa [*Adamek et al.*, 1987], 1990 Nicoya Gulf [*Protti et al.*, 1995], 1992 Nicaragua [*Ihmlé*, 1996], and 1999 Quepos [*DeShon et al.*, 2003] earthquakes. Circles are 3-month aftershocks from the OVSICORI seismic catalog for the 1990 event and from PDE for others. Focal mechanisms are from *Adamek et al.* [1987] for the 1983 event, from *Protti et al.* [1995] for the 1990 event, and the global centroid moment tensor (gCMT) catalog [Eskröm *et al.*, 2005] for others. Historically, the Nicoya segment has the largest thrust earthquakes ($M > 7.5$) in Costa Rica compared to moderate-magnitude ($7 < M < 7.5$) earthquakes in southeastern Costa Rica where the Cocos Ridge subducts and smaller-magnitude ($M \sim 7$) earthquakes in central Costa Rica where abundant small isolated seamounts subduct [Protti *et al.*, 1994; Bilek *et al.*, 2003]. Cocos-Caribbean convergence vectors (mm/yr) are derived from the PVEL model by *DeMets et al.* [2010]. Dashed lines are the boundaries separating seafloor spreading magnetic anomalies into EPR, CNS-1, and CNS-2; solid line is a propagator coinciding with the Fisher Ridge [*Barckhausen et al.*, 2001]. CNS, Cocos-Nazca spreading center; EPR, East Pacific Rise spreading center; CR, Cocos Ridge; FSG, Fisher Seamount Group; QP, Quepos Plateau.

The increasing risk of a potential large thrust earthquake striking Nicoya has been warned for two decades by scientists [e.g., *Nishenko*, 1991; *Protti et al.*, 1995]. Until recently, the discovery of transient slow-slip events [*Outerbridge et al.*, 2010; *Dixon et al.*, 2010], deep low-frequency earthquakes [*Brown et al.*, 2009], and non-volcanic tremors [*Outerbridge et al.*, 2010; *Walter et al.*, 2011] along the Nicoya segment complicated the characteristic earthquake cycle and raised a new question; that is, whether frequent silent transient slips have secretly released the accumulated strain over

the last 60 years. Nevertheless, >10 mm/yr subsidence along the coast observed by local residents [*Marshall and Anderson*, 1995] and geodetic studies [*Lundgren et al.*, 1999; this study] strongly suggests that the overriding plate is probably dragged down by a strong coupling with the subducting plate.

To investigate if long-term strong coupling indeed exists on the Nicoya subduction interface, we present a new interseismic megathrust coupling model based on the latest campaign and continuous GPS data. We also explore the possible relationships between megathrust earthquakes, microearthquakes, tremors, LFEs, and transient slips.

Slip vectors of shallow thrusting earthquakes at the CO-CA subduction zone are deflected 10 ° away from the plate convergence direction [*DeMets*, 2001, 2002]; consequently the non-negligible trench-parallel component from a high obliquity of ~22 ° near Nicoya needs to be partially taken in other ways. A forearc sliver extending from the diffuse Cocos-Caribbean-North American triple junction in southern Guatemala to the Central Costa Rica Deformed Belt (CCRDB) [*Marshall et al.*, 2000] has been proposed to accommodate portion of the trench-parallel motion by its W- to NW-directed transport relative to the Caribbean plate along the Central America volcanic arc [*Harlow and White*, 1985; *DeMets*, 2001]. Such a model is supported by frequent moderate-magnitude ($M \leq 6.5$) dextral strike-slip earthquakes in the upper crust along the volcanic front [*White and Harlow*, 1993; *DeMets*, 2001] and by strong trench-parallel component of motion recorded at GPS stations in southern Guatemala [*Lyon-Caen et al.*, 2006], El Salvador [*Correa-Mora et al.*, 2009; *Alvarado et al.*, 2011], Nicaragua [*Turner et al.*, 2007], and western Costa Rica [*Lundgren et al.*, 1999; *Norabuena et al.*, 2004; *LaFemina et al.*, 2009; this study] (Figure 4.2). Surface geological evidence also exists for the

forearc sliver including dextral strike-slip surface faulting observed in southern Guatemala [*Carr,* 1976; *Burkart and Self,* 1985] and central El Salvador [*Mart ńez-D áz et al.,* 2004; *Corti et al.,* 2005; *Agostini et al.,* 2006; *Funk et al.,* 2009; *Canora et al.,* 2010] as well as pull-apart basins formed at major step-overs of the volcanic arc in central El Salvador [*Corti et al.,* 2005; *Funk et al.,* 2009], the Gulf of Fonseca [*Funk et al.,* 2009; *Alvarado et al.,* 2011], and the Managua Graben of Nicaragua [*Weinberg,* 1992; *Girard and van Wyk de Vries,* 2005],

Although the existence of the Central America forearc sliver has been verified by various studies, a newly proposed hypothesis lately challenged the classic explanation of the driving mechanism. Instead of favoring oblique convergence with strong subduction interface coupling as the driving force [e.g., *Jarrard,* 1986a, 1986b], the recent hypothesis suggested another possibility that requires lateral crustal escape from the Cocos Ridge subduction offshore southern Costa Rica as the pushing force [*LaFemina et al.,* 2009] and weak interface coupling as the condition for freely translating of the Salvadoran and Nicaraguan forearcs as a single undeforming sliver [*Correa-Mora et al.,* 2009; *Alvarado et al.,* 2011].

As the second objective, we explore the Central America forearc sliver motion in NW Costa Rica using our new GPS dataset, propose possible boundaries for the forearc sliver, and also give some insight into the driving mechanism.

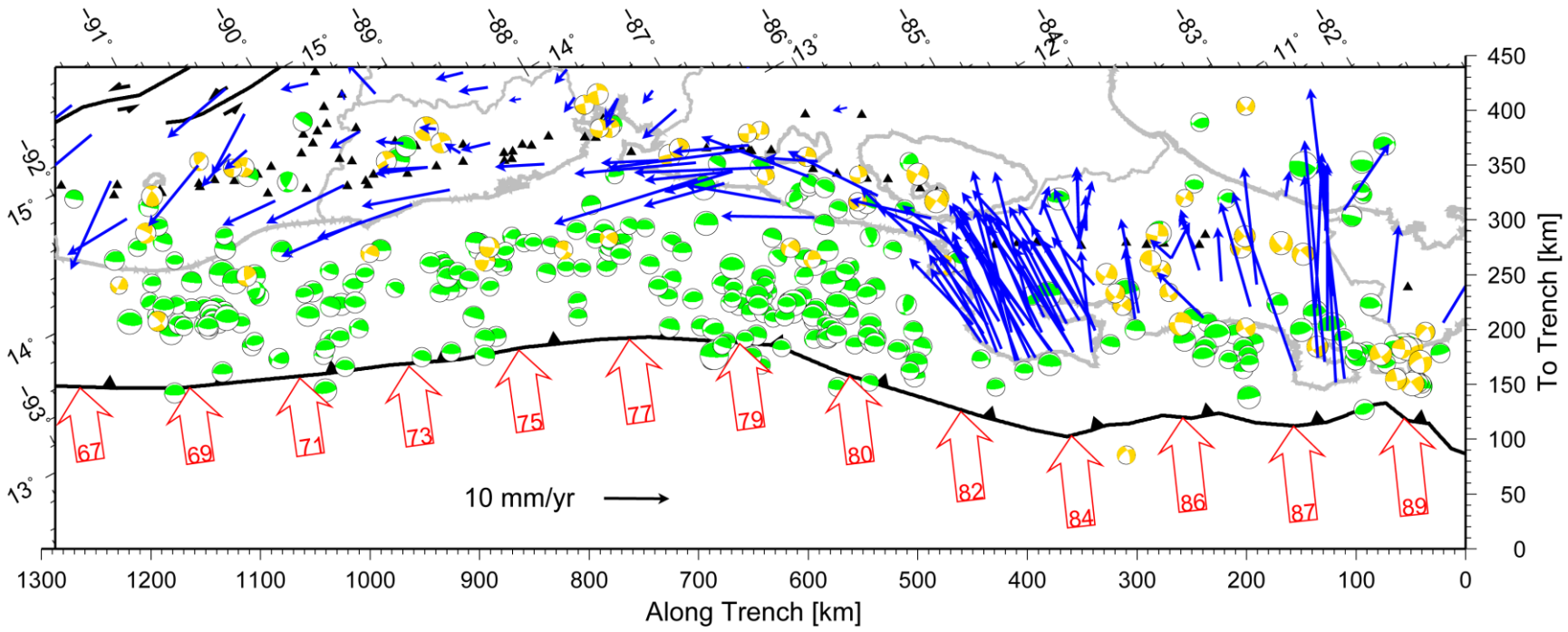

Figure 4.2: Focal mechanisms, GPS velocities, and Cocos-Caribbean plate motions along the Central America subduction zone. Focal mechanisms ($Mw \geq 5$) are taken from the gCMT catalog [Eskröm et al., 2005]. Strike-slip earthquakes (depth $\leq$ 30 km) are shown in yellow and thrust earthquakes (depth $\leq$ 70 km) are shown in green. Blue thin arrows show GPS velocities relative to the stable Caribbean compiled from Lyon-Caen *et al.* [2006], Rodriguez *et al.* [2009], Correa-Mora *et al.* [2009], LaFemina *et al.* [2009], and this study. Red thick arrows show plate convergence motion (mm/yr) derived from the PVEL model by DeMets *et al.* [2010]. Black triangles are volcanoes with evidence of Holocene activity [Siebert and Simkin, 2002].

4.2 GPS Data and Analysis

4.2.1 Campaign and Continuous GPS

The first Nicoya GPS campaign site was established at Liberia in 1988 as part of the first Central and South America campaign (CASA UNO) [*Kellogg and Dixon*, 1990]. Subsequent campaigns including CASA 1994 [*Lundgren et al.*, 1999], CASA 1996 [*Lundgren et al.*, 1999], Costa Rica 2000 [*Norabuena et al.*, 2004], and Costa Rica 2003 [*LaFemina et al.*, 2009] provide a long GPS campaign history for Nicoya. Campaigns were also carried out between 1997 and 2003 for three sites (PARK, GR38, and WARN) at Arenal Volcano, which is located east of Nicoya (Figure 4.3).

We performed the most recent GPS campaign in early March 2010 almost doubling the observation length since the last campaign in 2003. Twenty four existing campaign sites in both Nicoya and Arenal were reoccupied mostly for three consecutive UTC days. Four sites (AGUS, CORO, GUAR, and LOCA) have been destroyed before our 2010 campaign and CABU was missed (Figure 4.3), but their old data were retrieved. For the 2010 campaign, a combination of Trimble R7 and Trimble 5700 GPS receivers were used along with Trimble Zephyr Geodetic antennas. The recording interval is 15 seconds and the elevation mask is 5°.

The Nicoya continuous GPS network was initiated in 2002 with installing three stations (IND1, HUA2, and PUJE) along a NE-SW transect in central Nicoya and completed with a total of 19 stations in late 2009 [*Outerbridge et al.*, 2010] (Figure 4.3). Among the 19 stations, ELVI was precluded from the following analysis because of the receiver malfunction [*Dixon et al.*, 2010]. PNE2 is ~50 m away from an old site PNEG, but it had only one fifths of PNEG's duration and thus was also excluded. Although five

other sites (BIJA, CABA, EPZA, LAFE, and VERA) also had similar short duration of ~1 year (Figure B.4), they were kept in the analysis on account of their unique locations. Additionally, we included two continuous GPS stations (AROL and LOLA) that were operated from 1996 to 2003 for monitoring Arenal Volcano and another continuous site (IRZU) for *Irazú* Volcano from late 1999 to early 2003 (Figure 4.3).

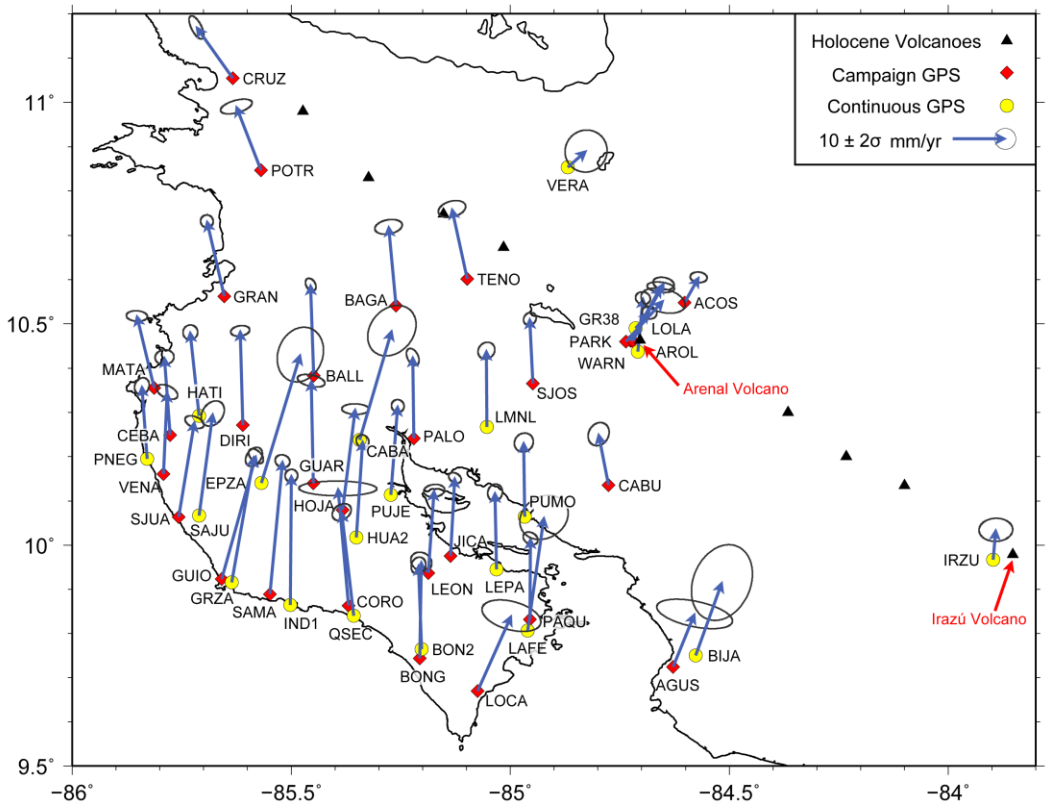

Figure 4.3: Map of campaign and continuous GPS stations. Vectors show horizontal velocities relative to the stable Caribbean plate [*DeMets et al.* 2010] between 1996 and 2010. 2-D 2σ error ellipses represent 86.5% confidence.

In summary, a total of 49 GPS stations including 29 campaign sites were used in this study covering the Nicoya Peninsula and a large area NE of it (Figure 4.3). Time series of all the 49 stations relative to the stable Caribbean plate are provided in Appendix B (Figures B.1-B.5). The average time span is 7.9 years. The average station spacing is 15-20 km for Nicoya and ~30 km more inland.

4.2.2 GPS Data Analysis

Using GIPSY 5 software from the Jet Propulsion Laboratory (JPL) along with precise satellite orbits and clocks provided by JPL [*Zumberge et al.*, 1997], all the data except the 1994 campaign that lacks JPL orbit and clock information were processed at the Geodesy Lab of the University of Miami. The resulting fiducial-free daily solutions [*Heflin et al.*, 1992] were converted to the International Terrestrial Reference Frame 2005 (ITRF2005) [*Altamimi et al.*, 2007]. To keep consistency between the campaign and continuous data, no filtering was implemented, but daily solutions with formal error larger than 3 times the average error were removed as outliers. The long-term interseismic velocities were estimated by iteratively fitting straight lines through individual components of the time series using a weighted least-squares method. In each iteration, outliers that have a deviation from the estimated linear trend larger than 3 times the weighted root-mean-square scatter (WRMS) were flagged and removed. The best fit rates were achieved until no more outliers can be identified.

The error calculation adopted an empirical noise model by *Mao et al.* [1999], which accounts for both the time-uncorrelated and time-correlated noises. This noise model was developed based on unfiltered data, thereby giving another reason for not imposing any filters to our time series. Individual noise contributions for the north, east, and vertical components were separately estimated from WRMS using equations given by *Dixon et al.* [2000]. Although the time series of the campaign sites were very irregular, the extremely long time span of data collected at most sites significantly reduced uncertainties. The resulting velocities with their corresponding errors relative to ITRF2005 are listed in Table 4.1.

Besides interseismic strain accumulation and forearc sliver motion, the two focuses of this chapter, other tectonic sources that may contribute to the raw time series include coseismic offsets, postseismic deformation, and aseismic transients.

Examining the Preliminary Determination of Epicenters (PDE) bulletin from National Earthquake Information Center (NEIC), no postseismic and coseismic signals were found to siginficantly contaminant the interseismic signal. *Norabuena et al.* [2004] showed the 1992 M_w = 7.7 Nicaragua tsunami earthquake is large and close enough to cause postseismic deformation of Nicoya; however, their estimate was <2 mm/yr for 1997. Given our observation period from 1996 to 2010, the postseismic response induced by the 1992 event is likely on the order of velocity uncertainty, thus not large enough to be considered as a signal source. During the observation, the largest local earthquakes beneath Nicoya are two M_w = 5.3 events at ~25 km depth in 2003 and the largest regional earthquake in the vicinity is the 1999 Quepos M_w = 6.9 event [*DeShon et al.*, 2003; *Bilek and C. Lithgow-Bertelloni*, 2005; *Moyer et al.*, 2011] (Figure 4.1b). All these earthquakes are either too small or too far to introduce any significant offset in the GPS time series.

Five slow-slip episodes have been observed near Nicoya with a rough recurrence interval of ~2 years [*Dixon et al.*, 2010]. The first episode, in early 2000, including three slow-slip transients propagating at the shallow subduction interface, was suggested by correlated flow rate transience detected across three flow meters at forearc frontal prism [*Brown et al.*, 2005; *LaBonte et al.*, 2009]. The transient signal was also accompanied with tremor-like noise recorded on collocated ocean bottom seismometers [*Brown et al.*, 2005].

Table 4.1: GPS interseismic velocities relative to ITRF2005[a] and the stable Caribbean plate[b]

Site	Lat (°N)	Lon (°W)	Height (m)	ΔT (yrs)	Days	Relative to ITRF2005 (mm/yr)						Relative to Caribbean (mm/yr)					
						N	1 σ	E	1 σ	U	1 σ	N	1 σ	E	1 σ	U	1 σ
Nicoya Campaign Sites																	
ACOS	10.5485	84.6024	300.52	14.07	50	11.8	0.3	16.0	0.7	0.1	1.2	4.8	0.5	2.7	0.8	-0.1	1.2
AGUS	9.7241	84.6284	70.55	3.01	8	17.0	1.3	17.8	3.6	6.9	5.9	10.1	1.4	4.1	3.6	6.7	5.9
BAGA	10.5414	85.2612	123.46	10.01	9	21.6	0.5	12.0	1.3	0.1	1.4	15.0	0.7	-1.4	1.3	-0.1	1.4
BALL	10.3834	85.4484	118.18	14.07	9	23.8	0.3	12.8	0.3	0.3	0.9	17.3	0.6	-0.6	0.5	0.0	0.9
BONG	9.7438	85.2069	21.40	10.04	11	25.0	0.8	14.0	1.0	-4.5	2.0	18.4	0.9	0.3	1.0	-4.7	2.0
CABU	10.1358	84.7756	499.18	7.26	10	16.6	1.0	11.7	0.9	0.4	2.5	9.7	1.1	-1.9	1.0	0.2	2.5
CEBA	10.2491	85.7761	90.32	10.06	11	21.3	0.5	12.4	0.8	-4.0	1.8	14.8	0.7	-1.1	0.9	-4.2	1.8
CORO	9.8630	85.3696	98.86	3.00	7	28.9	0.6	11.6	3.7	1.2	5.9	22.3	0.7	-2.0	3.7	1.0	5.9
CRUZ	11.0543	85.6337	267.24	14.10	13	16.2	1.0	6.2	0.6	-0.3	1.6	9.7	1.1	-6.9	0.7	-0.5	1.6
DIRI	10.2718	85.6106	82.04	10.06	13	24.5	0.3	13.0	0.8	-0.2	1.8	17.9	0.5	-0.5	0.9	-0.5	1.8
GRAN	10.5622	85.6530	122.36	14.09	17	20.8	0.3	10.0	0.4	-1.7	0.9	14.3	0.6	-3.3	0.6	-2.0	0.9
GUAR	10.1400	85.4497	135.44	7.04	6	26.1	0.3	13.2	1.2	-6.8	2.0	19.5	0.6	-0.4	1.3	-7.0	2.0
GUIO	9.9231	85.6585	31.18	10.02	10	29.9	0.5	20.1	0.6	-9.6	1.1	23.4	0.7	6.5	0.7	-9.9	1.1
HOJA	10.0795	85.3824	240.98	10.05	13	25.8	0.2	15.9	1.2	0.1	1.2	19.2	0.5	2.4	1.3	-0.2	1.2
JICA	9.9751	85.1360	61.45	14.07	14	21.6	0.3	14.4	0.4	-1.2	0.9	14.9	0.5	0.8	0.6	-1.4	0.9
LEON	9.9365	85.1868	276.88	10.00	9	22.4	0.4	14.7	0.9	-3.4	1.6	15.7	0.6	1.1	1.0	-3.6	1.6
LOCA	9.6701	85.0742	157.60	3.02	7	21.0	1.4	20.1	2.7	-1.9	3.8	14.3	1.5	6.4	2.8	-2.2	3.8
MATA	10.3553	85.8129	77.80	14.06	17	20.1	0.3	10.1	0.9	-3.6	1.1	13.7	0.5	-3.3	1.0	-3.8	1.1
PALO	10.2415	85.2203	40.19	10.03	10	22.2	0.6	13.3	0.5	-4.2	1.6	15.5	0.8	-0.2	0.6	-4.4	1.6
PAQU	9.8322	84.9551	80.31	14.08	13	22.1	0.4	13.8	0.5	-2.4	1.4	15.4	0.6	0.1	0.7	-2.7	1.4
POTR	10.8474	85.5691	155.80	10.05	15	18.6	0.6	8.6	1.5	0.2	1.7	12.1	0.7	-4.7	1.5	0.0	1.7
SAMA	9.8892	85.5488	45.57	14.05	11	31.8	0.4	16.0	0.6	-10.6	0.9	25.3	0.6	2.4	0.7	-10.8	0.9
SJOS	10.3656	84.9482	1062.24	14.10	12	19.0	0.4	12.8	0.5	0.1	1.2	12.3	0.6	-0.6	0.6	-0.1	1.2
SJUA	10.0632	85.7569	44.36	14.06	13	24.6	0.5	16.5	0.8	-7.7	1.1	18.1	0.6	3.0	0.9	-8.0	1.1
TENO	10.6018	85.0983	373.45	10.05	10	20.0	0.6	10.5	1.2	-1.6	2.1	13.3	0.8	-2.9	1.3	-1.8	2.1

VENA	10.1611	85.7917	24.76	10.03	11	22.1	0.5	14.2	0.9	-5.3	1.6	15.6	0.7	0.7	1.0	-5.5	1.6
Nicoya Continuous Sites																	
BIJA	9.7500	84.5769	555.63	0.80	294	20.8	3.6	18.7	2.9	12.8	9.2	13.9	3.6	5.0	2.9	12.5	9.2
BON2	9.7645	85.2025	27.97	5.32	1702	22.6	0.6	13.1	0.6	-4.6	1.5	15.9	0.8	-0.6	0.7	-4.8	1.5
CABA	10.2379	85.3435	26.96	0.96	353	27.4	2.3	19.5	2.3	3.2	7.8	20.8	2.4	6.1	2.3	3.0	7.8
EPZA	10.1409	85.5681	668.40	0.96	323	31.0	2.5	21.0	2.2	4.3	7.3	24.4	2.6	7.4	2.2	4.1	7.3
GRZA	9.9155	85.6356	39.32	4.25	1201	30.4	0.8	17.8	0.7	-11.2	1.8	23.9	0.9	4.2	0.8	-11.4	1.8
HATI	10.2922	85.7101	58.60	4.24	1543	22.4	0.6	11.8	0.6	-3.0	1.8	15.9	0.7	-1.7	0.7	-3.3	1.8
HUA2	10.0177	85.3517	593.92	6.90	2198	24.9	0.3	14.8	0.5	-3.2	1.1	18.3	0.6	1.2	0.6	-3.5	1.1
IND1	9.8646	85.5022	75.29	7.49	2368	31.2	0.4	13.8	0.4	-12.1	1.1	24.6	0.6	0.2	0.6	-12.3	1.1
LAFE	9.8071	84.9603	65.24	1.16	425	28.2	2.0	16.8	2.2	-14.0	7.3	21.5	2.1	3.1	2.3	-14.2	7.3
LEPA	9.9454	85.0312	20.93	4.37	1579	21.3	0.6	13.3	0.6	-0.1	1.9	14.6	0.8	-0.3	0.7	-0.3	1.9
LMNL	10.2675	85.0533	102.97	3.33	1216	21.2	0.7	13.4	0.7	0.1	2.4	14.5	0.8	-0.1	0.8	-0.1	2.4
PNEG	10.1955	85.8290	19.56	4.39	1501	20.2	0.6	12.5	0.6	-6.7	2.0	13.8	0.8	-1.0	0.7	-6.9	2.0
PUJE	10.1140	85.2725	30.11	6.77	2155	23.6	0.4	14.8	0.5	-2.5	1.1	16.9	0.6	1.3	0.6	-2.8	1.1
PUMO	10.0645	84.9667	17.96	3.16	1141	20.9	0.8	13.4	0.8	1.3	2.5	14.1	0.9	-0.2	0.9	1.1	2.5
QSEC	9.8404	85.3573	17.44	4.36	1355	26.4	0.7	11.4	0.8	-4.7	1.8	19.7	0.8	-2.3	0.9	-4.9	1.8
SAJU	10.0671	85.7106	73.44	2.47	903	25.9	1.1	16.2	1.0	-7.0	3.3	19.4	1.2	2.6	1.1	-7.3	3.3
VERA	10.8536	84.8690	64.32	1.13	413	10.0	1.9	16.7	1.9	-2.4	6.8	3.1	2.0	3.5	2.0	-2.7	6.8
Volcano Sites																	
AROL	10.4372	84.7092	754.01	7.86	1251	17.0	0.5	14.4	0.6	-4.3	1.4	10.2	0.6	1.0	0.7	-4.6	1.4
GR38	10.4619	84.7249	677.04	12.26	17	17.0	0.3	19.1	1.3	1.7	1.6	10.2	0.5	5.7	1.3	1.4	1.6
IRZU	9.9669	83.8975	2963.55	3.45	1152	12.9	1.0	14.1	1.6	3.3	3.7	5.7	1.1	0.5	1.6	3.0	3.7
LOLA	10.4901	84.7137	575.83	7.88	827	9.9	0.4	16.0	0.6	-4.5	1.3	3.0	0.6	2.6	0.7	-4.8	1.3
PARK	10.4602	84.7363	583.15	5.25	18	14.7	1.1	20.5	2.1	-1.2	4.2	7.8	1.2	7.1	2.1	-1.4	4.2
WARN	10.4619	84.7209	748.67	12.34	22	17.8	0.4	19.3	1.0	-3.8	2.8	10.9	0.6	5.9	1.0	-4.0	2.8

Lat, latitude; Lon, longitude; ΔT, observation length (yrs); Days, number of daily position; N, north; E, east; U, vertical; 1 σ , standard error (68% confidence). [a]ITRF2005 is defined by *Altamimi et al.* [2007]. [b]The conversion from ITRF2005 to Caribbean is taken from *DeMets et al.* [2010] with a correction for the translation of Earth mass center.

The second episode included two slow-slip transients initiated in May and September 2003, respectively. Both were observed first by three GPS sites on land [*Protti et al.*, 2004] and 2-3 weeks later by a stepwise pressure change in a prism toe borehole ~1 km landward of the trench [*Davis and Villinger*, 2006]. The best-documented episode is the May 2007 slow-slip event detected by the continuous GPS and seismic network in NW Costa Rica [*Outerbridge et al.*, 2010]. Two other episodes in mid-2005 and early-2009 were also observed by the Nicoya continuous GPS sites [*Dixon et al.*, 2010].

In recent interseismic studies, much effort has been spent on removing transient slip signals from time series for continuous sites and modeling corresponding offsets for campaign sites as long as such procedures are permitted by the data resolution [e.g., *Correa-Mora et al.*, 2008]. We simply chose not to remove any slow-slip signal. Because our major interest lies in determining long-term strain accumulation; that is to identify potential accumulated slip deficit on the subduction interface. Conversely, removing transient slip offsets adds the slips that have occurred back to the time series. A velocity increase of 30-50% can be obtained from removing slow-slip transients [*Correa-Mora et al.*, 2008; *Outerbridge et al.*, 2010]. By doing such a correction, what obtained is an intertransient coupling instead of an interseismic coupling (Figure 4.4). We suggest a clarification of "interseismic" and "intertransient". A proper selection of either totally depends on whether the research focus is megathrust coupling for only large earthquakes or interface coupling for both megathrust earthquakes and transient slips.

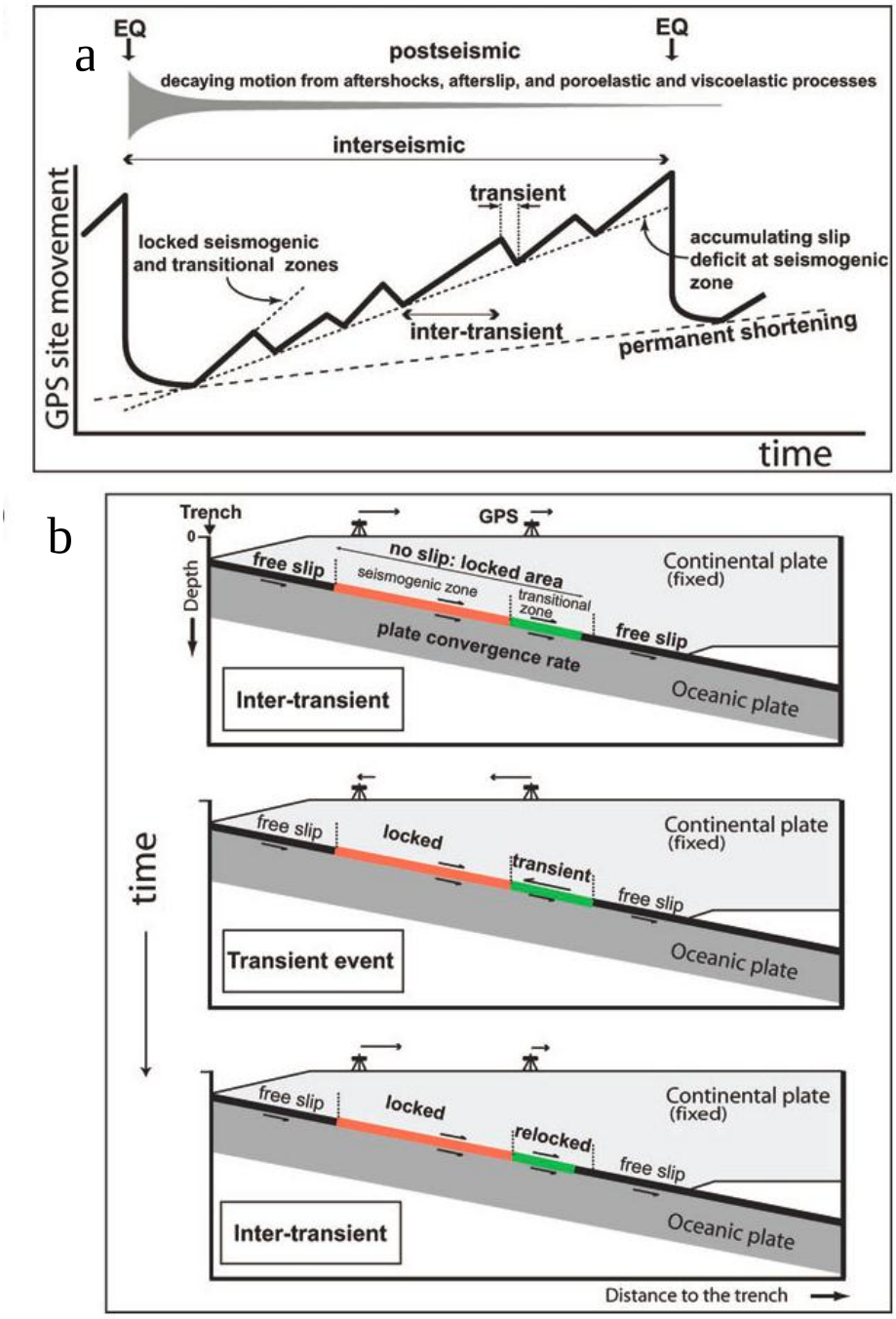

Figure 4.4: Schematic interseismic model. (a) Surface deformation with time during one seismic cycle. (b) Subduction interface behavior and surface displacement pattern in the interseismic phase of the seismic cycle including periods of transient slip superimposed on interseismic strain accumulation [adapted from *Correa-Mora et al.* 2008].

4.3 GPS Interseismic Velocities Relative to Caribbean

The interseismic velocities in the Caribbean reference frame (Table 4.1) were calculated using a CA-ITRF2005 Euler vector (36.9 °N, 98.9 °W, 0.261 °/Ma) and its covariance matrix with adjustment for the translation of Earth's center-of-mass relative to ITRF2005 [*DeMets et al.*, 2010]. The resultant horizontal velocities (Figure 4.3) indicate distinct behaviors of forearc and non-forearc sites. The non-forearc sites that includes six volcano sites (Table 4.1) and two sites (ACOS and VERA) NE of the volcanic arc have a relatively small residual with respect to Caribbean. The volcano sites may be affected by volcano activity, but ACOS and VERA are most likely to be on the stable Caribbean [*Lundgren et al.*, 1999]. On the other hand, the forearc sites located SW of the volcanic arc show an apparent counterclockwise rotation as observed by previous studies [*Lundgren et al.*, 1999; *Norabuena et al.*, 2004; *LaFemina et al.*, 2009], which is actually a result of forearc sliver motion superimposing on interseismic deformation. To separate the two types of motion, we project the horizontal velocities onto local trench-parallel and trench-normal directions.

4.3.1 Trench-parallel Velocities

The trench-parallel velocities of the forearc sites show a surprisingly uniform long-term displacement rate, while the trench-parallel velocities of the non-forearc sites fall to almost zero (Figure 4.5a). The velocity change occurs very rapidly within a 16-km-wide zone between the forearc and non-forearc sites (Figure 4.5a) in accord with the clustering of frequent strike-slip earthquakes within 20 km of the volcanic arc [*White and Harlow*, 1993]. Compared to an interseismic deformation zone of >200 km affected by locked strike-slip faults, as suggested by the screw dislocation model [*Savage and*

Burford, 1973] and observed on many transform fault systems [e.g., *Lyon-Caen et al.*, 2006; *Schmalzle et al.*, 2006], the observed transition zone in northern Costa Rica is very narrow. Presumably most of the shear strain induced from the forearc sliver motion is concentrated close to the Central America volcanic arc. Thus, the northern Costa Rican forearc sliver including area between the MAT and the volcanic arc translates as a rigid undeforming block.

Many previous GPS studies have demonstrated a northwestward sliver motion in northern Costa Rica, but their prediction of the translation rate differ from 5 ± 6 to 8 ± 3 mm/yr based on either sparse data [*Lundgren et al.*, 1999; *Iinuma et al.*, 2004] or simultaneously modeling of forearc and interseismic motions [*McCaffrey*, 2002; *Norabuena et al.*, 2004; *LaFemina et al.*, 2009]. Given longer observation period and better GPS coverage, we obtain a much higher average rate of 12 mm/yr (Figure 4.5a) in the preferred trench direction (N45°W) that aligns with the general physiographic trend of the trench offshore Nicoya (Figure 4.9b). The standard error of the weighted average rate is very small (<0.2 mm/yr), but it is calculated on the basis of a predefined trench and hence probably underestimated. To account for the uncertainty in the trench direction, we vary the trench strike by $\pm 5°$ from N45°W assuming the chance of having the strike outside this range is low. Accordingly, we find the average rate changes from 11 to 13 mm/yr suggesting an uncertainty of ~1 mm/yr.

Further north from Nicaragua to Guatemala where the coastlines lie farther away from MAT (>120 km), only trench-parallel motion is observed lacking NE-directed interseismic trench-normal motion (Figure 4.2). In Nicaragua, the mean velocity for forearc sites is 15.1 mm/yr toward NW [*Turner et al.*, 2007]. In El Salvador, a minimum

estimate of 9-10 mm/yr is suggested for the long-term slip rate across the volcanic arc [*Alvarado et al.*, 2011]. The Salvadoran and Nicaraguan forearcs have been shown to move together as part of the same crustal sliver at a rate of 15±2 mm/yr parallel to their respective trenches [*Alvarado et al.*, 2011]. In southern Guatemala, a slower differential motion of ~10 mm/yr is observed spanning the volcanic arc [*Lyon-Caen et al.*, 2006]. Our estimation of 12±1 mm/yr falls between 10 and 15 mm/yr. Interestingly, a late Pleistocene-Holocene slip rate of ~11 mm/yr across the El Salvador fault zone [*Corti et al.*, 2005] is closest to our observation. If such a slow-fast-slow variation in the forearc sliver motion is indeed true, the question is whether it occurs rapidly or gradually and how it is accommodated within the forearc.

The trench-parallel component of the CO-CA plate convergence from the PVEL model [*DeMets et al.*, 2010] is as high as 32 mm/yr beneath Nicoya, while our observation from the GPS data suggests only 12 mm/yr for the forearc translation rate. The large discrepancy (20 mm/yr) implies partial partitioning of oblique convergence into less oblique thrusting on the subduction interface and strike-slip motion along the volcanic arc [e.g., *Jarrard*, 1986a, 1986b; *McCaffrey*, 1992]. Despite of the existence of the forearc sliver, subduction thrust earthquakes still take ~60% of the trench-parallel convergence. Alternatively, from a seismological perspective, slip vectors of shallow thrusting earthquakes in Nicoya have been shown to be deflected ~8 °(read from Figure 1 of *DeMets* [2001]) clockwise from the convergence direction (N23 ºE from PVEL) toward the trench-normal [*DeMets*, 2001, 2002]. The trench-normal is N45 ºE for Nicoya, so slip directions are oriented between the convergence direction and the trench-normal suggesting partial partitioning again. Assuming the forearc moves parallel to the trench

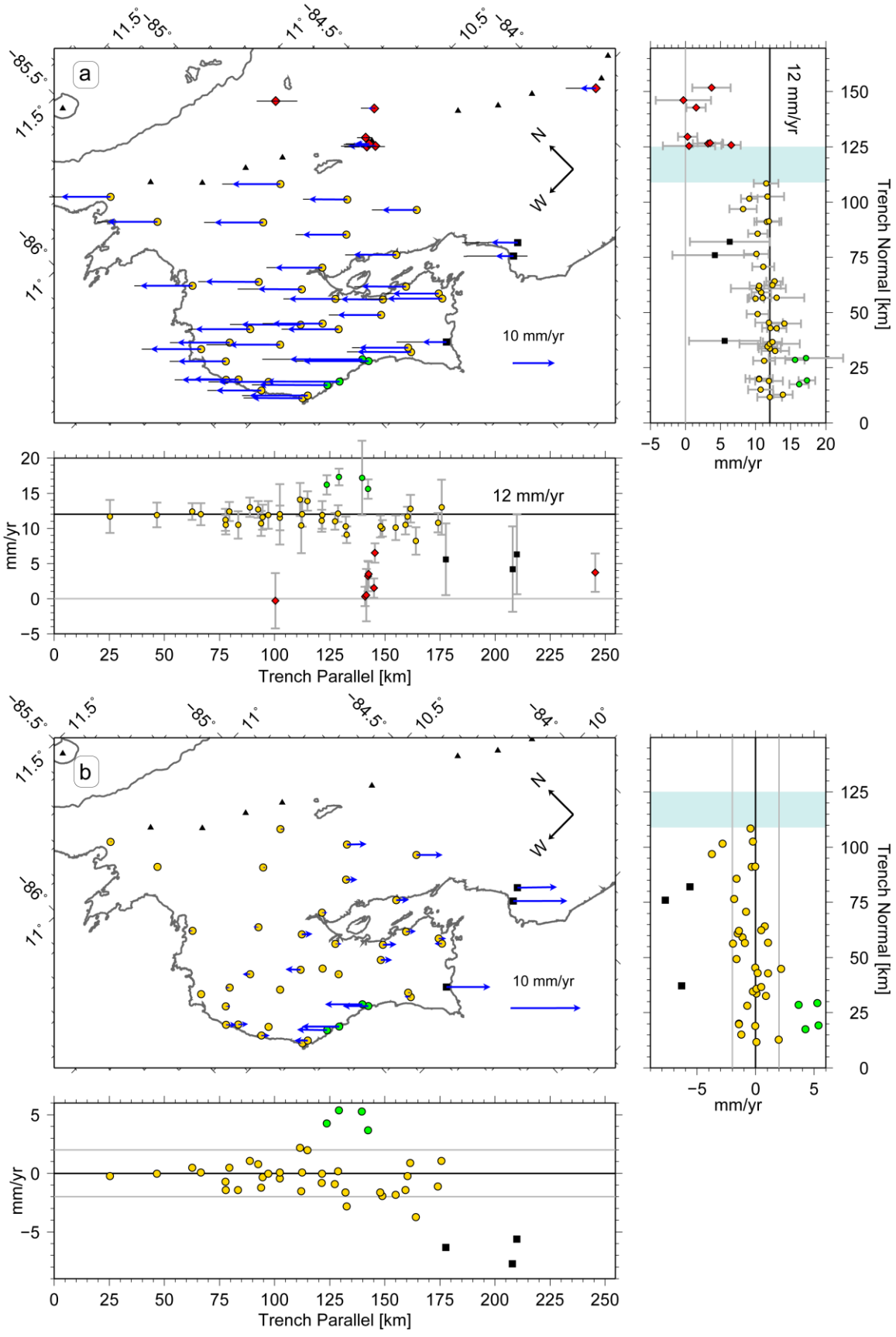
a
11.5°
-85°
11°
-84.5°
10.5°
-84°
-85.5°
-86°
N
W
10 mm/yr
12 mm/yr
mm/yr
Trench Parallel [km]
Trench Normal [km]
b
10°
-85°
-84.5°
-84°

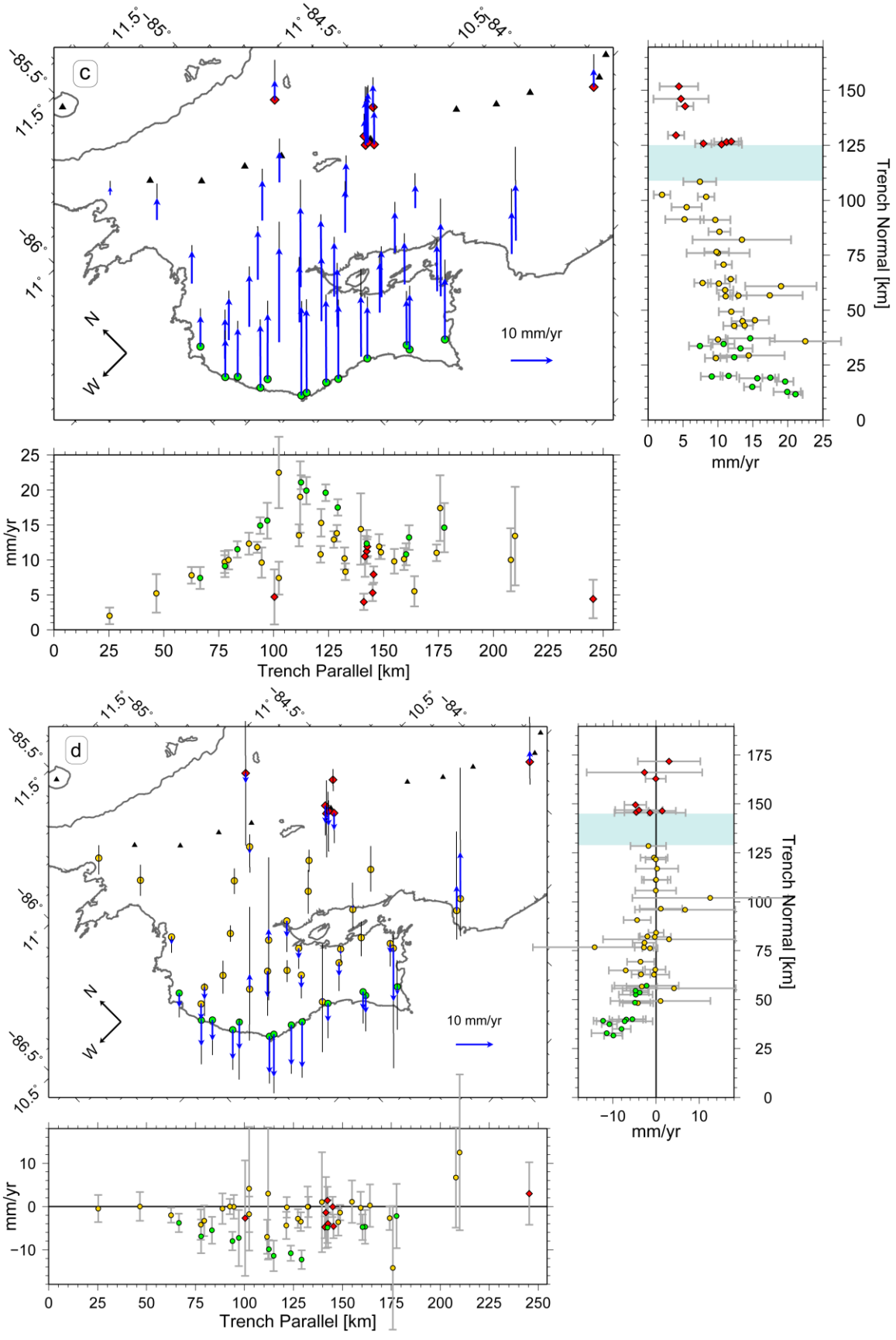
c
11.5°
−85°
11°
−84.5°
10.5°
−84°
−85.5°
11.5°
−86°
11°
N
W
10 mm/yr
mm/yr
Trench Normal [km]
Trench Parallel [km]
d
−86.5°
10.5°
−10
0
10

Figure 4.5: Interseismic velocities from 1996 to 2010 in the Caribbean-fixed frame [*DeMets et al.* 2010] are presented as (a) trench-parallel, (c) trench-normal, (d) vertical components, and (b) residuals of trench-parallel velocities with the 12 mm/yr forearc sliver motion removed. For each component, bottom panel plots velocities along a trench-parallel transect; right panel plots velocities along a trench-normal transect with the narrow velocity transition zone highlighted in light cyan. Trench direction is taken as N45°W. Yellow circles, the forearc sites; Red diamonds, the non-forearc sites; Green circles, the coastal sites, part of the forearc sites; Black squares, the sites with large residuals with respect to the northern Costa Rican forearc.

and slip directions align with N31°E, the rate of forearc sliver motion is estimated to be ~12 mm/yr following *DeMets* [2001]. This independently derived value agrees perfectly with our estimate from GPS observation.

After removing the average sliver motion, most residual velocities (Figure 4.5b) are <2 mm/yr indicating little internal deformation within the northern Costa Rican forearc. However, four coastal sites (green sites in Figure 4.5b) show up to 5 mm/yr deviation from the average. This variation is most likely from the strike-slip component of the interseismic strain accumulation. But if compared to a high strike-slip rate of 20 mm/yr that needs to be accommodated by thrust earthquakes, even 5 mm/yr is insignificant, not to mention residuals less than 2 mm/yr. Therefore, the oblique convergence probably does not contribute significant trench-parallel interseismic strain accumulation at the surface; however, a considerably large strike-slip motion would be simultaneously released when thrusting occurs on the subduction interface.

The residuals also reveal possible differential forearc motion SE of Nicoya. Three sites (black sites in Figure 4.5b) move 5-9 mm/yr slower than others suggesting that a potential extension zone may exist in the entrance of the Nicoya Gulf.

4.3.2 Trench-normal Velocities

The trench-normal velocities (Figure 4.5c) are dominated by elastic interseismic strain accumulation of the upper plate resulting from frictional coupling of the subduction interface. Generally, the coastal sites (green sites in Figure 4.5c) show the largest trench-normal velocities indicating largest coupling offshore with a peak at the elbow of the coastline coincident with the rough-smooth boundary that separates oceanic crusts generated at the Cocos-Nazca spreading center (CNS) and the East Pacific Rise (EPR) [*Barckhausen et al.*, 2001]. The trench-normal velocities decay gradually toward inland and flatten out at ~5 mm/yr for the most inland sites. No apparent difference is observed across the volcanic arc.

4.3.3 Vertical Velocities

Similar to the trench-normal velocities, the vertical velocities (Figure 4.5d) mainly originate from the interseismic strain accumulation. The coastal sites (green sites in Figure 4.5d) have the largest subsidence rate >10 mm/yr indicating a strong coupling offshore. We do not observe any clear transition from subsidence to uplift. Most remaining sites show essentially zero vertical motion.

4.3.4 Velocity Comparison

Several previous studies including *Lundgren et al.* [1999], *Iinuma et al.* [2004], *Norabuena et al.* [2004], and *LaFemina et al.* [2009] have determined interseismic velocities relative to the Caribbean plate for sites in northern Costa Rica. We compare our results with the most recent published velocities from *LaFemina et al.* [2009]. The differences are primarily within the errors (Figures 4.6a and 4.6b), so no further conclusion can be drawn.

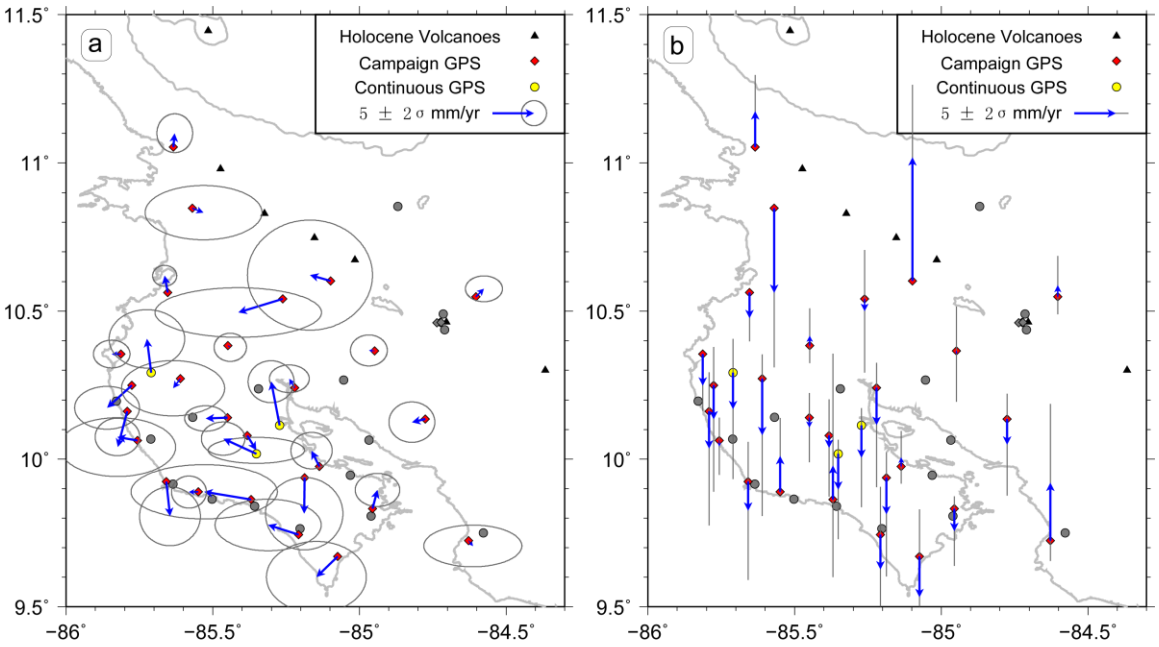

Figure 4.6: 1996-2010 interseismic velocities relative to stable Caribbean from this study subtracted by 1993-2005 velocities from *LaFemina et al.* [2009]. (a) Horizontal velocity differences and (b) Vertical velocity differences.

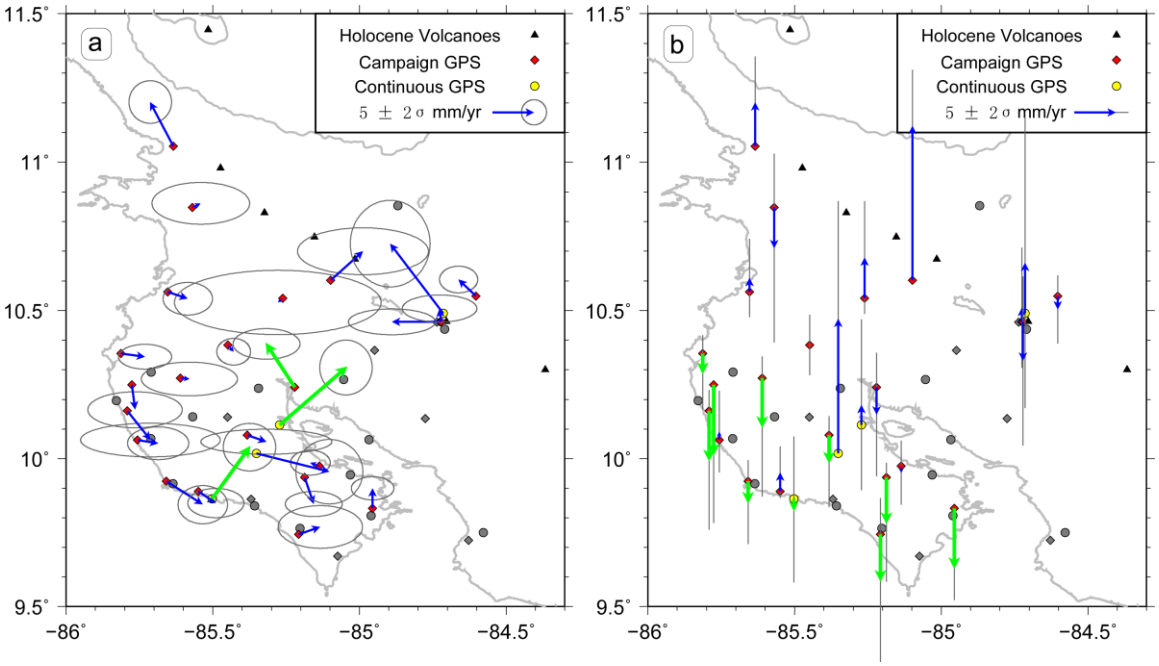

Figure 4.7: Velocity differences in the Caribbean frame between 2003-2010 and 1996-2003 periods from this study. (a) Horizontal velocity differences. Continuous sites IND1, HUA2, and PUJE (green vectors) show more northeastward or eastward motion in 2003-2010 than in 1996-2003. (b) Vertical velocity differences. Most costal sites (green vectors) show more downward motion in 2003-2010 than in 1996-2003.

4.3.5 Temporal Variation

To investigate if any temporal variation exists, we divided the observation time from 1996 to 2010 into two 7-year-long periods that are 1996-2003 and 2003-2010. Because the last campaign before our 2010 campaign was conducted in 2003, the data in 2003 were included in both periods. We subtracted the interseismic velocities in 1996-2003 from those in 2003-2010 (Figures 4.7a and 4.7b). The random orientations of the difference arrows do not support any consistent pattern, and the differences for most sites are smaller than their errors, hence the temporal resolution of our data is not enough to confidently suggest any temporal variation. However, continuous sites like IND1, HUA2, and PUJE, which have the longest observation time, show more northeastward or eastward motion (>5 mm/yr) in 2003-2010 than in 1996-2003 (green vectors in Figure 4.7a), which might indicate increasing interseismic coupling with time. Other potential evidence includes more downward motion for most costal sites in 2003-2010 than in 1996-2003 (green vectors in Figure 4.7b).

4.4 Forearc Sliver Transform Fault Model

As we showed in 4.3.1, the forearc sliver in northern Costa Rica translates northwestward as a whole ridge block, while a velocity change of up to 12 mm/yr occurs within a narrow deforming zone of ~16 km wide. The question is how a transform fault that bounds the forearc sliver accommodates such a rapid change. Without knowing much about the transform fault system, we conduct a grid search for fault location, slip rate, and locking depth using only the trench-parallel velocities of the forearc sites. A simple screw dislocation model [*Savage and Burford*, 1973] is used assuming the strike-slip fault is infinitely long and vertically dipping. Velocities are calculated using

$$v = \frac{b}{\pi}\arctan\left(\frac{x}{D}\right) \qquad (4.1)$$

where D is locking depth, b is slip rate, x is the distance to fault, and v is the strike slip displacement. The obtained velocities are then used to calculate reduced Chi-square χ_r^2.

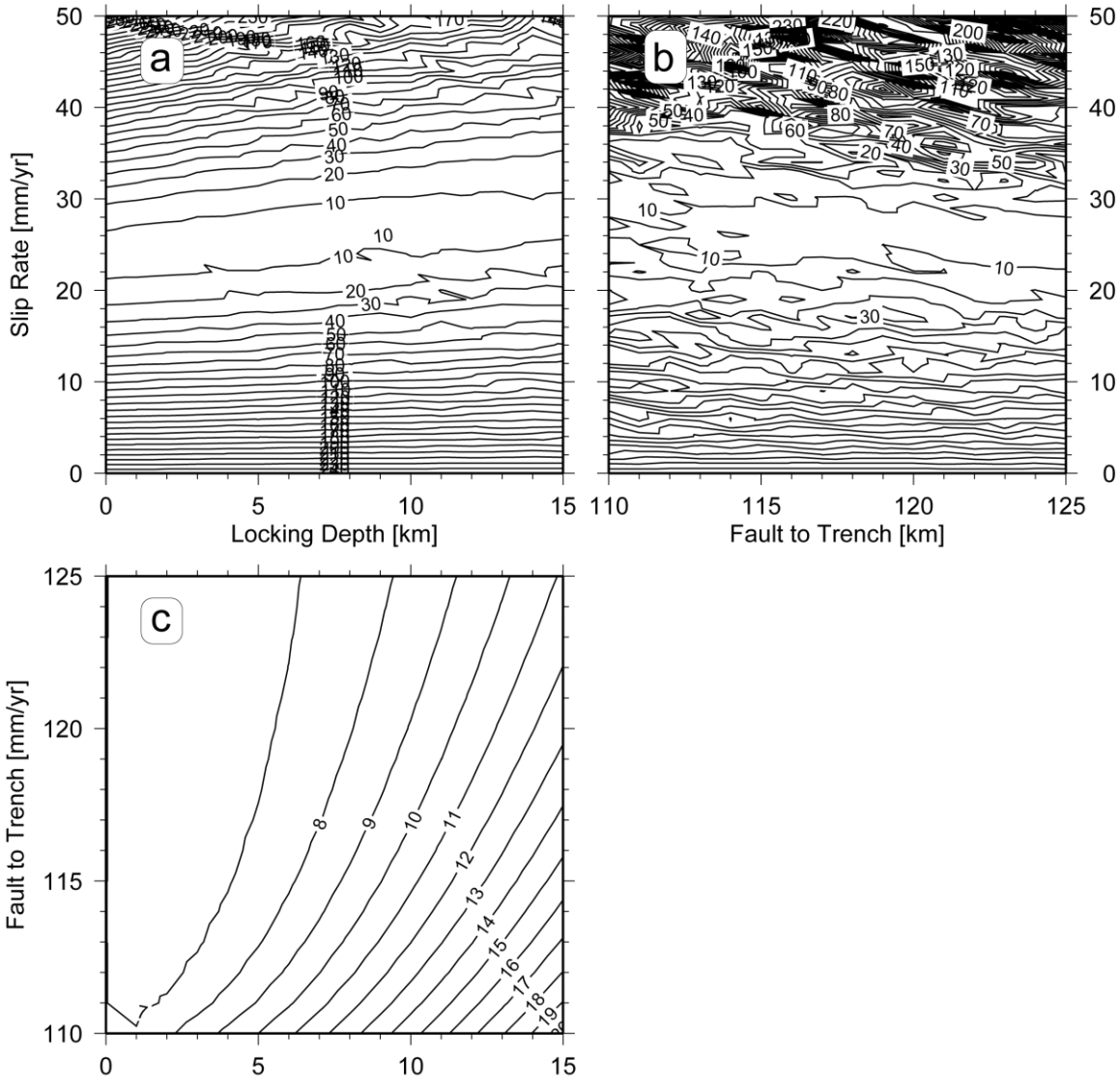

Figure 4.8: Grid search results for the forearc sliver transform fault: (a) contours of χ_r^2 for the pair of locking depth and slip rate; (b) contours of χ_r^2 for the pair of fault location and slip rate; (c) contours of χ_r^2 for the pair of locking depth and fault location.

Because our station distribution is designed for studying megathrust, it is not ideal for observing strike-slip motion. All our stations are outside the high velocity gradient zone (light cyan shaded zone in Figure 4.5). Thus only slip rate is well constrained at 24-26 mm/yr (Figures 4.8a and 4.8b). Note this value is twice as large as our trench-parallel average, because the dislocation model assumes a symmetrical fault with two sides move equally in the opposite direction, but only the forearc side moves in our case. We cannot accurately determine fault location and locking depth from the current data. When moving the fault across the transition zone, locking depth varies from 2 km to 6 km (Figure 4.8c). This shallow depth range is within the depth range of upper-crustal earthquakes along the Central America volcanic chain from 1 to 20 km with the majority between 3 and 15 km [*White and Harlow*, 1993]. A shallow locking depth seems to be required to accommodate the narrow high velocity gradient in northern Costa Rica. The existence of volcanic systems probably shallows the brittle-ductile transition [*Gourmelen et al.*, 2011] and allows creep occur shallower.

4.5 Interseismic Megathrust Coupling Model

We employed the widely used back slip model proposed by *Savage* [1983] to represent the interseismic strain accumulation induced by coupling on the subduction interface. In the back slip model, virtual "normal" slip on the coupled region indicates slip deficit, i.e., slip less than full plate motion. We assumed the interseismic strain accumulation is purely elastic and will be released in the next large earthquake without causing any permanent deformation in the upper plate.

4.5.1 Model Input Data

As discussed in section 3.3.1, the horizontal signals from the interseismic strain accumulation are dominated by the trench-normal component with little contribution from the trench-parallel. Therefore, we used only the trench-normal and vertical velocities to invert for slip distribution across the subduction interface. Although vertical uncertainties are 2-3 times larger than horizontal uncertainties, vertical velocities have a better capability of constraining the downdip limit of the locking zone [*Lundgren et al.*, 1999]. Moreover, the 15-year-long observation duration allows us to obtain relatively reliable vertical measurements for the first time in northern Costa Rica, so the vertical components were also included in the following modeling.

4.5.2 Model Geometry

The 3-D geometry of the plate interface was derived from the well-located plate interface and slab seismicity [*Ghosh et al.*, 2008] using the maximum seismicity method [*Thomas et al.*, 2007]. Although steepening of the plate interface from CNS to EPR has been observed above ~20 km depth [*DeShon et al.*, 2006], we simplified the interface using planar row segments that have an increasing dip with depth as a first order approximation. To construct a representative 2-D cross section perpendicular to the trench, we used a function that comprises of a straight line at shallow depth and a parabolic curve at deep depth to fit the 3-D interface beneath Nicoya down to 100 km depth. The best fit smooth curve was then discretized into planar row segments of ~5 km width to ~60 km depth (Figure 4.9a). As a result, the fault interface is approximated by 30 connected planes with a changing dip. The dip is 11.4 ° at the trench depth of 4.5 km below sea level, stays constant to 18.6 km depth, and gradually increases to 48.1 ° at the bottom depth of 62 km. Because our stations are all on land, to account for the

inconsistency between trench depth and sea level, an imaginary row is added to extend the interface to the sea level (Figures 4.9a and 4.9b). A comparison of our interface with two others by *Norabuena et al.* [2004] and *DeShon et al.* [2006] shows small differences down to ~30 km depth and increasing discrepancies at deeper depth (Figure 4.9a), presumably because we included deep slab seismicity down to 100 km to constrain the curvature of the interface at depth.

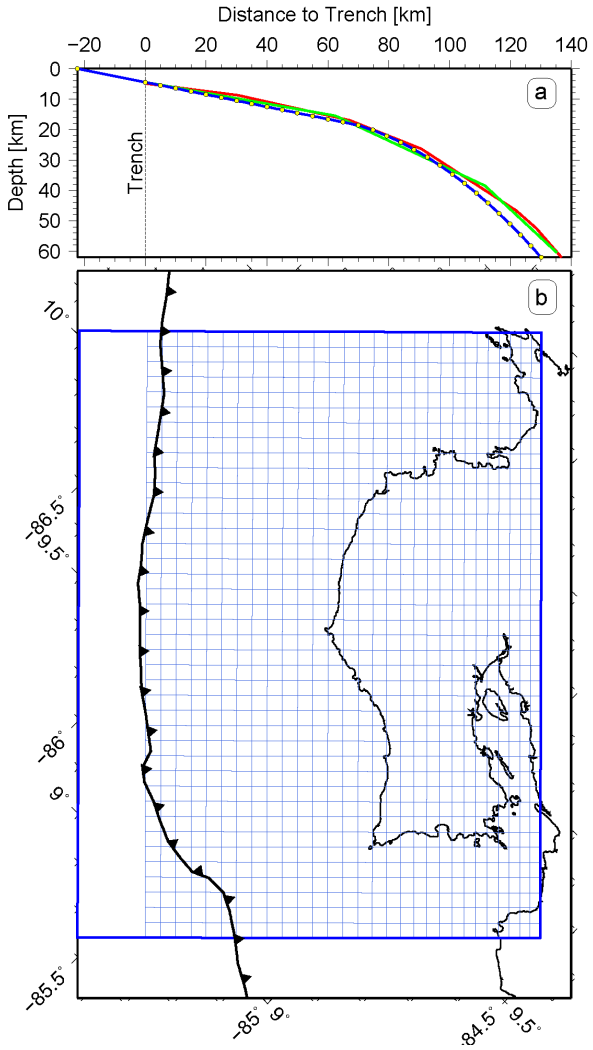

Figure 4.9: Interseismic megathrust coupling model geometry. (a) Cross section of the subduction plate interface used in modeling (blue line) with yellow circles denoting the ends of planar row segments. Green line represents the model interface used by *Norabuena et al.* [2004]. Red line is the generalized subduction interface from Figure 10 in *DeShon et al.* [2006]. Zero depth is at sea level and trench is 4.5 km below sea level. (b) Surface projection of the fault interface and its individual patches.

In contrast to the varying dip, the strike of the interface was fixed at N45°W. Assuming a length of 200 km along strike, the model area not only covers the Nicoya Peninsula but also extends laterally far enough to avoid edge effects. The interface was also discretized into 5-km-wide segments along strike (Figure 4.9b).

In summary, the assumed fault is composed of 30×40 rectangular patches extending 200 km long and ~60 km deep with each patch covering roughly 5×5 km^2 area on the interface.

4.5.3 Model Formulation and Inversion

Green functions were calculated for the north, east, and vertical displacements of 43 GPS stations (excluding six volcano sites) imposed by unit uniform dip-slip on each patch using the Okada model [*Okada*, 1992]. By linear superimposing contributions from each patch, total deformation at each site can be obtained.

Back (normal) slips alone were inverted in the models and their values were only allowed to vary between zero and the trench-normal component of the CO-CA convergence at the center of each patch. We refer the ratio of back slip rate to local trench-normal convergence rate as the degree of coupling across the plate interface, which is a kinematic estimate and not directly related to friction. A back slip at the trench-normal convergence rate represents fully coupling, while a zero back slip indicates freely slipping. The slips at the top boundary of the fault are set to vary freely, but the slips at the bottom and side boundaries are fixed at zero back slip implying freely slipping.

To solve this underdetermined problem with more unknowns (30×40=1200) than observations (43×3=129), two-dimensional (along strike and dip) second-derivative

(Laplacian) smoothing [*Harris and Segall*, 1987; *Jónsson et al.*, 2002] was applied to fault slips. Smoothing spatially links slips on adjacent patches to avoid unrealistic highly variable slip distribution [*Chen et al.*, 2009]. Additionally, two-dimensional first-derivative stress minimization smoothing method was also tested [*Feng et al.*, 2009]; however, the results are not significantly different from the traditional Laplacian smoothing method, thus the details of stress minimization are only explained in Appendix C.

Combining the constraints from data and smoothing, we seek to solve the linear equation system below that relates slips to surface deformation using MATLAB lsqlin function.

$$\begin{bmatrix} w^{-1}d \\ 0 \end{bmatrix} = \begin{bmatrix} w^{-1}G \\ \kappa^2 D \end{bmatrix} m \qquad (3.2)$$

where d is the observation vector including north, east, and vertical components, m is the unknown slip vector including back slip only, w is the diagonal matrix constructed from observation errors, G is the green function matrix, D is the second-order finite difference operator [*Jónsson et al.*, 2002], κ^2 controls the weight imposed on the smoothing.

The use of different weights on smoothing leads to different model results, so no single solution exists. Increasing smoothing is always accompanied with a cost of reducing model misfit; therefore we visually inspected the trade-off curve between model misfit and roughness to determine a preferred model [*Du et al.*, 1992]. The root-mean-square (RMS) of the weighted residual sum of squares (WRSS) is used to quantify model misfit, while model roughness, the average second-order finite-difference sum of each patch [*Jónsson et al.*, 2002], is used to represent the degree of smoothing.

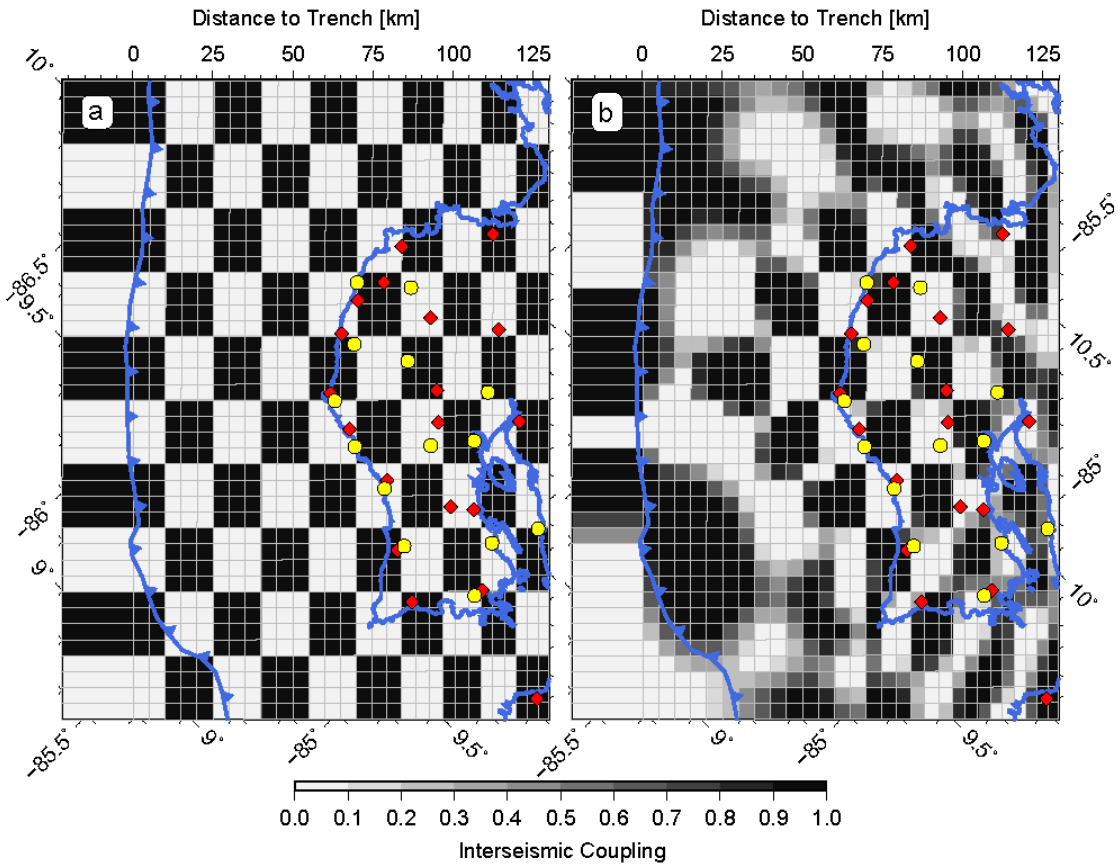

Figure 4.10: Checkerboard test on the spatial resolution of the dense Nicoya GPS network. (a) Synthetic input slip distribution used to create a synthetic deformation field. (b) Output slip distribution inverted from the synthetic surface deformation. Red diamonds are campaign sites. Yellow circles are continuous sites.

4.5.4 Checkerboard Resolution Test

We first conducted a checkerboard resolution test to access the spatial resolving capability of the Nicoya GPS network on the assumed fault geometry. Because the network has an average station spacing of 15-20 km, which suggests the capability of resolving slips with similar scale, we divided the fault interface into patches of 15×20 km^2 area, assigned alternating zero and full convergence back slips to them as a synthetic input (Figure 4.10a), and calculated the displacements at our stations from this input. Uncertainties of the real data were added to the synthetic displacements before inverting

for slips. As expected from the dense coverage, the preferred model at $\kappa = 400$ recovers all the patches beneath Nicoya and other patches within ~25 km distance to the coastline, but loses resolution dramatically toward the trench where no GPS sites exist and at greater depth where fewer sites are available (Figure 4.10b).

4.5.5 Model Results

We then ran inversion models using a wide range of smoothing parameters. The preferred model at $\kappa = 15000$ (Figure 4.11b) was chosen because of its location in the inflection corner of the trade-off curve between roughness and misfit (Figure 4.11d), which introduces enough smoothing but without increasing too much misfit. For comparison, examples of under-smooth (Figure 4.11a) and over-smooth (Figure 4.11c) are also provided. We define three types of regions: the fully coupled region with >90% coupling (red), the partially coupled region with ~50% coupling (blue to green), and the freely slipping region with <10% coupling (purple). Because of the reduced resolution toward the boundaries, we here only consider the high resolution area near the coastline as shown by our resolution test (Figure 4.10).

Independent of the smoothing parameter, high spatial heterogeneity along both strike and dip is pronounced among all three cases. Two fully coupled patches, including one offshore centered at ~15 km depth and the other inland centered at ~24 km, are surrounded by freely and partially slipping areas (Figures 4.11a, 4.11b, and 4.11c). This result is different from 50-60% coupling found by previous studies [*Norabuena et al.*, 2004; *LaFemina et al.*, 2009] (Figure 4.12). The overall pattern appears persistent during our interseismic observation period, but it is unknown whether it is persistent over many earthquake cycles, as observed in Kamchatka [*Bürgmann et al.*, 2005], Sumatra [*Chlieh*

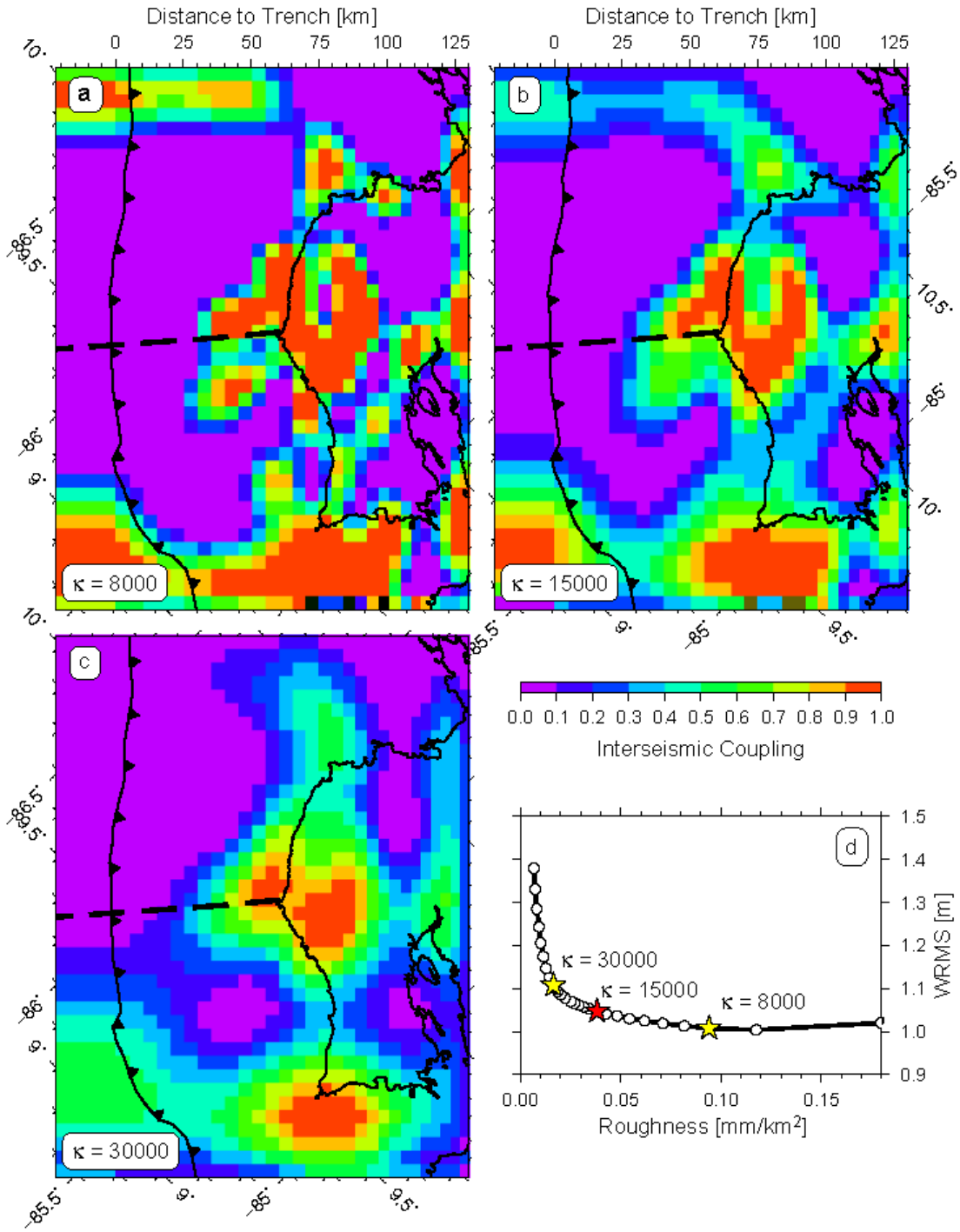

Figure 4.11: Interseismic coupling distribution of the best fit models for selected values of the smoothing parameter κ: (a) κ = 8000, (b) κ = 15,000, and (c) κ = 30,000. As smoothing increases, slip becomes more distributed. (d) Trade-off curve between decreased roughness (increased smoothing) and increased WRMS misfit. Our preferred model at κ = 15,000 is chosen in the inflection corner of the curve.

et al., 2008], and Japan [*Hashimoto et al.*, 2009] from the close correlation of interseismic slip deficit zones with rupture zones of past large earthquakes. In Nicoya, the two fully coupled regions do not appear to resemble either of the 1950 and 1978 rupture regions (Figure 4.1b). But we note that the rupture regions of the two historic events are not very well determined.

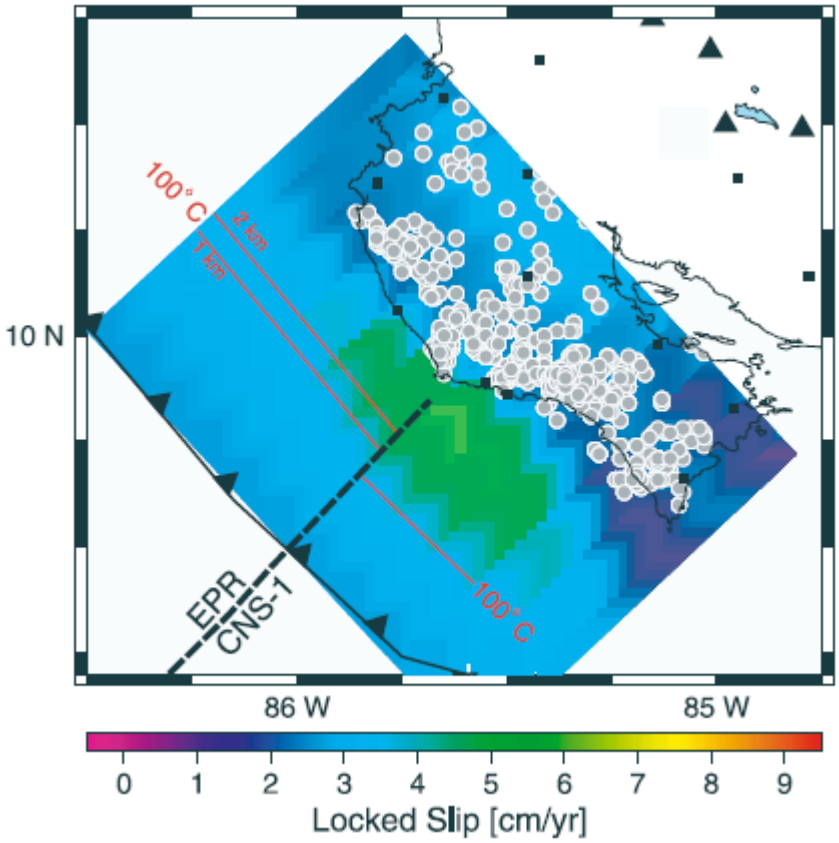

Figure 4.12: Interseismic locked slip distribution of the best fit model by *Norabuena et al.* [2004]. Gray circles are well-located interface earthquakes. Red lines are 100 ℃ isotherms from *Spinelli and Saffer* [2004]. The figure is taken from *Norabuena et al.* [2004].

On the basis of our preferred model (Figure 4.11b), the geodetic moment accumulation rate of the Nicoya segment is calculated to be 8.2×10^{18} N m/yr using a rigidity of 30 GPa. Assuming a constant strain accumulation rate, the Nicoya segment has accumulated enough strain between 1950 and 2010 to generate an M_w 7.7 1950-type

earthquake. A close monitoring of the Nicoya seismic gap is highly recommended considering the high seismic potential of interseismic strong-coupling patches [e.g., *Hashimoto et al.*, 2009; *Moreno et al.*, 2010].

4.6 Discussion

4.6.1 Subduction Interface Along-strike and Along-dip Heterogeneity

The unprecedented detailed imaging of interseismic coupling from 1996 to 2010 on the subduction interface allows us to compare long-term megathrust coupling with short-term phenomena like microearthquakes, tremors, LFEs, and slow-slip events (Figure 4.13).

Most strikingly, the interface seismicity between late-1999 and mid-2001 [*Ghosh et al.*, 2008] is concentrated in the partially coupled region between the two fully coupled regions forming a narrow band. On the EPR side, the correlation between microseismicity and partial coupling is particularly strong, while on the CNS side, some microearthquakes appear in the fully coupled area, which may reflect temporal change in coupling or may be an artifact due to our planar interface geometry. Microearthquakes are almost absent within the shallow full-coupling zone, while slightly more occur within the deep full-coupling zone, but still considerably less than in the partial-coupling zone. The partially coupled microseismic zone may reflect a small decrease in effective normal stress that weakens the plate interface and allows both creep and small earthquakes [*Schwartz and DeShon*, 2007]. *Schwartz and DeShon* [2007] suggested that plate interface microseismicity correlates with the 250 ℃ isotherm line. They proposed that basalt dehydration reactions occurring around 250 ℃ and/or permeability reduction above 250 ℃ may potentially increase pore pressure and reduce effective normal stress

[*Schwartz and DeShon*, 2007]. On the other hand, the location of the microseismicity coincides with the bending of the subducting plate where dip increases rapidly, so we suspect the normal-faulting fractured subducting slab [*von Huene et al.*, 2000; *Ranero et al.*, 2003] may release more fluid at the kink where the slab is flexed as suggested by slab fluid input variations in arc lavas [Patino *et al.*, 2000]. The strongest slab fluid signal was found in western Nicaragua where lower-plate fractures are the most pervasive [Patino *et al.*, 2000]. Overall, our results confirm that interseismic microseismicity neither defines the strong-coupling patches nor marks the updip or downdip limit of the seismogenic zone in Nicoya [*Norabuena et al.*, 2004; *DeShon et al.*, 2006; *Schwartz and DeShon*, 2007].

Along strike, a 5-km upward and trenchward shift in the updip limit of interface seismicity has been identified to occur at the transition from EPR to CNS [*Newman et al.*, 2002; *DeShon et al.*, 2006], which was associated with the thermal difference between the anomalously cold EPR crust due to hydrothermal circulation and the normal CNS crust cooled only by conduction [*Fisher et al.*, 2003]. Interestingly, we identify a similar upward and trenchward along-strike change of the fully coupled region crossing the CNS-EPR boundary as mimicked by the offset of the 100 ℃ and 250 ℃ isotherm lines (Figure 4.13b).

The updip limit of the seismogenic zone defined by the updip of the shallow locked patch is located at ~8 km depth and ~25 km landward from MAT, the same as previously suggested by *Norabuena et al.* [2004], and coincides with the 100 ℃ opal dewatering isotherm derived from thermal models [*Spinelli and Saffer*, 2004] (Figures 4.11b and 4.12). The correspondence of the 100-150 ℃ isotherm to the updip limit of the

seismogenic zone has been shown in many other subduction zones including south Alaska, Cascadia, Chile, and SW Japan [e.g., *Oleskevich et al.*, 1999]. In this temperature range, water contained in sediments that enter subduction zones is released by diagenetic and low-grade metamorphic processes (e.g., opal to quartz and smectite to illite) and expelled by compaction and consolidation [*Moore and Saffer*, 2001]. *Spinelli and Saffer* [2004] proposed that the dewatering processes decrease fluid pressure, increase effective normal stress and thus may control the transition from aseismic stable sliding to coseismic stick-slip at shallow depths of the Nicoya subduction zone.

The downdip of the full coupled patch from our preferred model is located at 28-29 km depth (Figures 4.13a and 4.13b). A very narrow partially coupled transition region appears to exist between the deep full coupled region and the continental Moho. The downdip limit of the seismogenic zone has been suggested to be controlled by either the 350 ℃ isotherm or the serpentinized mantle wedge depending on which the subducting plate encounters first [*Hyndman et al.*, 1997]. Beneath Nicoya, the oceanic slab intersects the continental Moho at 30-35 km depth (Figures 4.13a and 4.13b) with the mantle wedge 15-25% serpentinized [*DeShon and Schwartz*, 2004; *DeShon et al.*, 2006]; however, the intersection of the 350 ℃ isotherm with the subduction interface varies around the continental Moho according to different thermal models, which makes it difficult to determine the controlling factor for the downdip limit [*DeShon et al.*, 2006]. Nevertheless, *Harris and Wang* [2002] suggested the intersection of 350 ℃ isotherm with the subducting plate is well below the mantle wedge and the transition from stick-slip to stable sliding at depth is not thermally controlled, but related to the serpentinized mantle wedge.

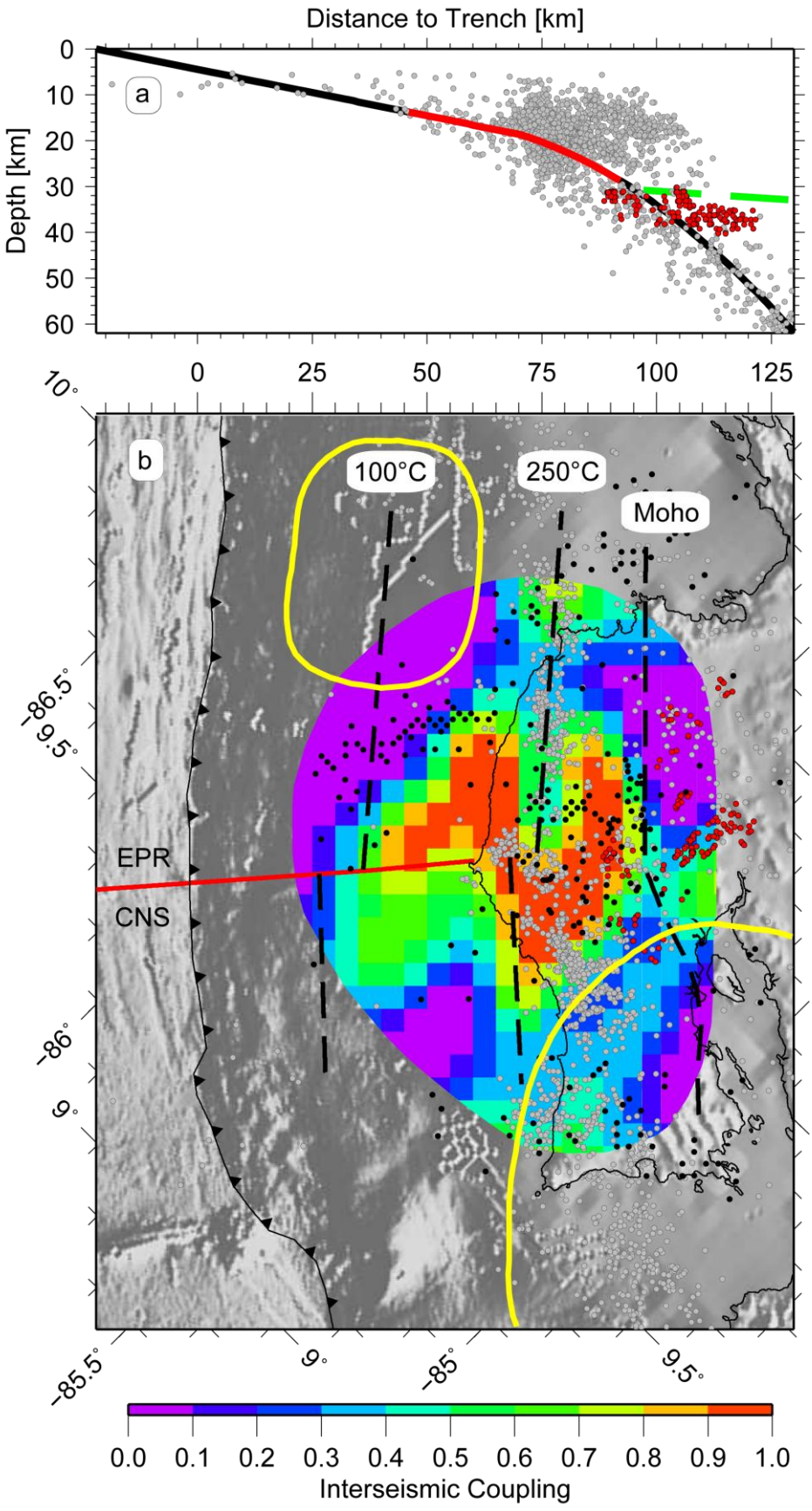
Distance to Trench [km]
Depth [km]
a
0
10
20
30
40
50
60
0
25
50
75
100
125
b
100°C
250°C
Moho
EPR
CNS
10°
-86.5°
-9.5°
-86°
-9°
-85.5°
-9°
-85°
-9.5°
0.0
0.1
0.2
0.3
0.4
0.5
0.6
0.7
0.8
0.9
1.0
Interseismic Coupling

Figure 4.13: Comparison of our preferred model at κ = 15,000 with interplate microearthquakes, LFEs, tremors, slow-slips and isotherms. (a) Cross section of the subduction plate interface with the fully locked (>90%) portion in red. Green dashed line is the continental Moho inferred from the tomography study by *DeShon et al.* [2006]. Gray circles are interface seismicity between late-1999 and mid-2001 taken from *Ghosh et al.* [2008]. Red circles are LFEs located by *Brown et al.* [2009]. (b) Surface projection of the interseismic coupling distribution of our preferred model. Only high resolution part determined by the checkerboard test is plotted. Red line is the rough-smooth CNS-EPR boundary and its landward projection [*Barckhausen et al.*, 2001]. Thick dashed lines are 100 ℃ isotherm, 250 ℃ isotherm, and the continental Moho, respectively [*Spinelli and Saffer*, 2004; *DeShon et al.*, 2006; *Schwartz and DeShon*, 2007]. Note the isotherms could shift either landward or seaward depending on models, but the CNS-EPR offset persist. Yellow curves outline one updip and one downdip slip patches of the 2007 slow-slip event determined by *Outerbridge et al.* [2010]. Black dots are tremors from *Outerbridge et al.* [2010] and *Walter et al.* [2011]. Gray and red circles are the same as described in Figure 4.13a.

Tremor characterized with a non-distinct small-amplitude high-frequency onset followed by a harmonic waveform in the typical long period range of 0.2-2 s (frequency range of 0.5-5 Hz) was originally only found in active volcanic regions [*Chouet*, 1996]. Until a decade ago, non-volcanic tremor (NVT) was first discovered in the Nankai subduction zone in SW Japan [*Obara*, 2002] and subsequently observed in other subduction zones from Cascadia [*Rogers and Dragert*, 2003], Costa Rica [*Brown et al.*, 2005], Mexico [*Payero et al.*, 2008] to Alaska [*Peterson and Christensen*, 2009].

The NVT waveforms recorded in SW Japan, northern Cascadia, and northern Costa Rica contain identifiable sequences of low-frequency (~1-5 Hz) earthquakes (LFEs) [*Shelly et al.*, 2007; *Brown et al.*, 2008, 2009; *La Rocca et al.*, 2009, 2010] and very-low-frequency (0.02-0.05 Hz) earthquakes (VLFs) [*Ito et al.*, 2007, 2009], which suggests that NVT is likely a superposition of bursts of LFEs and/or VLFs.

In SW Japan, NVT and LFEs were inferred to be fluid-enabled weak shear slip near the deep interface seismic-aseismic transition zone from precise relocations of LFEs

[*Shelly et al.*, 2006; *Brown et al.*, 2009] and focal mechanisms of LFEs [*Ide et al.*, 2007] and VLFs [*Ito et al.*, 2007, 2009]. In Cascadia, the mechanism is less clear and highly debated. NVT was found distributed over a very wide depth range (>40 km wide) using direct P and/or S wave arrivals [*Kao et al.*, 2005; La Rocca *et al.*, 2008] or envelope cross correlation [*McCausland et al.*, 2005], while a new location method including S minus P time differences from cross correlating horizontal and vertical components imposed a better constraint on depth and placed NVT near the plate interface [*La Rocca et al.*, 2009, 2010] or well-defined structures with strong seismic reflection [*Kao et al.*, 2009].

In contrast to Nankai and Cascadia where NVT and LFEs cluster near the deep transition zone, *Walter et al.* [2011] suggested NVT in Nicoya is distributed throughout the seismogenic zone including shallow depths. The locations of their determination bound one side of the shallow fully coupled region between 100 ℃ and 250 ℃ isotherms showing good correlation with the freely slipping region, while the deep tremors between the 250 ℃ isotherm and continental Moho are more widespread (Figure 4.13b).

LFEs in Nicoya detected by a network autocorrelation method are clustered at 30-40 km depth [*Brown et al.*, 2009], similar to other subduction zones, with some occurring in the partially coupled transition zone and most others near the tip of the mantle wedge below Moho (Figures 4.13a and 4.13b). The locations of LFEs in Nicoya approximately correspond to 350 ℃ isotherm, while temperatures for LFEs in SW Japan and Cascadia vary from 325 ℃ to 575 ℃ [*Peacock*, 2009]. The wide range of temperatures for LFEs excludes any dependence on a particular temperature or metamorphic reaction, but indicates the importance of fluid [*Peacock*, 2009].

Seismically detected NVT is observed to co-occur both temporally and spatially with geodetically detected transient slow-slip event (SSE) in SW Japan [e.g., *Obara et al.*, 2004] and Cascadia [e.g., *Rogers and Dragert*, 2003], thus it has been speculated that NVT, LFEs, VLFs, and SSE are essentially different manifestations of a single process – quasi-static slip [e.g., *Shelly et al.*, 2006; *Wech and Creager*, 2007; *La Rocca et al.*, 2009, 2010; *Peng and Gomberg*, 2010]. However, NVT and long-term SSE observed in the Mexican subduction zone are separated spatially and not completely synchronized in time suggesting different origins for NVT and SSE in Mexico [*Kostoglodov et al.*, 2010]. *Kostoglodov et al.* [2010] proposed that SSE is a creep-like slip without producing seismic radiation while the stress change induced by the propagation of SSE may trigger NVT at favorable locations.

In Nicoya, *Outerbridge et al.* [2010] studied the 2007 slow-slip event and found two distinct slip patches: one shallow patch centered at ~6 km depth and one deep patch centered at 25-30 km depth (Figure 4.13b). The locations of the two patches are both outside our high resolution area, but certainly not overlapping the fully coupled regions. NVT were found temporally correlated with the 2007 event but not spatially [*Outerbridge et al.*, 2010].

4.6.2 Trailing Edge of the Central America Forearc

Where the Central America forearc sliver takes off, namely the trailing edge, is still unclear. *Lewis et al.* [2008] placed the trailing edge in the CCRDB and suggested the Atirro-R ó Sucio fault system to be the northern margin of the forearc sliver (Figure 4.14a). The CCRDB (outlined by yellow dashed lines in Figure 4.14a) is a diffuse zone of seismically active faulting across central Costa Rica [*Marshall et al.*, 2000]. It marks the

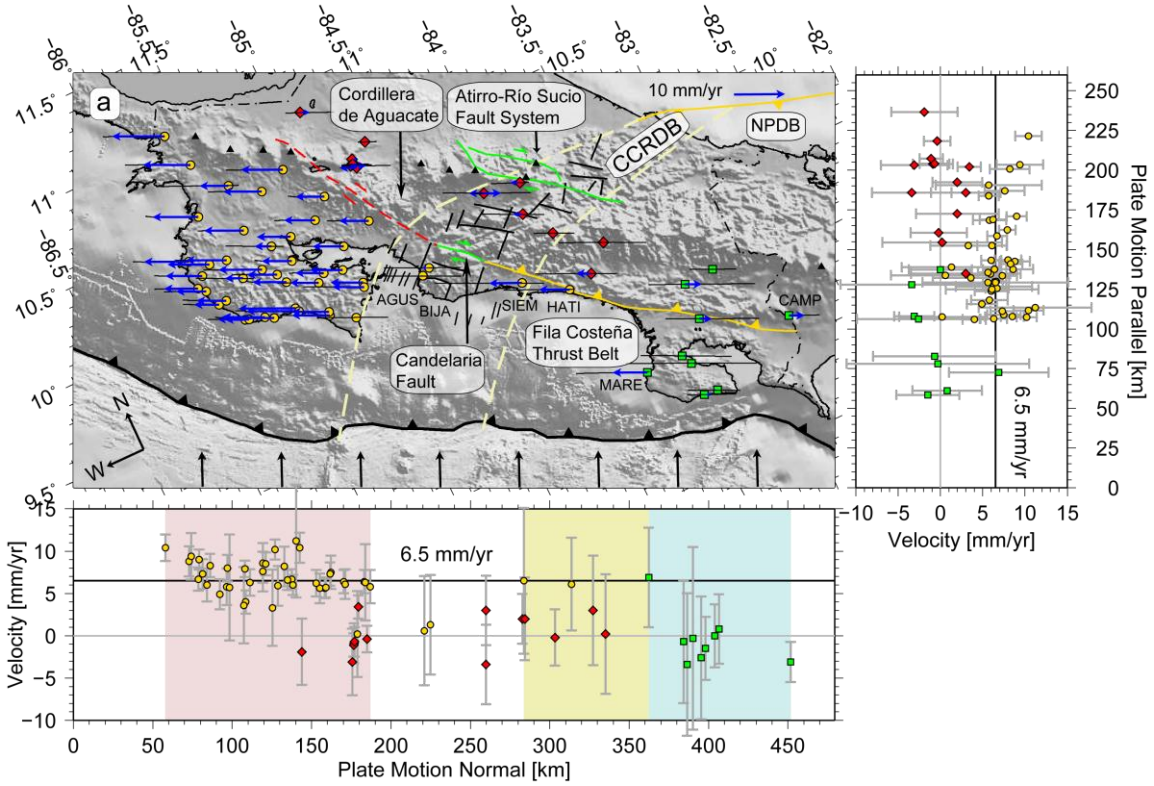
a
Cordillera de Aguacate
Atirro-Río Sucio Fault System
CCRDB
NPDB
10 mm/yr
AGUS
BIJA
SIEM
HATI
CAMP
MARE
Fila Costeña Thrust Belt
Candelaria Fault
N
W
6.5 mm/yr
Velocity [mm/yr]
Plate Motion Parallel [km]
Plate Motion Normal [km]

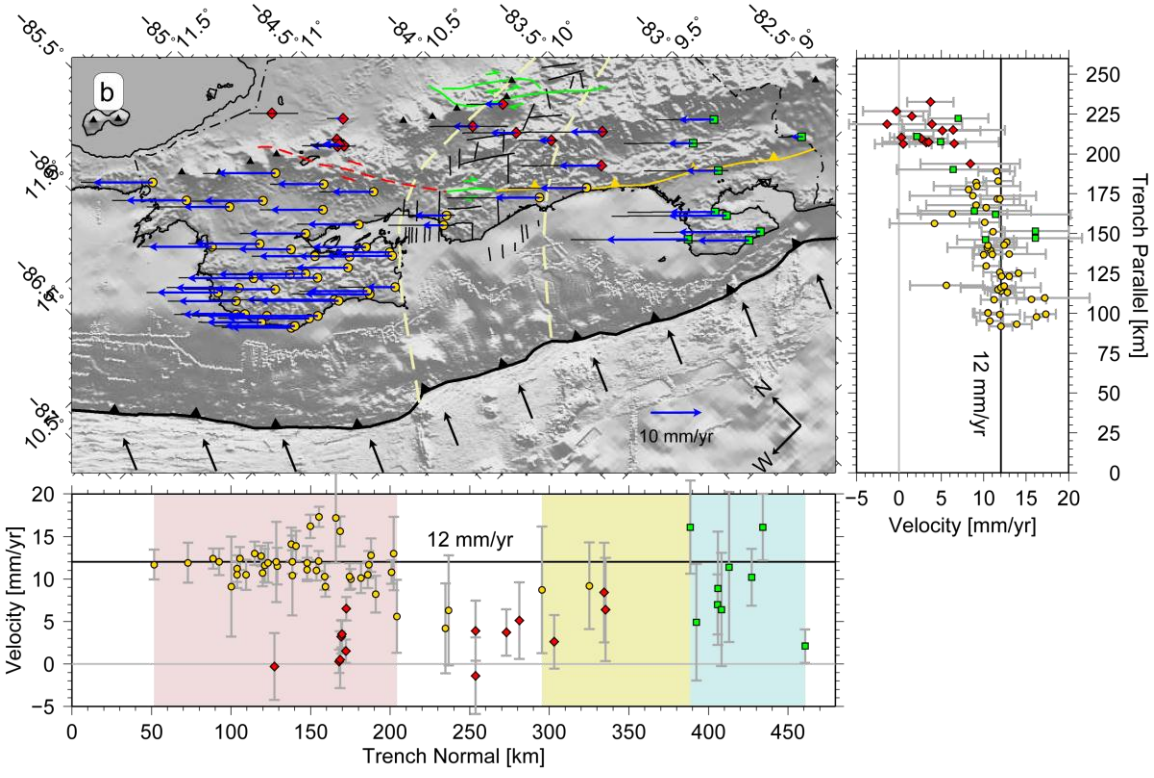
b
10 mm/yr
N
W
12 mm/yr
Velocity [mm/yr]
Trench Parallel [km]
Trench Normal [km]

Figure 4.14: Map of the trailing edge of the Central America forearc. Caribbean-fixed interseismic velocities (blue vectors) are from this study for NW Costa Rica and from *LaFemina et al.* [2009] for central and SE Costa Rica. Velocities are projected to (a) plate convergence parallel (N65°W), and (b) trench parallel (N45°W). Yellow circles, the forearc sites; Red diamonds, the non-forearc sites; Green squares, the Cocos Ridge sites. Yellow dashed lines outlines the Central Costa Rica Deformed Belt (CCRDB) modified from *Marshall et al.* [2000]. Black lines represent NW and NE striking mesoscale faults in the CCRDB and yellow lines represent thrusts [*Marshall et al.*, 2000]. Candelaria fault is taken from *Marshall et al.* [2000], while the Atirro-Río Sucio fault system is taken from *Lewis et al.* [2008]. Red dashed line is the strike-slip fault we propose in this paper. Black arrows show plate convergence motion (mm/yr) derived from the PVEL model by *DeMets et al.* [2010]. Black triangles are volcanoes with evidence of Holocene activity [*Siebert and Simkin*, 2002]. NPDB, North Panama Deformed Belt.

western margin of the Panama block and links the North Panama Deformed Belt (NPDB) on the Caribbean side with the MAT on the Pacific side [*Marshall et al.*, 2000]. A detailed examination of the GPS interseismic velocity field showed that the margin-parallel component is absent in southern Cost Rica but significant in northern Costa Rica [*LaFemina et al.*, 2009] (Figure 4.14a).

We combine the velocities from this study and *LaFemina et al.* [2009], then project them along N65°W that is normal to the plate convergence and also generally consistent with the trench strike offshore central Costa Rica (Figure 4.14a). According to the different behaviors and locations of the GPS sites, we divide all the sites into the Osa (green squares), forearc (yellow circles), and non-forearc (red diamonds) groups (Figure 4.14a). All the Osa sites except MARE and CAMP move parallel to the plate convergence without noticeable margin-parallel motion. MARE exhibits ~6.5 mm/yr northwestward trench-parallel motion, and CAMP shows ~3 mm/yr southeastward trench-parallel motion. The anomalous deviations of MARE and CAMP indicate that the translation of the forearc blocks may have already started at the two sites. However, a definite conclusion cannot be drawn based only on two vectors and its large errors. But

more evidence can be found further northwest where SIEM and HATI move along the trench at the same velocity as MARE. So it is likely that the translation has started at least between SIEM and MARE (green shaded area in Figure 4.14a) if not even more southeast. AGUS and BIJA show anomalously lower trench-parallel motion than sites either northwest or southeast. We suspect that they may be interfered by the propagation of the CCRDB into the forearc region. We also note that the short occupation of these two sites may introduce large errors (Table 4.1), so the low velocities may not be real. Although sites south of Nicoya show better consistency in the N45°W projection direction (Figure 4.14a), the uniform translation of sites in Nicoya is better shown in the direction of N45°W (Figure 4.14b). A direction change of the forearc sliver motion in accord with the change in trench strike might explain this. Non-forearc sites generally show almost zero trench-parallel motion considering errors (Figure 4.14a).

A clear spatial separation exists between the forearc and non-forearc sites. We propose that the northern boundary of the Costa Rican forearc block is composed of a hypothesized right-lateral strike-slip fault (red dashed line in Figure 4.14a) that goes through the Cordillera de Aguacate, the Candelaria fault [*Marshall et al.*, 2000], and the Longitudinal fault that defines the thrust front of the Fila Costeña thrust belt [*Fisher et al.*, 2004]. The Cordillera de Aguacate is eroded remnants of an extinct Neogene volcanic arc [*Marshall et al.*, 2000] whose volcanism was shut down after the inception of the Cocos Ridge subduction ~2-3 Ma [*MacMillan et al.*, 2004] due to shallowing of the slab and possible slab retreat by forearc erosion [*Marshall et al.*, 2000]. It is likely that the translation of the forearc sliver existed before the Cocos Ridge subduction when the volcanism in Cordillera de Aguacate was still active, thus the strike-slip fault cut through

the weak and hot Aguacate instead of the modern Cordillera Central. The Longitudinal fault is dominated by thrusting at present [*Fisher et al.*, 2004], but it may be the continuation of the Aguacate-Candelaria strike-slip fault before the Cocos Ridge subduction and reactivated as a thrust fault in response to the ridge indentation. The recently mapped Atirro-Río Sucio fault system includes a major releasing step-over forming a pull-apart basin [*Lewis et al.*, 2008], which most likely result from the recent migration of volcanism to its current location suggesting that a reconfiguration of the forearc boundary might be undertaken.

4.6.3 Driving Mechanism for Forearc Sliver

The partial partitioning of the CO-CA plate convergence and the possible existence of a forearc sliver before the Cocos Ridge subduction strongly support oblique convergence with strong coupling as the major driving mechanism for the NW Costa Rican forearc sliver. However, the puzzle exists in El Salvador where westward forearc motion continues at the absence of oblique convergence (Figure 4.2) [*Alvarado et al.*, 2011]. *Alvarado et al.* [2011] argued that the weak frictional coupling offshore much of the Central America facilitates the free slipping of the Salvadoran forearc along with the Nicaraguan forearc as a single undeforming block while the northwestward lateral escape from the Cocos Ridge subduction provides the pushing force [*LaFemina et al.*, 2009].

Many authors concluded weak coupling on the subducting interface from the lack of interseismic signals on coastal GPS sites in Guatemala, Al Salvador and Nicaragua [e.g., *Lyon-Caen et al.*, 2006; *Correa-Mora et al.*, 2009; *Alvarado et al.*, 2011]. The sites they used are mostly >120 km away from the trench. According to our observation near Nicoya (Figures 4.5c and 4.5d), 120 km is far beyond the region where a clear

interseismic coupling signal can be identified, and thus those coastal sites provide no information about the interplate coupling. In addition, gCMT solutions show thrusting earthquakes occur on a regular basis along the subduction zone from Guatemala to Nicaragua (Figure 4.2), so it is unlikely the coupling is as low as zero as suggested by models to allow free slipping [*Correa-Mora et al.*, 2009; *Alvarado et al.*, 2011].

Instead we propose another strong coupling model to explain the paradox of El Salvador. We suggest that the bottom of the forearc is moving together with the Cocos plate in the plate convergence direction until thrusting earthquakes occur to release the accumulated strain. Where oblique subduction exists, the forearc sliver translation starts taking trench-parallel motion if oblique shear stress overcomes the resistance stress. The amount of trench-parallel motion a forearc sliver takes is determined by obliquity and coupling long the volcanic arc. Higher obliquity leads to larger shear force and may cause faster translation rate. The obliquity in Nicaragua is larger than in Costa Rica [*DeMets*, 2002], thus it may explain why the Nicaraguan forearc translates a little faster than the Costa Rican forearc. However, coupling along the volcanic arc is also important. If the coupling is low, the forearc can translate freely and may cause complete partitioning. In other words, the forearc translation takes all the trench-parallel motion. In contrast, strong coupling have been suggested along the volcanic arc faults in Central America [*Álvarez-Gómez et al.*, 2008; *Correa-Mora et al.*, 2009; *Alvarado et al.*, 2011]. The volcanic arc faults are locked from surface to the locking depth of 2-6 km, so the upper portion of the forearc crust cannot move simultaneously with the subducting plate as the bottom of the forearc does during interseismic periods. Instead the upper portion of the forearc is dragged by the motion of the lower portion. As a result, the forearc only takes a small

portion of the trench-parallel motion and leaves a large component to be taken by thrusting. In El Salvador, although the orthogonal subduction supplies no shear force for forearc translation at the bottom of the forearc, the upper layer of the forearc is still likely pushed by the Nicaraguan forearc and thus translates at the same rate as the Nicaraguan forearc as suggested by *Alvarado et al.* [2011].

4.7 Conclusion

Using the campaign and continuous GPS data from 1996 to 2010, we reveal the partial partitioning of the CO-CA plate convergence into 12 ± 1 mm/yr trench-parallel forearc sliver motion and less oblique thrusting with 20 mm/yr strike-slip motion on the subduction interface. Such a partition contributes the first-order deformation of NW Costa Rica. Coupling across the subduction interface and on the volcanic arc faults contribute the second-order deformation.

Surface deformation caused by interseismic coupling on the subduction interface is primarily trench-normal. Two fully-coupled patches, one located offshore the Nicoya Peninsula centered at ~15 km and the other located inland centered at ~24 km, are identified with the potential to generate an M_w 7.7 1950-type earthquake. The updip of the seismogenic zone is located at ~8 km depth coinciding with the 100 ℃ isotherm. The downdip of the seismogenic zone is located updip of the continental Moho and likely controlled by the mantle wedge. Interseismic interface microearthquakes are mostly concentrated between the two fully coupled patches.

Surface deformation caused by forearc sliver translation is primarily trench-parallel. The volcanic arc faults have a locking depth of 2-6 km. The trailing edge of the Central America forearc is likely situated in central Costa Rica. The hypothesized right-

lateral strike-slip fault, Candelaria fault and the Longitudinal fault may be the northern boundary of the Costa Rican forearc. Strong coupling and oblique subduction are more likely the mechanism for forearc sliver motion.

APPENDIX A

ERROR ANALYSIS FOR GPS SITES IN AND NEAR LVC

Table A.1: Estimated amplitudes for white a_w, flicker a_{fl}, and random walk a_{rw} noise for the regionally filtered data of 17 GPS sites in and near Long Valley Caldera (LVC) between 2000 and 2008 [J. Langbein, personal communication, 2009]. Amplitude solutions are determined following the Maximum Likelihood Estimator (MLE) methodology described in *Langbein* [2004].

	North			East			Up		
Site	a_w mm/yr	a_{fl} mm/yr$^{0.25}$	a_{rw} mm/yr$^{0.5}$	a_w mm/yr	a_{fl} mm/yr$^{0.25}$	a_{rw} mm/yr$^{0.5}$	a_w mm/yr	a_{fl} mm/yr$^{0.25}$	a_{rw} mm/yr$^{0.5}$
BALD	1.10	1.89	1.82	1.03	2.11	0.50	3.75	7.78	1.50
CA99	1.50	2.53	2.08	1.25	1.91	1.50	4.01	10.8	11.60
CASA	1.50	2.53	2.10	1.22	2.14	1.00	4.04	10.79	11.90
DDMN	1.06	1.71	1.50	1.38	1.05	1.50	4.06	0.31	11.49
HOTK	1.38	2.41	1.50	1.08	0.01	1.59	3.92	5.56	1.50
JNPR	1.74	5.39	1.00	1.72	4.26	1.50	4.68	19.54	1.50
KNOL	1.06	3.17	1.50	1.19	2.58	1.50	3.63	10.11	3.76
KRAC	1.18	0.80	1.75	1.23	0.78	1.50	4.28	7.83	6.03
KRAK	1.16	1.70	1.70	1.28	1.45	1.50	4.31	9.10	5.90
LINC	1.43	2.44	1.50	1.33	4.26	1.50	3.41	15.28	9.65
MINS	0.47	5.42	1.00	1.01	3.22	5.99	2.33	16.65	1.50
MWTP	1.41	3.61	2.73	1.44	4.04	1.50	3.77	22.45	10.16
PMTN	1.13	0.03	1.50	1.44	0.87	1.50	4.05	6.85	1.50
RDOM	1.09	1.81	0.50	1.04	0.01	1.50	3.56	5.83	6.84
SAWC	1.12	1.10	0.50	1.16	1.30	1.50	4.32	4.99	3.92
TILC	1.78	3.48	2.46	1.30	1.23	2.45	4.92	6.55	1.94
WATC	0.96	2.05	0.50	0.92	0.84	1.00	3.58	9.47	1.50

APPENDIX B

GPS TIME SERIES RELATIVE TO STABLE CARIBBEAN

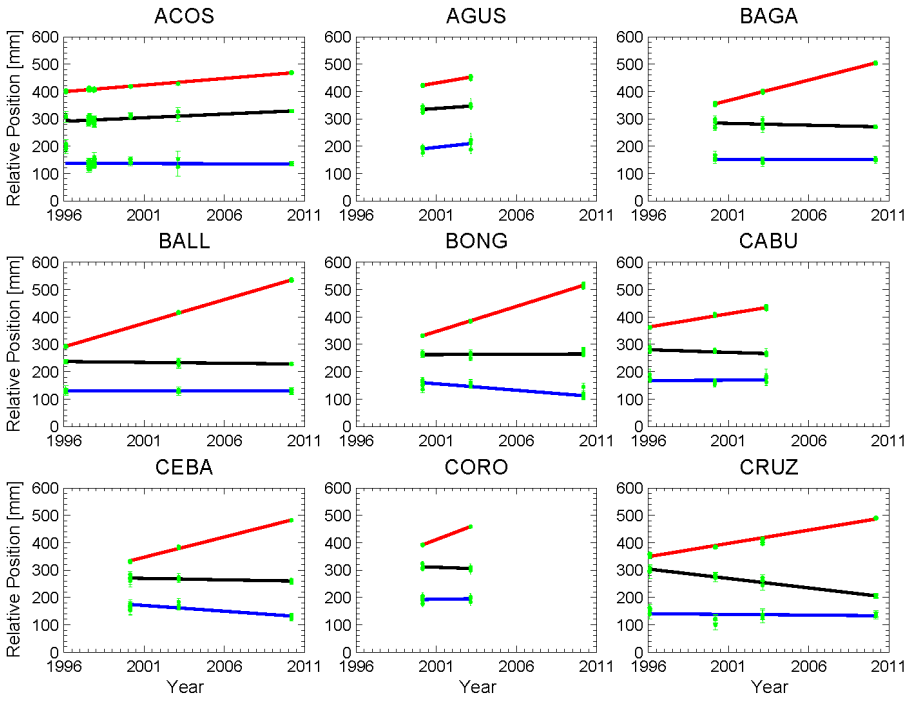

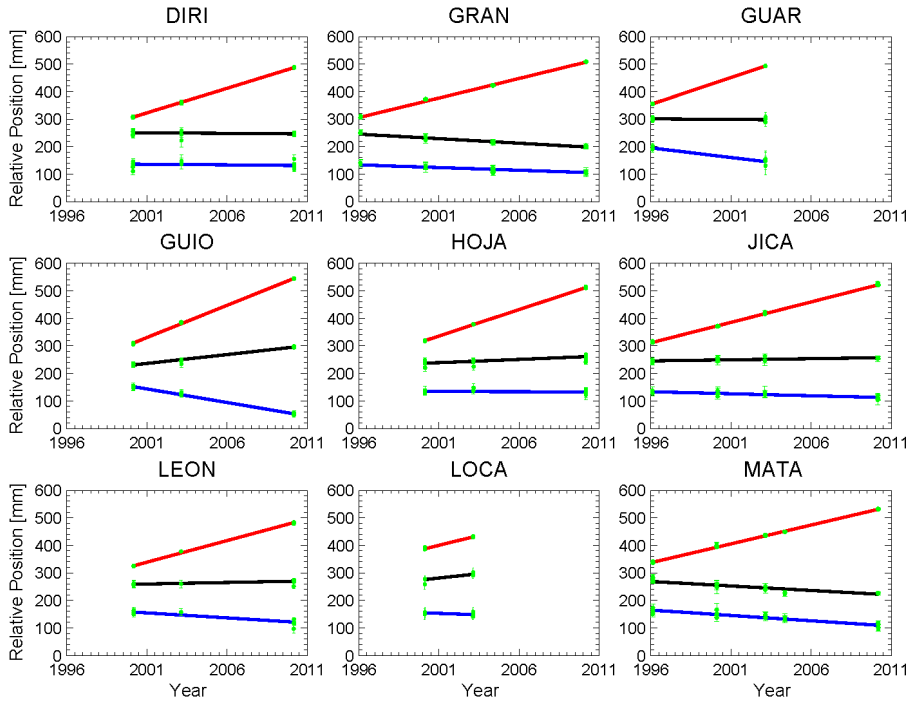

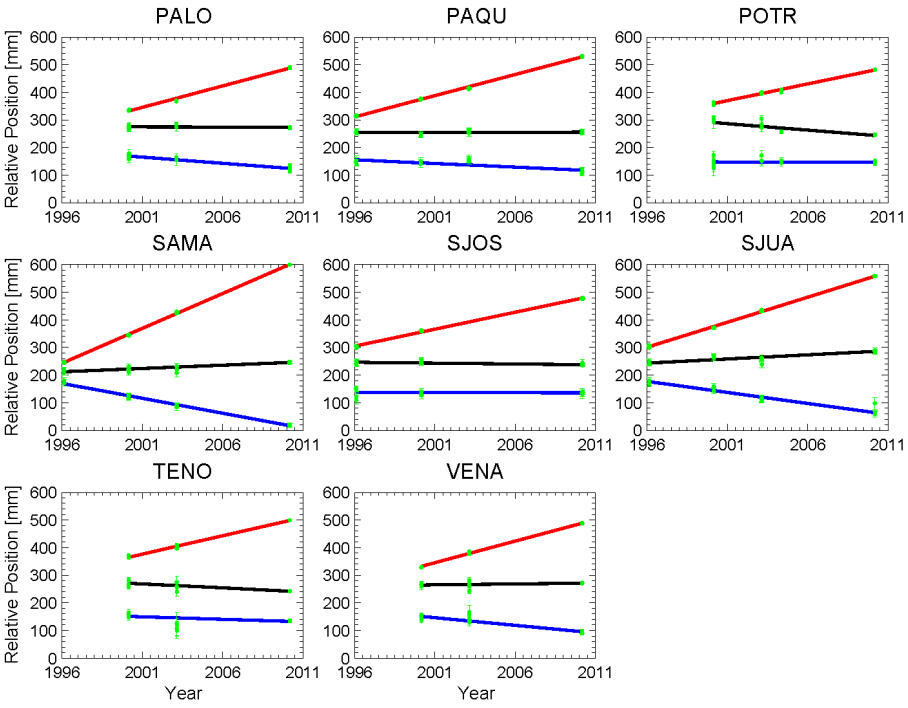

Figure B.1: GPS Time series relative to the stable Caribbean plate for campaign sites in Nicoya.

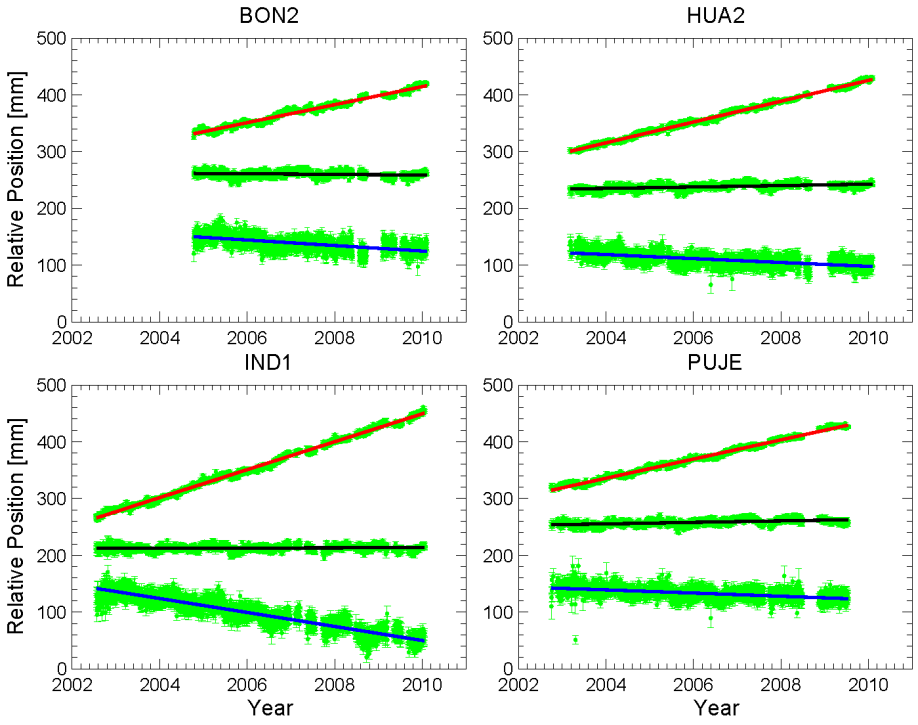

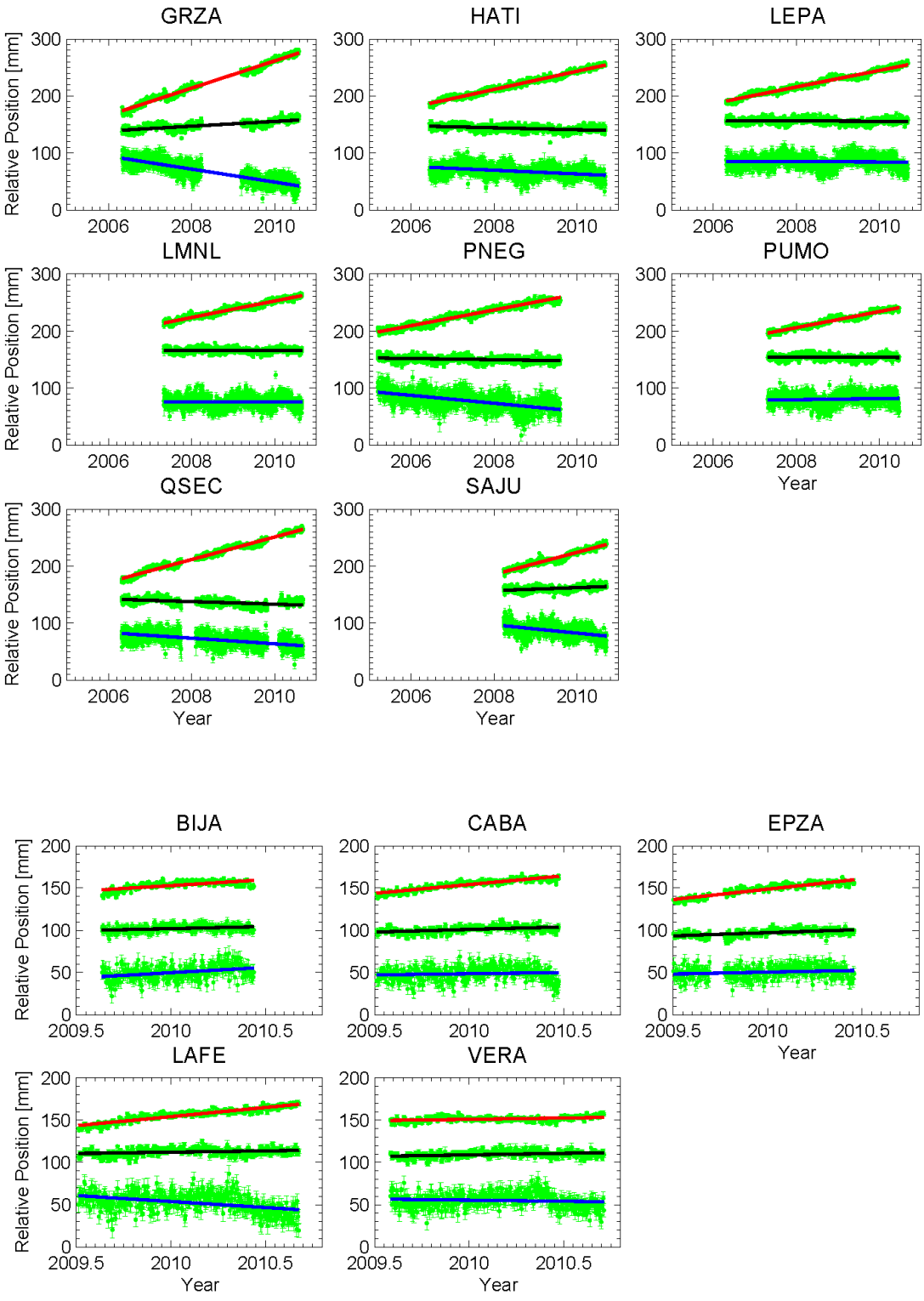

Figure B.2: GPS Time series relative to the stable Caribbean plate for continuous sites in Nicoya.

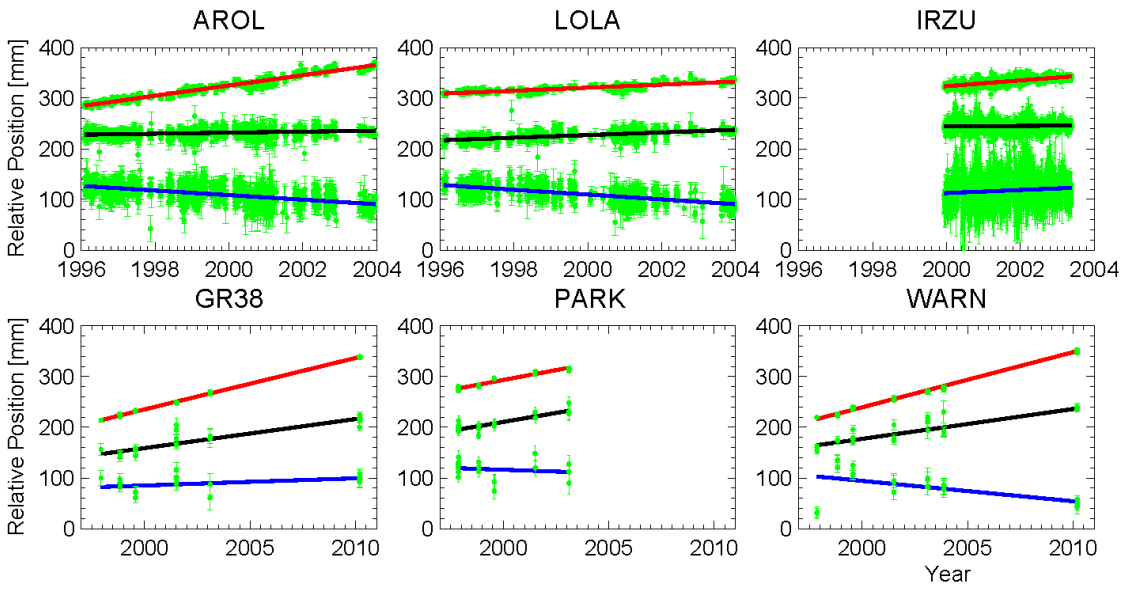

Figure B.3: GPS Time series relative to the stable Caribbean plate for volcano sites.

APPENDIX C

STRESS MINIMIZATION VS ROUGHNESS MINIMIZATION

Distributed slip models usually have the number of parameters larger than the number of data points. One approach to solve the underdetermined problems is applying a smoothing operator. The most widely used smoothing operator is Laplacian smoothing [*Harris and Segall,* 1987]. Laplacian smoothing algorithm minimizes second-order derivative of interface displacement field $\nabla^2 S$. Roughness, the average second-order finite-difference sum of each patch [*Jónsson et al.*, 2002], is used to represent the degree of Laplacian smoothing describing deviations from zero, thus we call this method roughness minimization. However, low roughness allows continued and smooth increases in displacement; it does not constrain the strain field. Unrealistically large slip would occur in areas of low resolution like places close to trenches without direct geodetic observations.

We explored a new algorithm that minimizes first-order derivative of interface displacement $\frac{\partial}{\partial x} S_{ij}$, which is actually strain. Strain can be related to stress σ by $\sigma_{kl} = c_{ijkl} \frac{\partial}{\partial x} S_{ij}$, thus we call this new method stress minimization. Stress minimization is more realistic for fault interface where perturbations would cause additional slip.

We did a comparison test using both methods for the 1 April 2007 M_w 8.1 Solomon Islands Earthquakes. The model details were discussed in *Chen et al.* [2009]. We fixed the fault dip at 29°, used 100 m for the maximum slip and set free surface at trench. The results are noticeably different. The inverted maximum slip is up to 50 m

using roughness minimization (Figure C.1), while the maximum slip is well constrained to ~30 m using stress minimization (Figure C.2).

We also tested the two methods for interseismic coupling of Costa Rica, but the results are not very different. Presumably it is because the data coverage is much better in Costa Rica than in Solomon. So we conclude that roughness minimization and stress minimization are indistinguishable in places with good data coverage, but stress minimizations constrain the maximum slip better in places with limited data coverage.

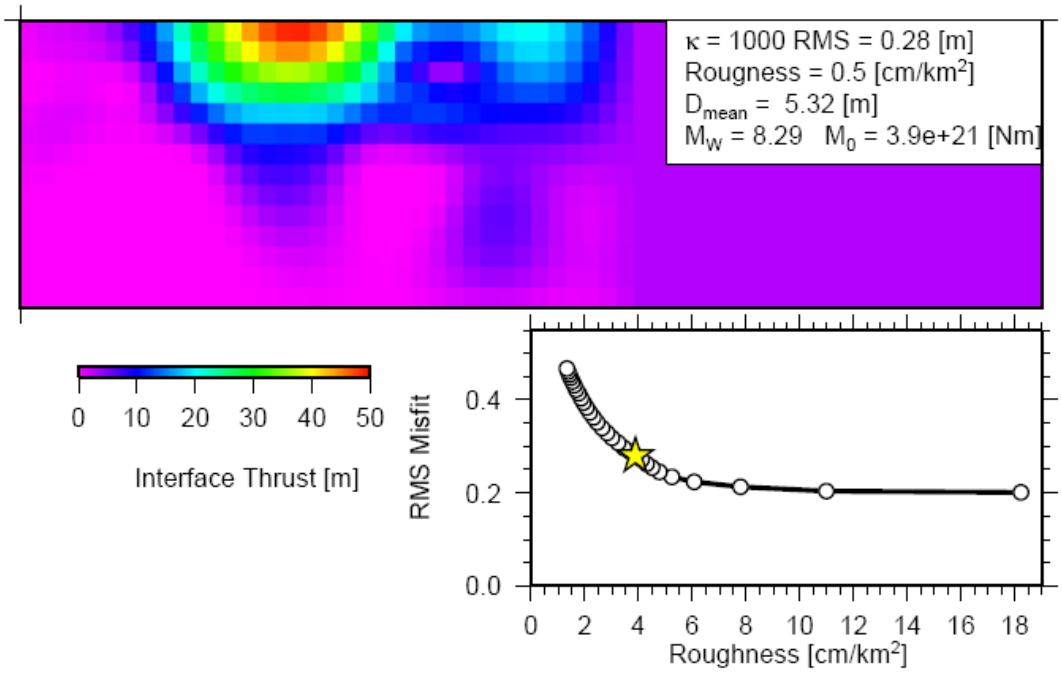

Figure C.1: Best-fit model for roughness minimization.

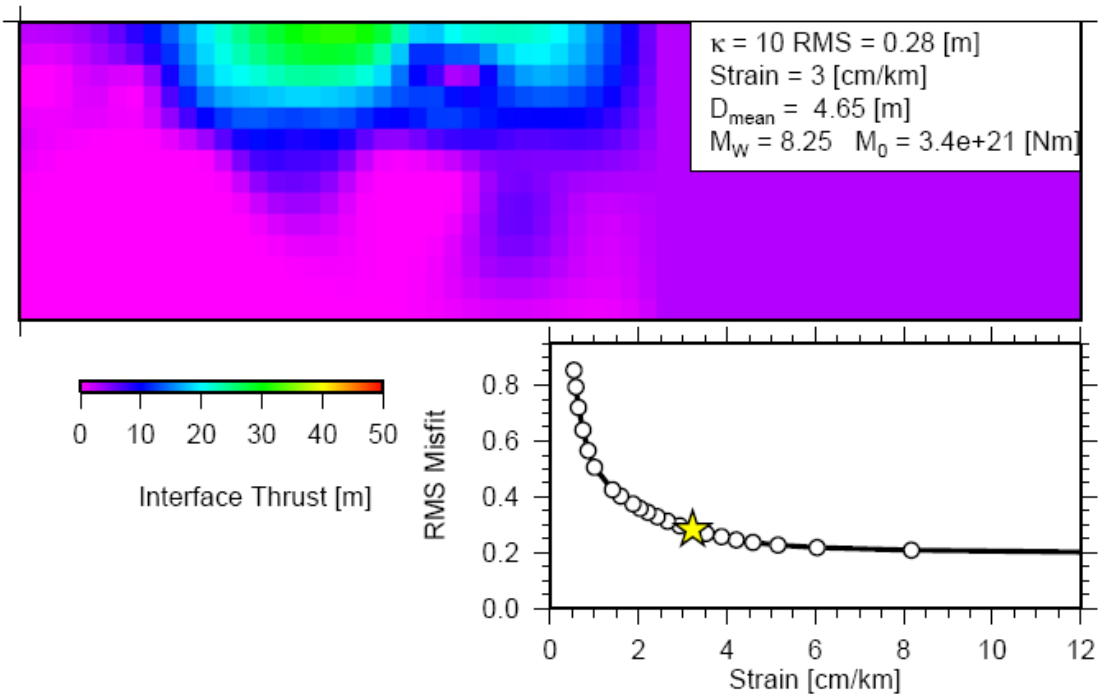

Figure C.2: Best-fit model for stress minimization.

REFERENCES

Adamek, S., F. Tajima, and D. Wiens (1987), Seismic rupture associated with subduction of the Cocos ridge, *Tectonics*, *6*(6), 757-774, doi:10.1029/TC006i006p00757.

Agostini, S., G. Corti, C. Doglioni, E. Carminati, F. Innocenti, S. Tonarini, P. Manetti, G. Di Vincenzo, and D. Montanari (2006), Tectonic and magmatic evolution of the active volcanic front in El Salvador: Insight into the Berlin and Ahuachapan geothermal areas, *Geothermics*, *35*(4), 368-408, doi:10.1016/j.geothermics.2006.05.003.

Ambraseys, N. N., and J. A. Jackson (1997), Seismicity and strain in the Gulf of Corinth (Greece) since 1694, *J. Earthquake Eng.*, *1*(3), 433-474, doi: 10.1080/13632469708962374.

Allmann, B. P., and P. M. Shearer, (2009), Global variations of stress drop for moderate to large earthquakes, *J. Geophys. Res.*, *114*, B01310, doi:10.1029/2008JB005821.

Altamimi, Z., X. Collilieux, J. Legrand, B. Garayt, and C. Boucher (2007), ITRF2005: A new release of the International Terrestrial Reference Frame based on time series of station positions and Earth Orientation Parameters, *J. Geophys. Res.*, *112*, B09401, doi:10.1029/2007JB004949.

Alvarado, D., C. DeMets, B. Tikoff, D. Hernandez, T. F. Wawrzyniec, C. Pullinger, G. Mattioli, H. L. Turner, M. Rodriguez, and F. Correa-Mora (2011), Forearc motion and deformation between El Salvador and Nicaragua: GPS, seismic, structural, and paleomagnetic observations, *Lithosphere*, *3*(1), 3-21, doi:10.1130/L108.1.

Álvarez-Gómez, J. A., P. T. Meijer, J. J. Martínez-Díaz, and R. Capote (2008), Constraints from finite element modeling on the active tectonics of northern Central America and the Middle America Trench, *Tectonics*, *27*, TC1008, doi:10.1029/2007TC002162.

Avants, M., S. Schwartz, A. Newman, and H. DeShon (2001), Large underthrusting earthquakes beneath the Nicoya Peninsula, *Eos Trans. AGU*, *82*(46), Fall Meet. Suppl., Abstract T52E-07.

Avallone, A., et al. (2004), Analysis of eleven years of deformation measured by GPS in the Corinth Rift Laboratory area, *Compt. Rendus Geosci.*, *336*, 301-311, doi: 10.1016/j.crte.2004.12.007.

Bailey, R. A. (1989), Geologic map of Long Valley caldera, Mono-Inyo craters volcanic chain, and vicinity, eastern California, *U.S. Geol. Surv. Misc. Invest. Map*, I-1933, scale 1:62,500; pamphlet.

Bailey, R. A., G. B. Dalrymple, and M. A. Lanphere (1976), Volcanism, structure, and geochronology of Long Valley caldera, Mono county, California, *J. Geophys. Res.*, *81*(5), 725-744.

Barckhausen, U., C. Ranero, R. von Huene, S. Cande, and H. Roeser (2001), Revised tectonic boundaries in the Cocos Plate off Costa Rica: Implications for the segmentation of the convergent margin and for plate tectonic models, *J. Geophys. Res.*, *106*(B9), 19,207-19,220, doi:10.1029/2001JB000238, 2001.

Battaglia, M., C. Roberts, and P. Segall (1999), Magma intrusion beneath Long Valley caldera confirmed by temporal changes in gravity, *Science*, *285*, 2,119-2,122.

Battaglia, M., P. Segall, J. Murray, P. Cervelli, and J. Langbein (2003a), The mechanics of unrest at Long Valley caldera, California: 1. Modeling the geometry of the source using GPS, leveling and two-color EDM data, *J. Volcanol. Geotherm. Res.*, *127*, 195-217.

Battaglia, M., P. Segall, and C. Roberts (2003b), The mechanics of unrest at Long Valley caldera, California: 2. Constraining the nature of the source using geodetic and micro-gravity data, *J. Volcanol. Geotherm. Res.*, *127*, 219-245.

Bell, R. E., L. C. McNeill, J .M. Bulland, T. J. Henstock (2008), Evolution of the western Gulf of Corinth, *Bull. Geol. Soc. Am.*, *120*, 156-178, doi:10.1130/B26212.1.

Benetatos, C., A. Kiratzi, C. Papazachos, and G. Karakaisis (2004), Focal mechanisms of shallow and intermediate depth earthquakes along the Hellenic Arc, *J. Geodyn.*, *37*(2), 253-296, doi:10.1016/j.jog.2004.02.002.

Bernard, P., and A. Zollo (1989), The Irpinia (Italy) 1980 Earthquake: Detailed Analysis of a Complex Normal Faulting, *J. Geophys. Res.*, *94*(B2), 1,631-1,647.

Bilek, S. L., and C. Lithgow-Bertelloni (2005), Stress changes in the Costa Rica subduction zone due to the 1999 M_w = 6.9 Quepos earthquake, *Earth Planet. Sci. Lett.*, *230*, 97–112, doi:10.1016/j.epsl.2004.11.020.

Bilek, S. L., S. Y. Schwartz, and H. R. DeShon (2003), Control of seafloor roughness on earthquake rupture behavior, *Geology*, *31*(5), 455-458, doi:10.1130/0091-7613(2003)031<0455:COSROE>2.0.CO;2.

Bilek, S. L., C. E. Elliott, and C. L. Bertelloni (2009), Triggered seismicity associated with the 1990 Nicoya, Costa Rica, M_w = 7.0 earthquake, *Geochem. Geophys. Geosyst.*, *10*, Q04S13, doi:10.1029/2008GC002317.

Bos, M. S., R. M. S. Fernandes, S. D. P. Williams, and L. Bastos (2008), Fast error analysis of continuous GPS observations, *J. Geod.*, *82*, 157-166.

Briole, P., et al. (2008), Multidisciplinary Study of the June 8, 2008, M_W = 6.4 Andravida Earthquake. *31st General Assembly*, European Seismol. Commission (Abstract).

Brown, J., G. C. Beroza, and D. R. Shelly (2008), An autocorrelation method to detect low frequency earthquakes within tremor, *Geophys. Res. Lett.*, *35*, L16305, doi:10.1029/2008GL034560.

Brown, J. R., G. C. Beroza, S. Ide, K. Ohta, D. R. Shelly, S. Y. Schwartz, W. Rabbel, M. Thorwart, and H. Kao (2009), Deep low-frequency earthquakes in tremor localize to the plate interface in multiple subduction zones, *Geophys. Res. Lett.*, *36*, L19306, doi:10.1029/2009GL040027.

Brown, K. M., M. D. Tryon, H. R. DeShon, L. M. Dorman, and S. Y. Schwartz (2005), Correlated transient fluid pulsing and seismic tremor in the Costa Rica subduction zone, *Earth Planet. Sci. Lett.*, *238*, 189-203, doi:10.1016/j.epsl.2005.06.055.

Bürgmann, R., M. G. Kogan, G. M. Steblov, G. Hilley, V. E. Levin, and E. Apel (2005), Interseismic coupling and asperity distribution along the Kamchatka subduction zone , *J. Geophys. Res.*, *110*, B07405, doi:10.1029/2005JB003648.

Burkart, B., and S. Self (1985), Extension and rotation of crustal blocks in northern Central America and effect on the volcanic arc, *Geology*, *13*(1), 22-26, doi:10.1130/0091-7613(1985)13<22:EAROCB>2.0.CO;2.

Bursik, M. and K. Sieh (1989), Range front faulting and volcanism in the Mono Basin, eastern California, *J. Geophys. Res.*, *94*(B11), 15,587-15,609.

Canora, C., J. J. Martínez-Díaz, P. Villamor, K. Berryman, J. A. Álvarez-Gómez, C. Pullinger, and R. Capote (2010), Geological and seismological analysis of the 13 February 2001 M_w 6.6 El Salvador earthquake: evidence for surface rupture and implications for seismic hazard, *Bull. Seismol. Soc. Am.*, *100*(6), 2873-2890, doi:10.1785/0120090377.

Carmichael, R. S. (1982), *CRC Handbook of Physical Properties of Rocks*, Vol. 2, CRC Press, Boca Raton, Florida.

Carr, M. J. (1976), Underthrusting and Quaternary faulting in northern Central America, *Geol. Soc. Am. Bull.*, *87*(5), 825-829, doi:10.1130/0016-7606(1976) 87<825:UAQFIN>2.0.CO;2.

Castle, R. O., J. E. Estrem, and J. C. Savage (1984), Uplift across Long Valley caldera, California, *J. Geophys. Res.*, *89*(B13), 11,507-11,516.

Chen, T., A. V. Newman, L. Feng, and H. M. Fritz (2009), Slip distribution from the 1 April 2007 Solomon Islands earthquake: A unique image of near-trench rupture, *Geophys. Res. Lett.*, *36*, L16307, doi:10.1029/2009GL039496.

Chlieh, M., J. P. Avouac, K. Sieh, D. H. Natawidjaja, and J. Galetzka (2008), Heterogeneous coupling of the Sumatran megathrust constrained by geodetic and paleogeodetic measurements , *J. Geophys. Res.*, *113*, B05305, doi:10.1029/2007JB004981.

Chouet, B. A. (1996), Long-period volcano seismicity: its source and use in eruption forecasting, *Nature*, *380*, 309-316.

Choy, G. L., and J. L. Boatwright (1995), Global patterns of radiated seismic energy and apparent stress, *J. Geophys. Res.*, *100*(B9), 18,205-18,228.

Correa-Mora, F., C. DeMets, E. Cabral-Cano, B. Marquez-Azua, and O. Diaz-Molina (2008), Interplate coupling and transient slip along the subduction interface beneath Oaxaca, Mexico. *Geophys. J. Int.*, *175*(1), 269-290, doi:10.1111/j.1365-246X.2008.03910.x.

Correa-Mora, F., C. DeMets, D. Alvarado, H. L. Turner, G. Mattioli, D. Hernandez, C. Pullinger, M. Rodriguez, and C. Tenorio (2009), GPS-derived coupling estimates for the Central America subduction zone and volcanic arc faults: El Salvador,

Honduras and Nicaragua, *Geophys. J. Int.*, *179*(3), 1279-1291, doi:10.1111/j.1365-246X.2009.04371.x.

Corti, G., E. Carminati, F. Mazzarini, and M. O. Garcia (2005), Active strike-slip faulting in El Salvador, Central America, *Geology*, *33*, 989-992, doi:10.1130/G21992.1.

Davis, E. E., and H. W. Villinger (2006), Transient formation fluid pressures and temperatures in the Costa Rica forearc prism and subducting oceanic basement: CORK monitoring at ODP sites 1253 and 1255, *Earth Planet. Sci. Lett.*, *245*, 232-244, doi:10.1016/j.epsl.2006.02.042.

Dawson, P. B., J. R. Evans, and H. M. Iyer (1990), Teleseismic tomography of the compressional wave velocity structure beneath the Long Valley region, California, *J. Geophys. Res.*, *95*(B7), 11,021-11,050.

DeMets, C. (2001), A new estimate for present-day Cocos-Caribbean plate motion: Implications for slip along the Central American volcanic arc, *Geophys. Res. Lett.*, *28*(21), 4043-4046, doi:10.1029/2001GL013518.

DeMets, C. (2002), Reply to comment on "A new estimate for present-day Cocos-Caribbean plate motion: Implications for slip along the Central American volcanic arc" by Marco Guzmán-Speziale and Juan Martín Gómez, *Geophys. Res. Lett.*, *29*(20), 1946, doi:10.1029/2002GL015384.

DeMets, C., R. G. Gordon, and D. F. Argus (2010), Geologically current plate motions, *Geophys. J. Int.*, *181*, 1-80, doi:10.1111/j.1365-246X.2009.04491.x.

Denlinger, R. P., and F. Riley (1984), Deformation of Long Valley caldera, Mono County, California, from 1975 to 1982, *J. Geophys. Res.*, *89*(B10), 8,303-8,314.

DeShon, H. R. and S. Y. Schwartz (2004), Evidence for serpentinization of the forearc mantle wedge along the Nicoya Peninsula, Costa Rica, *Geophys. Res. Lett.*, *31*, L21611, doi:10.1029/2004GL021179.

DeShon, H. R., S. Y. Schwartz, S. L. Bilek, L. M. Dorman, V. Gonzalez, J. M. Protti, E. R. Flueh, and T. H. Dixon (2003), Seismogenic zone structure of the southern Middle America Trench, Costa Rica, *J. Geophys. Res.*, *108*(B10), 2491, doi:10.1029/2002JB002294.

DeShon, H. R., S. Y. Schwartz, A. V. Newman, V. Gonzalez, J. M. Protti, L. M. Dorman, T. Dixon, D. E. Sampson, and E. R. Flueh (2006), Seismogenic zone structure beneath the Nicoya Peninsula, Costa Rica, from three-dimensional local earthquake P- and S-wave tomography, *Geophys. J. Int.*, *164*, 1091-24, doi:10.1111/j.1365-246X.2005.02809.x.

Dewey, J. W., et al. (2007), Seismicity Associated with the Sumatra–Andaman Islands Earthquake of 26 December 2004, *Bull. Seismol. Soc. Am.*, *97*(1A), S25-S42, doi: 10.1785/0120050626.

Dixon, T. H., A. Mao, M. Bursik, M. Heflin, J. Langbein, R. Stein, and F. Webb (1997), Continuous monitoring of surface deformation at Long Valley Caldera, California, with GPS, *J. Geophys. Res.*, *102*(B6), 12,017-12,034.

Dixon, T. H., M. Miller, F. Farina, H. Wang, and D. Johnson (2000), Present-day motion of the Sierra Nevada block and some tectonic implications for the Basin and Range province, North American Cordillera, *Tectonics*, *19*(1), 1-24, doi:10.1029/1998TC001088.

Dixon, T. H., Y. Jiang, S. Wdowinski, S. Y. Schwartz, M. Protti, V. M. Gonzáez (2010), Episodic slip events measured by a continuous GPS network on the Nicoya Peninsula, Costa Rica, *Eos Trans. AGU*, *91*(47), Fall Meet. Suppl., Abstract G41C-01.

Doutsos, T., and S. Kokkalas (2001), Stress and deformation patterns in the Aegean region, *J. Struct. Geol.*, *23*, 455-472, doi:10.1016/S0191-8141(00)00119-X.

Du, Y., A. Aydin, and P. Segall (1992), Comparison of various inversion techniques as applied to the determination of a geophysical deformation model for the 1983 Borah Peak earthquake, *Bull. Seismol. Soc. Am.*, *82*(4), 1840-1866.

Ekström, G., A. M. Dziewonski, N. N. Maternovskaya, and M. Nettles (2005), Global seismicity of 2003: Centroid-moment-tensor solutions for 1087 earthquakes. *Phys. Earth Planet. Inter.*, *148*(2-4), 327-351, doi: 10.1016/j.pepi.2004.09.006.

Feng, L., A. V. Newman, and T. Chen (2009), Coseismic, episodic, and interseismic slip: Does surface roughness or strain energy control its distribution? *Eos Trans. AGU*, *90*(52), Fall Meet. Suppl., Abstract T14A-07.

Ferentinos, G., M. Brooks, and T. Doutsos (1985), Quaternary tectonics in the Gulf of Patras, western Greece, *J. Struct. Geol.*, *7*(6), 713-717, doi:10.1016/ 0191-8141(85)90146-4.

Fernandes, R. M. S., B. A. C. Ambrosius, R. Noomen, L. Bastos, M. J. R. Wortel, W. Spakman, and R. Govers (2003), The relative motion between Africa and Eurasia as derived from ITRF2000 and GPS data, *Geophys. Res. Lett.*, *30*(16), 1828, doi:10.1029/2003GL017089.

Fialko, Y., M. Simons, and Y. Khazan (2001), Finite source modeling of magmatic unrest in Socorro, New Mexico, and Long Valley, California, *Geophys. J. Int.*, *146*, 191-200.

Fialko, Y., D. Sandwell, M. Simons, and P. Rosen (2005), Three-dimensional deformation caused by the Bam, Iran, earthquake and the origin of shallow slip deficit, *Nature*, *435*, 295-299, doi:10.1038/nature03425.

Fink, J. H., (1985), The geometry of silicic dikes beneath the Inyo Domes, *J. Geophys. Res.*, *90*(B13), 11,127--11,133.

Fisher, A. T., et al. (2003), Abrupt thermal transition reveals hydrothermal boundary and role of seamounts within the Cocos Plate, *Geophys. Res. Lett.*, *30*(11), 1550, doi:10.1029/2002GL016766.

Fisher, D. M., T. W. Gardner, P. B. Sak, J. D. Sanchez, K. Murphy, and P. Vannucchi (2004), Active thrusting in the inner forearc of an erosive convergent margin, Pacific coast, Costa Rica, *Tectonics*, *23*, TC2007, doi:10.1029/2002TC001464.

Flotté, N., D. Sorel, C. Müller, and J. Tensi (2005), Along strike changes in the structural evolution over a brittle detachment fault: Example of the Pleistocene Corinth-Patras rift (Greece), *Tectonophysics*, *403*, 77-94, doi:10.1016/j.tecto.2005.03.015.

Foulger, G. R., B. R. Julian, A. M. Pitt, D. P. Hill, P. E. Malin, and E. Shalev, Three-dimensional crustal structure of Long Valley caldera, California, and evidence for the migration of CO_2 under Mammoth Mountain, *J. Geophys. Res.*, *108*(B3), 2147, doi:10.1029/2000JB000041.

Funk, J., P. Mann, K. McIntosh, and J. Stephens (2009), Cenozoic tectonics of the Nicaraguan depression, Nicaragua, and Median Trough, El Salvador, based on

seismic-reflection profiling and remote-sensing data, *Geol. Soc. Am. Bull.*, *121*(11-12), 1491-1521, doi:10.1130/B26428.1.

Ganas, A., and T.Parsons (2009), Three-dimensional model of Hellenic Arc deformation and origin of the Cretan uplift, *J. Geophys. Res.*, *114*, B06404, doi:10.1029/2008JB005599.

Ganas, A., E. Serpelloni, G. Drakatos, M. Kolligri, I. Adamis, Ch. Tsimi, and E. Batsi (2009), The M_W 6.4 Achaia-Elia (Western Greece) Earthquake of 8 June 2008: Seismological, Field, GPS Observations, and Stress Modeling, *J. Earthquake Eng.*, *13*, 1,101-1,124, doi:10.1080/13632460902933899.

Gallovič, F., J. Zahradn ík, D. Křížová, V. Plicka, E. Sokos, A. Serpetsidaki, and. G.-A Tselentis (2009), From earthquake centroid to spatial-temporal rupture evolution: M_W 6.3 Movri Mountain earthquake, June 8, 2008, Greece, *Geophys. Res. Lett.*, *36*, L21310, doi:10.1029/2009GL040283.

Ghosh, A., A. V. Newman, A. M. Thomas, and G. T. Farmer (2008), Interface locking along the subduction megathrust from *b*-value mapping near Nicoya Peninsula, Costa Rica, *Geophys. Res. Lett.*, *35*, L01301, doi:10.1029/2007GL031617.

Girard, G., and B. van Wyk de Vries (2005), The Managua Graben and Las Sierras-Masaya volcanic complex (Nicaragua); pull-apart localization by an intrusive complex: results from analogue modeling, *J. Volcanol. Geotherm. Res.*, *144*, 37-57, doi:10.1016/j.jvolgeores.2004.11.016.

Gourmelen, N., T. H. Dixon, F. Amelung, G. Schmalzle (2011), Acceleration and evolution of faults: an example from the Hunter Mountain–Panamint Valley fault zone, Eastern California. *Earth Planet. Sci. Lett.*, *301*, 337-344 doi:10.1016/j.epsl2010.11.016.

Hammond, W. C., and W. Thatcher (2007), Crustal deformation across the Sierra Nevada, northern Walker Lane, Basin and Range transition, western United States measured with GPS, 2000-2004, *J. Geophys. Res.*, *112*, B05411.

Harris, R. A., and P. Segall (1987), Detection of a locked zone at depth on the Parkfield, California, segment of the San Andreas fault, *J. Geophys. Res.*, *92*(B8), 7945-7962, doi:10.1029/JB092iB08p07945.

Harris, R. N., and K. Wang (2002), Thermal models of the Middle America Trench at the Nicoya Peninsula, Costa Rica, *Geophys. Res. Lett.*, *29*(21), 2010, doi:10.1029/2002GL015406.

Harlow, D. H., and R. A. White (1985), Shallow earthquakes along the volcanic chain in Central America: evidence for oblique subduction (abstract), *Earthquake Notes*, *55*, 28.

Hatzfeld, D., G. Pedotti, P. Hatzidimitriou, and K. Makropoulos (1990), The strain pattern in the western Hellenic Arc deduced from a microearthquake survey, *Geophys. J. Int.*, *101*(1), 181-202.

Hashimoto, C., A. Noda, T. Sagiya, and M. Matsu'ura (2009), Interplate seismogenic zones along the Kuril-Japan trench inferred from GPS data inversion, *Nat. Geosci.*, *2*, 141-144, doi:10.1038/ngeo421.

Heflin, M., et al. (1992), Global geodesy using GPS without fiducial sites, *Geophys. Res. Lett.*, *19*(2), 131-134, doi:10.1029/91GL02933.

Herring, T. A., R. W. King, and S. C.McClusky (2008), *Introduction to GAMIT/GLOBK, Release 10.3*, Mass. Inst. of Techonol., Cambridge, USA.

Hildreth, W. (2004), Volcanological perspectives on Long Valley, Mammoth Mountain, and Mono Craters: several contiguous but discrete systems, *J. Volcanol. Geotherm. Res.*, *136*, 169-198.

Hill, D. P. (1976), Structure of Long Valley Caldera, California, from a seismic refraction experiment, *J. Geophys. Res.*, *81*(5), 745-753.

Hill, D. P. (2006), Unrest in Long Valley caldera, California, 1978-2004, In: Troise, C., G. De Natale, and C. R. J. Kilburn, *Mechanisms of activity and unrest at large calderas*, *269*, 1-24, Geological Society, Special Publications, London.

Hill, D. P., E. Kissling, J. H. Luetgert, and U. Kradolfer (1985), Constraints on the upper crustal structure of the Long Valley-Mono Craters volcanic complex, eastern California, from seismic refraction measurements, *J. Geophys. Res.*, *90*(B13), 11,135-11,150.

Hill, D. P., J. O. Langbein, and S. Prejean (2003), Relations between seismicity and deformation during unrest in Long Valley caldera, California, from 1995 through 1999, *J. Volcanol. Geotherm. Res.*, *127*, 175-193.

Hollenstein, Ch., A. Geiger, H.-G. Kahle, and G. Veis (2006), CGPS time-series and trajectories of crustal motion along the West Hellenic Arc, *Geophys. J. Int.*, *164*(1), 182-191, doi:10.1111/j.1365-246X.2005.02804.x.

Hollenstein, Ch., M. D. Muller, A. Geiger, and H.-G. Kahle (2008), Crustal motion and deformation in Greece from a decade of GPS measurements, 1993-2003, *Tectonophysics*, *449*, 17-40, doi:10.1016/j.tecto.2007.12.006.

Howle, J. F., J. Langbein, C. D. Farrar, and S. K. Wilkinson (2003), Deformation near the Casa Diablo geothermal well field and related processes Long Valley caldera, Eastern California, 1993-2000, *J. Volcanol. Geotherm. Res.*, 127, 365-390.

Husen, S., E. Kissling, and R. Quintero (2002), Tomographic evidence for a subducted seamount beneath the Gulf of Nicoya, Costa Rica: The cause of the 1990 M_w = 7.0 Gulf of Nicoya earthquake, *Geophys. Res. Lett.*, *29*(8), doi:10.1029/2001GL014045.

Hyndman, R. D., M. Yamano, and D. A. Oleskevich (1997), The seismogenic zone of subduction thrust faults, *Island Arc*, 6, 244-260.

Ide, S., D. R. Shelly, and G. C. Beroza (2007), The mechanism of deep low frequency earthquakes: Further evidence that deep non-volcanic tremor is generated by shear slip on the plate interface, *Geophys. Res. Lett.*, *34*, L03308, doi:10.1029/2006GL028890.

Ito, Y., K. Obara, K. Shiomi, S. Sekine, and H. Hirose (2007), Slow earthquakes coincident with episodic tremors and slow slip events, *Science*, *315*, 503-506, doi:10.1126/science.1134454.

Ito, Y., K. Obara, T. Matsuzawa, and T. Maeda (2009), Very low frequency earthquakes related to small asperities on the plate boundary at the locked to aseismic transition, *J. Geophys. Res.*, *114*, B00A13, doi:10.1029/2008JB006036.

Ihmlé, P. F. (1996), Monte Carlo slip inversion in the frequency domain: Application to the 1992 Nicaragua Slow Earthquake, *Geophys. Res. Lett.*, *23*(9), 913-916, doi:10.1029/96GL00872.

Iinuma, T., et al. (2004), Inter-plate coupling in the Nicoya Peninsula, Costa Rica, as deduced from a trans-peninsula GPS experiment, *Earth Planet. Sci. Lett.*, *223*, 203-212, doi:10.1016/j.epsl.2004.04.016.

Jarrard, R. D. (1986a), Terrane motion by strike-slip faulting of forearc slivers, *Geology*, *14*(9), 780-783, doi:10.1130/0091-7613(1986)14<780:TMBSFO>2.0.CO;2.

Jarrard, R. D. (1986b), Relations among subduction parameters, *Rev. Geophys.*, *24*(2), 217-284, doi:10.1029/RG024i002p00217.

Jónsson, S., H. Zebker, P. Segall, and F. Amelung (2002). Fault slip distribution of the 1999 M_W 7.1 Hector Mine, California earthquake, estimated from satellite radar and GPS measurements, *Bull. Seismol. Soc. Am. 92*(4), 1377-1389, doi:10.1785/0120000922.

Kamberis, E., S. Sotiropoulos, O. Aximniotou, S. Tsaila-Monopoli, and C. Ioakim (2000), Late Cenozoic deformation of the Gavrovo and Ionian zones in NW Peloponnesos (Western Greece), *Ann. Geofisica*, *43*(5), 905-919.

Kamberis, E., A. Pavlopoulos, S. Tsaila-Monopolis, S. Sotiropoulos, and C.Ioakim (2005), Paleogene deep-water sedimentation and paleogeography of foreland basins in the NW Peloponnese (Greece), *Geologica Carpathica*, *56*(6), 503-515.

Kao, H., S.-J. Shan, H. Dragert, G. Rogers, J. F. Cassidy, and K. Ramachandran (2005), A wide depth distribution of seismic tremors along the northern Cascadia margin, *Nature*, *436*, doi:10.1038/nature03903.

Kelleher, P. C., and K. L. Cameron (1990), The geochemistry of the Mono Craters-Mono lake islands volcanic complex, eastern California, *J. Geophys. Res.*, *95*(B11), 17,643-17,659.

Kellogg, J. N., and T. H. Dixon (1990), Central and South America GPS geodesy - CASA Uno, *Geophys. Res. Lett.*, *17*(3), 195-198, doi:10.1029/GL017i003p00195.

Kiratzi, A., et al. (2008), The April 2007 earthquake swarm near Lake Trichonis and implications for active tectonics in western Greece, *Tectonophysics*, *452*, 51-65, doi:10.1016/j.tecto.2008.02.009.

Kleinbaum, D. G., and L. L. Kupper (1978), *Applied regression analysis and other multivariable methods*, Duxbury Press, North Scituate, MA, USA.

Konstantinou, K. I., N. S. Melis, S.-J. Lee, C. P. Evangelidis, and K.Boukouras (2009), Rupture process and aftershocks relocation of the 8 June 2008 M_W 6.4 earthquake in northwest Peloponnese, western Greece, *Bull. Seism. Soc. Am.*, *99*(6), 3374-3389. doi:10.1785/0120080301.

Kostoglodov, V., A. Husker, N. M. Shapiro, J. S. Payero, M. Campillo, N. Cotte, and R. Clayton (2010), The 2006 slow slip event and nonvolcanic tremor in the Mexican subduction zone, *Geophys. Res. Lett.*, *37*, L24301, doi:10.1029/2010GL045424.

Kreemer, C., and N. Chamot-Rooke (2004), Contemporary kinematics of the southern Aegean and the Mediterranean Ridge, *Geophys. J. Int.*, *157*(3), 1377-1392, doi:10.1111/j.1365-246X.(2004),02270.x.

LaBonte, A. L., K. M. Brown, and Y. Fialko (2009), Hydrologic detection and finite element modeling of a slow slip event in the Costa Rica prism toe, *J. Geophys. Res.*, *114*, B00A02, doi:10.1029/2008JB005806.

LaFemina, P., T. H. Dixon, R. Govers, E. Norabuena, H. Turner, A. Saballos, G. Mattioli, M. Protti, and W. Strauch (2009), Fore-arc motion and Cocos Ridge collision in Central America, *Geochem. Geophys. Geosyst.*, *10*, Q05S14, doi:10.1029/2008GC002181.

Lagios, E., V. Sakkas, P. Papadimitriou, I. Parcharidis, B. N. Damiata, K. Chousianitis, and S. Vassilopoulou (2007), Crustal deformation in the Central Ionian Islands (Greece): Results from DGPS and DInSAR analyses (1995-2006), *Tectonophysics*, *444*, 119-145, doi:10.1016/j.tecto.2007.08.018.

Langbein, J. (1989), Deformation of the Long Valley caldera, eastern California from mid-1983 to mid-1988: measurements using a two-color geodimeter, *J. Geophys. Res.*, *94*(B4), 3,833-3,849.

Langbein, J. (2003), Deformation of the Long Valley Caldera, California: inferences from measurements from 1988 to 2001, *J. Volcanol. Geotherm. Res.*, *127*, 247-267.

Langbein, J. (2004), Noise in two-color electronic distance meter measurements revisited, *J. Geophys. Res.*, *109*, B04406, doi:10.1029/2003JB002819.

Langbein, J. (2008), Noise in GPS displacement measurements from Southern California and Southern Nevada, *J. Geophys. Res.*, *113*, B05405, doi:10.1029/2007JB005247.

Langbein, J., D. Dzurisin, G. Marshall, R. Stein, and J. Rundle (1995), Shallow and peripheral volcanic sources of inflation revealed by modeling two-color geodimeter and leveling data from Long Valley caldera, California, 1988-1992, *J. Geophys. Res.*, *100*(B7), 12,487-12,495.

Langbein, J., D. P. Hill, T. N. Parker, and S. K. Wilkinson (1993), An episode of reinflation of the Long Valley caldera, eastern California: 1989-1991, *J. Geophys. Res.*, *98*(B9), 15,851-15,870.

Langbein, J., and H. Johnson (1997), Correlated errors in geodetic time series: implications for time-dependent deformation, *J. Geophys. Res.*, *102*(B1), 591-603.

La Rocca, M., D. Galluzzo, S. Malone, W. McCausland, G. Saccorotti, and E. Del Pezzo (2008), Testing small-aperture array analysis on well-located earthquakes, and application to the location of deep tremor, *Bull. Seismol. Soc. Am.*, *98*(2), doi:10.1785/0120060185.

La Rocca, M., K. C. Creager, D. Galluzzo, S. Malone, J. E. Vidale, J. R. Sweet, and A. G. Wech (2009), Cascadia tremor located near plate interface constrained by S minus P wave times, *Science*, *323*, 620-623, doi:10.1126/science.1167112.

La Rocca, M., D. Galluzzo, S. Malone, W. McCausland, and E. Del Pezzo (2010), Array analysis and precise sourcelocation of deep tremor in Cascadia, *J. Geophys. Res.*, *115*, B00A20, doi:10.1029/2008JB006041.

Lewis, J. C., A. C. Boozer, A. Lopez, and W. Montero (2008), Collision versus sliver transport in the hanging wall at the Middle America subduction zone: Constraints from background seismicity in central Costa Rica, *Geochem. Geophys. Geosyst.*, *9*(7), Q07S06, doi:10.1029/2007GC001711.

Le Pichon, X., N. Chamot-Rooke, S. Lallemant, R. Noomenand, and G. Veis (1995), Geodetic determination of the kinematics of central Greece with respect to Europe: Implications for eastern Mediterranean tectonics, *J. Geophys. Res.*, 100(B7), 12,675-12,690.

Lonsdale, P. (2005), Creation of the Cocos and Nazca plates by fission of the Farallon plate, *Tectonophysics*, *404*, 237-264, doi:10.1016/j.tecto.2005.05.011.

Louvari, E., A. A. Kiratzi, and B. C. Papazachos (1999), The Cephalonia Transform Fault and its extension to western Lefkada Island (Greece), *Tectonophysics*, *308*, 223-236, doi:10.1016/S0040-1951(99)00078-5.

Lundgren, P., M. Protti, A. Donnellan, M. Heflin, E. Hernandez, and D. Jefferson (1999), Seismic cycle and plate margin deformation in Costa Rica: GPS observations from 1994 to 1997, *J. Geophys. Res.*, *104*(B12), 28,915-28,926, doi:10.1029/1999JB900283.

Lyon-Caen, H. et al. (1988), The 1986 Kalamata (South Peloponnesus) earthquake: detailed study of a normal fault, evidences for east-west extension in the Hellenic Arc, *J. Geophys. Res.*, *93*(B12), 14,967-15,000.

Lyon-Caen, H., et al. (2006), Kinematics of the North American-Caribbean-Cocos plates in Central America from new GPS measurements across the Polochic-Motagua fault system, *Geophys. Res. Lett.*, *33*, L19309, doi:10.1029/2006GL027694.

MacMillan, I., P. B. Gans, and G. Alvarado (2004), Middle Miocene to present plate tectonic history of the southern Central American Volcanic Arc, *Tectonophysics*, *392*, 325-348, doi:10.1016/j.tecto.2004.04.014.

Mao, A., C. G. A. Harrison, and T. H. Dixon (1999), Noise in GPS coordinate time series, *J. Geophys. Res.*, *104*(B2), 2797-2816, doi:10.1029/1998JB900033.

Margaris, B., et al. (2010), The 8 June 2008 M_W 6.5 Achaia-Elia, Greece Earthquake: Source Characteristics, Ground Motions, and Ground Failure, *Earthquake Spectra, 26*, 399-424, doi:10.1193/1.3353626.

Marinos, P., and E. Hoek (2001), Estimating the geotechnical properties of heterogeneous rock masses such as flysch, *Bull. Eng. Geol. Environ.*, *60*, 85-92, doi: 10.1007/s100640000090.

Marone, C. (1998), Laboratory-derived friction laws and their application to seismic faulting, *Annu. Rev. Earth Planet. Sci.*, *26*, 643-696, doi:10.1146/annurev.earth.26.1.643.

Marone, C. J., C. H. Scholz, and R. Bilham (1991), On the Mechanics of Earthquake Afterslip, *J. Geophys. Res.*, *96*(B5), 8,441-8,452, doi:10.1029/91JB00275.

Marshall, G. A., J. Langbein, R. S. Stein, M. Lisowski, and J. Svarc (1997), Inflation of Long Valley caldera, California, Basin and Range strain, and possible Mono Craters dike opening from 1990-94 GPS surveys, *Geophys. Res. Lett.*, *24*(9), 1,003-1,006.

Marshall, J. S., and R. S. Anderson (1995), Quaternary uplift and seismic cycle deformation, Peninsula de Nicoya, Costa Rica, *Geol. Soc. Am. Bull.*, *107*(4), 463-473, doi:10.1130/0016-7606(1995)107<0463:QUASCD>2.3.CO;2.

Marshall, J., D. Fisher, and T. Gardner (2000), Central Costa Rica deformed belt: Kinematics of diffuse faulting across the western Panama block, *Tectonics*, *19*(3), 468-492, doi:10.1029/1999TC001136.

Martínez-Díaz, J. J., J. A. Álvarez-Gómez, B. Benito, and D. Hernández (2004), Triggering of destructive earthquakes in El Salvador, *Geology*, *32*(1), 65-68, doi:10.1130/G20089.1.

McCaffrey, R. (1992), Oblique plate convergence, slip vectors, and forearc deformation, *J. Geophys. Res.*, *97*(B6), 8905-8915, doi:10.1029/92JB00483.

McCaffrey, R. (2002), Crustal block rotations and plate coupling, in *Plate Boundary Zones*, *Geodyn. Ser.*, vol. 20, edited by S. Stein and J. Freymueller, pp. 101-122, AGU, Washington, D. C.

McCausland, W., S. Malone, and D. Johnson (2005), Temporal and spatial occurrence of deep non-volcanic tremor: From Washington to northern California, *Geophys. Res. Lett.*, *32*, L24311, doi:10.1029/2005GL024349.

McClusky, S., et al. (2000), Global Positioning System constraints on plate kinematics and dynamics in the eastern Mediterranean and Caucasus, *J. Geophys. Res.*, *105*(B3), 5,695-5,719.

McTigue, D. F. (1987), Elastic stress and deformation near a finite spherical magma body: resolution of the point source paradox, *J. Geophys. Res.*, *92*(B12), 12,931-12,940.

Mogi, K. (1958), Relations between the eruption of various volcanoes and the deformation of the ground surface around them, *Bull. Earthquake Res. Inst. Univ. Tokyo*, *36*, 99-134.

Moore, J. C., and D. Saffer (2001), Updip limit of the seismogenic zone beneath the accretionary prism of southwest Japan: An effect of diagenetic to low-grade metamorphic processes and increasing effective stress, *Geology*, *29*(2), 183-186.

Moreno, M., M. Rosenau, and O. Onchen (2010), 2010 Maule earthquake slip correlates with pre-seismic locking of Andean subduction zone, *Nature*, *467*, 198-202, doi:10.1038/nature09349.

Motulsky, H. J., and A. Christopoulos (2003), *Fitting models to biological data using linear and nonlinear regression. A practical guide to curve fitting*, GraphPad Software Inc., San Diego, CA, USA, www.graphpad.com.

Moyer, P. A., S. L. Bilek, and W. S. Phillips (2011), Apparent stress variations near the Osa Peninsula, Costa Rica, influenced by subducted bathymetric features, *Geophys. Res. Lett.*, *38*, L02304, doi:10.1029/2010GL045955.

Newman, A. V., and E. A. Okal (1998), Teleseismic estimates of radiated seismic energy: The E/M_0 discriminant for tsunami earthquakes, *J. Geophys. Res.*, *103*(B11), 26,885-26,898.

Newman, A. V., and J. A. Convers, A rapid high-frequency energy-duration discriminant for very large and tsunami earthquakes, *Geophys. Res. Lett.*, in review.

Newman, A. V., T. H. Dixon, G. I. Ofoegbu, and J. E. Dixon (2001), Geodetic and seismic constrains on recent activity at Long Valley caldera, California: evidence for viscoelastic rheology, *J. Volcanol. Geotherm. Res.*, *105*, 183-206.

Newman, A. V., S. Y. Schwartz, V. Gonz âez, H. R. DeShon, J. M. Protti, and L. M. Dorman (2002), Along-strike variability in the seismogenic zone below Nicoya Peninsula, Costa Rica, *Geophys. Res. Lett.*, *29*(2), 1977, doi:10.1029/2002GL015409.

Newman, A. V., T. H. Dixon, and N. Gourmelen (2006), A four-dimensional viscoelastic deformation model for Long Valley Caldera, California, between 1995 and 2000, *J. Volcanol. Geotherm. Res.*, *150*, 244-269.

Nishenko, S. P. (1991), Circum-Pacific seismic potential: 1989-1999, *Pure Appl. Geophys.*, *135*(2), 169-259, doi:10.1007/BF00880240.

Norabuena, E., et al. (2004), Geodetic and seismic constraints on some seismogenic zone processes in Costa Rica, *J. Geophys. Res.*, *109*, B11403, doi:10.1029/2003JB002931.

Obara, K. (2002), Nonvolcanic deep tremor associated with subduction in southwest Japan, *Science*, *296*, 1679-1681.

Obara, K., H. Hirose, F. Yamamizu, and K. Kasahara (2004), Episodic slow slip events accompanied by non-volcanic tremors in southwest Japan subduction zone, *Geophys. Res. Lett.*, *31*, L23602, doi:10.1029/2004GL020848.

Okada, Y. (1992), Internal deformation due to shear and tensile faults in a half-space, *Bull. Seismol. Soc. Am.*, *82*(2), 1018-1040.

Oleskevich, D. A., R. D. Hyndman, and K. Wang (1999), The updip and downdip limits to great subduction earthquakes: Thermal and structural models of Cascadia, south Alaska, SW Japan, and Chile, *J. Geophys. Res.*, *104*(B7), 14,965-14,991, doi:10.1029/1999JB900060.

Outerbridge, K. C., T. H. Dixon, S. Y. Schwartz, J. I. Walter, M. Protti, V. Gonzalez, J. Biggs, M. Thorwart, and W. Rabbel (2010), A tremor and slip event on the Cocos-Caribbean subduction zone as measured by a global positioning system (GPS) and seismic network on the Nicoya Peninsula, Costa Rica, *J. Geophys. Res.*, *115*, B10408, doi:10.1029/2009JB006845.

Papanastassiou, D., J. Latoussakis, and G. Stavrakakis (2001), A revised catalogue of earthquakes in the broader area of Greece for the period 1950-2000, *Proc. 9th Int. Congr. Geol. Soc. Greece, Athens, Bull. Geol. Soc. Greece*, XXXIV/4, 1,563–1,566.

Patino, L. C., M. J. Carr, and M. D. Feigenson (2000), Local and regional variations in Central American arc lavas controlled by variations in subducted sediment input, *Contrib. Mineral. Petrol.*, *138*(3), 265-283.

Payero, J. S., V. Kostoglodov, N. Shapiro, T. Mikumo, A. Iglesias, X. Perez-Campos, and R. W. Clayton (2008), Nonvolcanic tremor observed in the Mexican subduction zone, *Geophys. Res. Lett.*, *35*, L07305, doi:10.1029/2007GL032877.

Peacock, S. M. (2009), Thermal and metamorphic environment of subduction zone episodic tremor and slip, *J. Geophys. Res.*, *114*, B00A07, doi:10.1029/2008JB005978.

Peng, Z., and J. Gomberg (2010), An integrated perspective of the continuum between earthquakes and slow-slip phenomena, *Nat. Geosci.*, *3*, 599-607, doi:10.1038/ngeo940.

Peterson, C. L., and D. H. Christensen (2009), Possible relationship between nonvolcanic tremor and the 1998–2001 slow slip event, south central Alaska, *J. Geophys. Res.*, *114*, B06302, doi:10.1029/2008JB006096.

Plafker, G. (1976), Tectonic aspects of the Guatemalan earthquake of 4 February 1976, *Science*, *193*, 1201-1208.

Prejean, S., W. Ellsworth, M. Zoback, and F. Waldhauser (2002), Fault structure and kinematics of the Long Valley Caldera region, California, revealed by high-accuracy earthquake hypocenters and focal mechanism stress inversions, *J. Geophys. Res.*, *107*(B12), 2355, doi:10.1029/2001JB001168.

Press, W. H., S. A. Teukolsky, W. T. Vetterling, and B. P Flannery (1992), *Numerical recipes in FORTRAN: the art of scientific computing*, 2nd ed., Cambridge Univ. Press, New York, NY, USA.

Protti, M., F. Güendel, and K. McNally (1994), The geometry of the Wadati-Benioff zone under southern Central America and its tectonic significance: results from a high-resolution local seismographic network, *Phys. Earth Planet. Inter.*, *84*, 271-287, doi:10.1016/0031-9201(94)90046-9.

Protti, M., et al. (1995), The March 25, 1990 (M_w = 7.0, M_L = 6.8), earthquake at the entrance of the Nicoya Gulf, Costa Rica: Its prior activity, foreshocks, aftershocks, and triggered seismicity, *J. Geophys. Res.*, *100*(B10), 20,345-20,358, doi:10.1029/94JB03099.

Protti, M., M. F. Güendel, and E. Malavassi (2001), *Evaluación del Potencial Sísmico de la Península de Nicoya*, 1st ed., 144 pp., Editorial Fundación Universidad Nacional, Heredia, Costa Rica.

Protti, M., V. González, T. Kato, T. Iinuma, S. Miyazaki, K. Obana, Y. Kaneda, P. LaFemina, T. Dixon, and S. Y. Schwartz (2004), A creep event on the shallow

interface of the Nicoya Peninsula, Costa Rica seismogenic zone, *Eos Trans. AGU*, *85*(47), Fall Meet. Suppl., Abstract S41D-07.

Ranero, C. R., J. Phipps Morgan, K. McIntosh, and C. Reichert (2003), Bending-related faulting and mantle serpentinization at the Middle America trench, *Nature, 425*, 367-373, doi:10.1038/nature01961.

Reilinger, R., et al. (2006), GPS constraints on continental deformation in the Africa-Arabia-Eurasia continental collision zone and implications for the dynamics of plate interactions, *J. Geophys. Res., 111*, B05411, doi:10.1029/2005JB004051.

Rodriguez, M., C. DeMets, R. Rogers, C. Tenorio, and D. Hernandez (2009), A GPS and modeling study of deformation in northern Central America, *Geophys. J. Int.*, 178**,** 1733-1754, doi:10.1111/j.1365-246X.2009.04251.x.

Rogers, G., and H. Dragert (2003), Episodic tremor and slip on the Cascadia subduction zone: the chatter of silent slip, *Science, 300*, 1942-1943, doi:10.1126/science.1084783.

Rogers, R. D., 2003. Jurassic-Recent tectonic and stratigraphic history of the Chortis block of Honduras and Nicaragua (northern Central America), *PhD thesis*, University of Texas at Austin, Austin.

Rogers, R. D. and P. Mann (2007), Transtensional deformation of the western Caribbean-North America plate boundary zone, in *Geologic and Tectonic Development of the Caribbean Plate Boundary in Northern Central America*, edited by P. Mann, pp. 37–64, *Geol. Soc. Am. Spec. Paper 428*, The Geological Society of America, Boulder, doi:10.1130/2007.2428(02).

Rosen, P.A., S. Henley, G. Peltzer, and M. Simons (2004), Updated Repeat Orbit Interferometry Package Released, *Eos Trans. AGU*, *85*(5), 47, doi:10.1029/2004EO050004.

Rosencrantz, E., and P. Mann (1991), SeaMARC II mapping of transform faults in the Cayman Trough, *Geology*, *19*, 690-693, doi:10.1130/0091-7613(1991)019<0690:SIMOTF>2.3.CO;2.

Ryall, A., and F. Ryall (1983), Spasmodic tremor and possible magma injection in Long Valley caldera, eastern California, *Science*, *219*, 1,432-1,433.

Sanders, C. O., S. C. Ponko, L. D. Nixon, and E. A. Schwartz (1995), Seismological evidence for magmatic and hydrothermal structure in Long Valley caldera from local earthquake attenuation and velocity tomography, *J. Geophys. Res.*, *100*(B5), 8,311-8,326.

Satake, K. (1994), Mechanism of the 1992 Nicaragua Tsunami Earthquake, Geophys. *Res. Lett.*, *21*(23), 2519-2522, doi:10.1029/94GL02338.

Savage, J. (1983), A dislocation model of strain accumulation and release at a subduction zone, *J. Geophys. Res.*, *88*(B6), 4984-4996, doi:10.1029/JB088iB06p04984.

Savage, J., and R. Burford (1973), Geodetic determination of relative plate motion in Central California, *J. Geophys. Res.*, *78*(5), 832-845, doi:10.1029/JB078i005p00832.

Savage, J. C., and M. M. Clark (1982), Magmatic resurgence in Long Valley caldera, California: possible cause of the 1980 Mammoth lakes earthquakes, *Science*, *217*, 531-533.

Savage, J. C., and R. S. Cockerham (1984), Earthquake swarm in Long Valley caldera, California, January 1983: evidence for dike inflation, *J. Geophys. Res.*, 89(B10), 8,315-8,324.

Savage, J. C., M. Lisowski, W. H. Prescott, and N. E. King (1981), Strain accumulation near the epicenter of the 1978 Bishop and 1980 Mammoth Lakes, California, earthquakes, *Bull. Seismol. Soc. Am.*, *71*, 465-476.

Schmalzle, G., T. Dixon, R. Malservisi, and R. Govers (2006), Strain accumulation across the Carrizo segment of the San Andreas Fault, California: Impact of laterally varying crustal properties , *J. Geophys. Res.*, *111*, B05403, doi:10.1029/2005JB003843.

Schwartz, S. Y., and H. R. DeShon (2007), Distinct updip limits to geodetic locking and microseismicity at the northern Costa Rica seismogenic zone: Evidence for two mechanical transitions, in *The Seismogenic Zone of Subduction Thrust Faults*, edited by T. H. Dixon and J. C. Moore, pp. 576-599, Columbia University Press, New York.

Screaton, E. J., and S. Ge (2007), Modeling of the effects of propagating thrust slip on pore pressures and implications for monitoring, *Earth Planet. Sci. Lett.*, *258*, 454-464, doi:10.1016/j.epsl.2007.04.004.

Shelly, D. R., G. C. Beroza, S. Ide, and S. Nakamula (2006), Low-frequency earthquakes in Shikoku, Japan, and their relationship to episodic tremor and slip, *Nature*, *442*, 188-191, doi:10.1038/nature04931.

Shelly, D. R., G. C. Beroza, and S. Ide (2007), Non-volcanic tremor and low-frequency earthquake swarms, *Nature*, *446*, 305-307, doi:10.1038/nature05666.

Siebert, L., and T. Simkin (2002), Volcanoes of the World: an illustrated catalog of Holocene volcanoes and their eruptions, *Global Volcanism Program Digital Inf. Ser.*, *GVP-3*, Smithsonian Inst, Washington, D. C. (http://www.volcano.si.edu/world/).

Simopoulos, K. 1985. *Foreign Travellers in Greece* (in Greek), 5th ed., 3 vols., Athens.

Smith, J. R. (1997), *Introduction to geodesy: the history and concepts of modern geodesy*, 224 pp., Wiley-Interscience, New York, USA.

Sorey, M. L., C. D. Farrar, G. A. Marshall, and J. F. Howle (1995), Effects of geothermal development on deformation in the Long Valley caldera, eastern California, 1985-1994, *J. Geophys. Res.*, *100*(B7), 12,475-12,486.

Sotiropoulos, S., E. Kamberis, M. V. Triantaphyllou, and T. Doutsos (2003), Thrust sequences in the central part of the External Hellenides, *Geol. Mag.*, *140*(6), 661-668, doi:10.1017/S0016756803008367.

Spinelli, G. A. and D. M. Saffer (2004), Along-strike variations in underthrust sediment dewatering on the Nicoya margin, Costa Rica related to the updip limit of seismicity, *Geophys. Res. Lett.*, *31*, L04613, doi:10.1029/2003GL018863.

Steck, L. K. (1995), Simulated Annealing Inversion of Teleseismic *P*-Wave Slowness and Azimuth for Crustal Velocity Structure at Long Valley Caldera, *Geophys. Res. Lett.*, *22*(4), 497-500.

Stein, S., and M. Wysession (2003), *An Introduction to Seismology, Earthquakes, and Earth Structure*, pp. 1-498, Blackwell Publishing, Berlin, Germany.

Stiros, S. C. (1995), Archaeological evidence of antiseismic constructions in antiquity, *Ann. Geofisica*, *38*(5-6), 725-736.

Stiros, S. C., P. A. Pirazzoli, J. Laborel, and F. Laborel-Deguen (1994), The 1953 earthquake in Cephalonia (Western Hellenic arc): coastal uplift and halotectonic faulting, *Geophys. J. Int., 117*, 834-849.

Strang, G., and K. Borre (1997), *Linear algebra, geodesy, and GPS*, 624 pp., Wellesley-Cambridge Press, Wellesley, MA, USA.

Suemnicht, G. A., and R. J. Varga (1988), Basement structure and implications for hydrothermal circulation patterns in the western moat of Long Valley caldera, California, *J. Geophys. Res.*, *93*(B11), 13,191-13,207.

Thomas, A. M., A. V. Newman, A. Ghosh, and G. T. Farmer (2007), Statistical modeling of the Middle America subduction zone using interplate seismicity, *Seismo. Res. Lett.*, Ann. Meet. Suppl., Abstract.

Tiampo, K. F., J. B. Rundle, J. Fernandez, and J. O. Langbein (2000), Spherical and ellipsoidal volcanic sources at Long Valley caldera, California, using a generic algorithm inversion technique, *J. Volcanol. Geotherm. Res., 102,* 189-206.

Tizzani, P., P. Berardino, F. Casu, P. Euillades, M. Manzo, G. P. Ricciardi, G. Zeni, and R. Lanari (2007), Surface deformation of Long Valley caldera and Mono Basin, California, investigated with the SBAS-InSAR approach, *Remote Sens. Environ., 108*, 277-289.

Torge, W. (2001), *Geodesy*, 3rd ed., 416 pp., Walter de Gruyter, Berlin, Germany.

Turcotte, D. L., and G. Schubert (2002), *Geodynamics,* 2nd ed., Cambridge Univ. Press, New York, NY, USA.

Turner, H. L., P. LaFemina, A. Saballos, G. S. Mattioli, P. E. Jansma, and T. Dixon (2007), Kinematics of the Nicaraguan forearc from GPS geodesy, *Geophys. Res. Lett., 34*, L02302, doi:10.1029/2006GL027586.

van Hinsbergen, D. J. J., D. G. van der Meer, W. J. Zachariasse, and J. E. Meulenkamp (2006), Deformation of western Greece during Neogene clockwise rotation and

collision with Apulia, *Int. J. Earth Sci.*, *95*(3), 463-490, doi:10.1007/s00531-005-0047-5.

van Hinsbergen, D. J. J., W. J. Zachariasse, M. J. R. Wortel, and J. E. Meulenkamp (2005), Underthrusting and exhumation: A comparison between the External Hellenides and the "hot" Cycladic and "cold" South Aegean core complexes (Greece), *Tectonics*, *24*, TC2011, doi:10.1029/2004TC001692.

von Huene, R., C. R. Ranero, W. Weinrebe, and K. Hinz (2000), Quaternary convergent margin tectonics of Costa Rica, segmentation of the Cocos Plate, and Central American volcanism, *Tectonics, 19*(2), 314-334, doi:10.1029/1999TC001143.

Waldhauser, F., and D. P. Schaff (2008), Large-scale relocation of two decades of Northern California seismicity using cross-correlation and double-difference methods, *J. Geophys. Res.*, *113*, B08311, doi:10.1029/2007JB005479.

Walter, J. I., S. Y. Schwartz, J. M. Protti, and V. Gonz á lez (2011), Persistent tremor within the northern Costa Rica seismogenic zone, *Geophys. Res. Lett.*, *38*, L01307, doi:10.1029/2010GL045586.

Wang, R., F. Lorenzo-Mart ń, and F. Roth (2003), Computation of deformation induced by earthquakes in a multi-layered elastic crust—FORTRAN programs EDGRN/EDCMP, *Comp. Geosci.*, *29*(2), 195-207, doi:10.1016/S0098-3004(02)00111-5.

Wech, A. G., and K. C. Creager (2007), Cascadia tremor polarization evidence for plate interface slip, *Geophys. Res. Lett.*, *34*, L22306, doi:10.1029/2007GL031167.

Wdowinski, S., Y. Bock, J. Zhang, P. Fang, and J. Genrich (1997), Southern California Permanent GPS Geodetic Array: Spatial filtering of daily positions for estimating coseismic and postseismic displacements induced by the 1992 Landers earthquakes, *J. Geophys. Res.*, *102*(B8), 18,057-18,070.

Webb, F. H., M. Bursik, T. Dixon, F. Farina, G. Marshall, and R. S. Stein (1995), Inflation of Long Valley Caldera from one year of continuous GPS observations, *Geophys. Res. Lett.*, *22*(3), 195-198.

Weiland, C. M., L. K. Steck, P. B. Dawson, and V. A. Korneev (1995), Nonlinear teleseismic tomography at Long Valley caldera, using three-dimensional minimum travel time ray tracing, *J. Geophys. Res.*, *100*(B10), 20,379-20,390.

Weinberg, R. F. (1992), Neotectonic development of western Nicaragua, *Tectonics*, *11*(5), 1010-1017, doi:10.1029/92TC00859.

Weinstein, S. A., and E. A. Okal (2005), The mantle wave magnitude M_m and the slowness parameter Θ: five years of real-time use in the context of tsunami warning, *Bull. Seismol. Soc. Am.*, *95*(3), 779-799, doi:10.1785/0120040112.

Wessel, P. and W. H. F. Smith (1991), Free software helps map and display data, *Eos Trans. AGU, 72*, 441.

White, R. A., and D. H. Harlow (1993), Destructive upper-crustal earthquakes of Central America since 1900, *Bull. Seismol. Soc. Am.*, *83*(4), 1115-1142.

Williams, S. D. P. (2003), The effect of coloured noise on the uncertainties of rates estimated from geodetic time series, *J. Geod.*, *76*, 483-494.

Williams, T., and C. Kelley, et al. (2007), Gnuplot – an interactive plotting program (Gnuplot manual version 4.2).

Yang, X., P. M. Davis, and J. H. Dieterich (1988), Deformation from inflation of a dipping finite prolate spheroid in an elastic half-space as a model for volcanic stressing, *J. Geophys. Res.*, *93*(B5), 4,249-4,257.

Zhang, J., Y. Bock, H. Johnson, P. Fang, S. Williams, J. Genrich, S. Wdowinski, and J. Behr (1997), Southern California permanent GPS geodetic array: Error analysis of daily position estimates and site velocities, *J. Geophys. Res.*, *102*(B8), 18,035-18,055.

Zumberge, J., M. Heflin, D. Jefferson, M. Watkins, and F. Webb (1997), Precise point positioning for the efficient and robust analysis of GPS data from large networks, *J. Geophys. Res.*, *102*(B3), 5005-5017, doi:10.1029/96JB03860.